Experimental Investigations on Stochastic Space-Time Channel Characteristics at 60 GHz Using an Antenna Array

vorgelegt von
Diplom-Ingenieur
Moon-Soon Choi
aus Kangnung, Korea

Von der Fakultät IV – Elektrotechnik und Informatik
der Technischen Universität Berlin
zur Erlangung des akademischen Grades

Doktor der Ingenieurwissenschaften
– Dr.-Ing. –

genehmigte Dissertation

Promotionsausschuss:

Vorsitzender:	Prof. Dr. h.c. Radu Popescu-Zeletin
Berichter:	Prof. Dr.-Ing. Dr. rer. nat. Holger Boche
Berichter:	Prof. Dr.-Ing. habil. Gerhard Mönich

Tag der wissenschaftlichen Aussprache: 21. November 2007

Berlin 2007

D 83

To the memory of my father.

Abstract

To cover steadily growing bandwidth requirements, future wireless communication systems could utilize spatial information of the propagation channels. For this, accurate knowledge of the space-time propagation channel structure is essential. Furthermore, the bandwidth shortage at lower frequencies is a primary limitation to development of broadband wireless systems. Therefore, mm-wave frequencies, especially in the 60 GHz frequency band, are interesting due to large available bandwidth (about 5 GHz), small antenna size (wavelength 5 mm) - favorable to compact devices - and small frequency reuse distance. Insights into the space-time propagation channel structure for the envisaged frequency band can be gained through experimental investigations.

This dissertation deals with the indoor measurement and statistical analysis of time-invariant wideband space-time propagation channel impulse responses (CIR) in the frequency range at 60 GHz using an antenna array.

The first part of this dissertation focuses on the channel reconstruction problem when wideband measurement is to be performed with a narrowband system that provides no perfect synchronization of oscillators. For propagation channel measurement, the synchronization of oscillators is usually carried out by applying a high precision reference source. If such a reference source is not available and the components to be used are limited to narrowband measurement, wideband measurement can be achieved by consecutive measurement of sub-channels and concatenation. However, the sub-channels suffer from individual random phase offsets, so that the concatenated channels would not represent the correct CIRs. The methods for proper reconstruction of sub-channels with respect to phase offsets are considered. More specifically, two compensation methods are investigated: the extrapolation and the overlap method. The methods are analyzed in terms of their feasibility. Moreover, improvement aspects specific to the intended measurement system are proposed. The compensation errors are expressed by means of simple mathematical analysis and performance of the methods is examined by simulative error analysis.

The second part is concerned with experimental investigations and statistical analysis. The overall measurement system setup is extended to the spatial domain using a 60 GHz patch antenna array. The measurement campaign is conducted in the corridors of an office building with a measurement RF-bandwidth of about 1 GHz. Parameters such as path gain, propagation delay and azimuth angle are extracted from the data provided by the measurement campaign using SAGE algorithm. Then, statistical analysis of the parameters is performed and their characteristics are discussed. As results, statistical characteristics of channel parameters such as delay spread, coherence bandwidth, K-factor and azimuth spread as well as empirical stochastic channel models like power spectra (PAS and PDS) and probability density functions for relative

delays and azimuth angles are shown.

Zusammenfassung

Um stetig steigende Bandbreitenanforderungen zu genügen, können künftige Mobilkommunikationssysteme die räumliche Informationen des Funkkanals ausnutzen. Hierzu sind genaue Kenntnisse über die Raum-Zeit Struktur des Funkkanals erforderlich. Zudem ist die Bandbreitenknappheit in niedrigen Frequenzbereichen eine grundlegende Beschränkung bei der Neuentwicklung von Breitbandmobilfunksystemen. Funkwellen im mm-Bereich insbesondere im 60 GHz Frequenzbereich werden dadurch interessant u.a. aufgrund der Größe der zur Verfügung stehenden Bandbreite (ca. 5 GHz), der kleinen Antennenabmessungen (günstig für Kompaktgeräte) und des kleinen Wiederverwendungsabstands von Frequenzen. Einblicke in die Struktur des Raum-Zeit-Funkkanals für das anvisierte Frequenzband können durch experimentelle Untersuchungen gewonnen werden.

Die vorliegende Dissertation behandelt die Indoor-Funkkanal-Messung und statistische Analyse der Impulsantworten (CIR) des zeitinvarianten breitbandigen Raum-Zeit-Funkkanals im 60 GHz Frequenzbereich unter Verwendung eines Antennenarrays.

Der erste Teil dieser Dissertation beschäftigt sich mit dem Problem der Kanalrekonstruktion, wenn breitbandige Funkkanalmessungen mit einem Schmalbandsystem ohne perfekte Synchronisation der Oszillatoren durchgeführt werden. Die Synchronisation der Oszillatoren wird bei der Funkkanalmessung üblicherweise unter Verwendung einer hochpräzisen Referenzquelle ausgeführt. Wenn eine solche Referenzquelle nicht zur Verfügung steht und die benutzten Komponenten nur für Schmalbandmessungen geeignet sind, kann eine breitbandige Funkkanalmessung durch das Zusammensetzen von stückweise gemessenen Unterkanälen erreicht werden. Die Unterkanäle sind jedoch individuell durch zufällige Phasenoffsets gestört, so dass die zusammengesetzten Funkkanäle nicht die korrekten CIRs darstellen. Es werden Methoden zur korrekten Rekonstruktion der Unterkanäle im Hinblick auf Phasenoffsets betrachtet. Dazu werden zwei Kompensationsmethoden untersucht: Die Extrapolations- und die Überlappungsmethode. Diese Methoden werden bzgl. der Durchführbarkeit analysiert. Ferner werden Verbesserungsaspekte speziell für das vorgesehene Messsystem vorgeschlagen. Die Kompensationsfehler werden durch einfache mathematische Analyse angegeben und die Leistungsfähigkeit der betrachten Methoden wird anhand von Simulationen überprüft.

Der zweite Teil befasst sich mit experimentellen Untersuchungen und statistischer Analyse. Das gesamte Messsystem wird durch Verwendung eines 60 GHz Patch Antennenarrays zur Azimuthwinkeldomäne erweitert. Die Messkampagnen werden in den Korridoren eines Bürogebäudes mit einer RF-Messbandbreite von ca. 1 GHz durchgeführt. Wichtige Parameter wie Pfadgewinn, Verzögerungszeit und Azimuthwinkel sind aus den Messdaten mittels des

SAGE-Algorithmus extrahiert. Eine statistische Analyse der Parameter wird ausgeführt und die Charakteristika werden diskutiert. Als Ergebnisse werden sowohl die Kanalparameter wie z.B. Zeitdispersion (delay spread), Kohärenzbandbreite, K-Faktor und Winkeldispersion (azimuth spread), als auch die empirischen stochastischen Kanalmodelle, z.B. die Leistungsspektren (PAS und PDS) bzw. die Wahrscheinlichkeitsdichtefunktionen für relative Verzögerungszeit und Azimuthwinkel dargestellt.

Acknowledgements

First of all, I thank my advisor Professor Holger Boche for his support throughout the last years. I also would like to express my thankfulness to Professor Gerhard Mönich for serving as second referee and reader of this dissertation. I am deeply grateful to Dr. Andreas Kortke for making available hardware components and giving advice on the setup sacrificing his valuable time. Furthermore, I want to thank Dr. Wilhelm Keusgen for reading of my work. My gratitude also goes to my former project leader Dr. Gerd Grosskopf, to colleagues Randolph Eggemann, Detlef Rohde for their support during our collaboration and to all other colleagues at the Heinrich Hertz Institute, Berlin. Finally, I would like to thank Katharina Schweers for her strong organisational help and Robert Schlabbach for his careful proofreading.

Contents

1 Introduction **2**

1.1 Problem Statement . . . 3

1.2 Related Work and Literature Survey . . . 4

1.3 Outline of the Dissertation . . . 6

2 Theoretical Background **8**

2.1 Radio Propagation Channel . . . 8

2.1.1 Channel Model . . . 8

2.1.2 Channel Parameters . . . 9

2.2 Measurement Techniques . . . 11

2.2.1 Narrowband Technique . . . 12

2.2.2 Pulse Technique . . . 12

2.2.3 Frequency Sweep Technique . . . 12

2.2.4 Correlation Technique . . . 13

2.2.5 Spatial Measurement Techniques . . . 13

2.3 Space-Time Channel Models for Smart Antennas . . . 14

2.3.1 Lee's Model . . . 14

2.3.2 Stapleton's Model . . . 15

2.3.3 Geometrically Based Single Bounce Statistical Channel Models . . . 15

2.3.4 The GWSSUS Model . . . 16

2.3.5 Time-Varying Vector Channel Model . . . 18

2.3.6 Two GSM Simulation Models . . . 19

2.3.7 The Uniform Sectored Distribution Model . . . 19

2.3.8 Modified Saleh-Valenzuela's Model . . . 19

2.3.9 Extended Tap-Delay-Line Method . . . 20

2.3.10 Other Models . . . 20

2.4 Multi-Dimension Parameter Estimation Techniques . . . 21

2.4.1 SAGE Algorithm . . . 21

2.4.2 Unitary Multi-dimensional ESPRIT . . . 25

2.4.3 Other Techniques . . . 28

3 Simulative Analysis **30**

3.1 Problem Statement . . . 31

3.2 Concatenation Methods . . . 32
3.2.1 Overlap Method . . . 32
3.2.2 Extrapolation Method . . . 35
3.3 Simulative Examination . . . 37
3.3.1 Preliminary Consideration . . . 37
3.3.2 Simulative Error Analysis . . . 40
3.4 Summary and Discussion . . . 57

4 Measurement System Setup 58
4.1 Measurement System Setup . . . 58
4.1.1 Description of the modules . . . 58
4.1.2 Channel Sounder Setup . . . 60
4.1.3 System Calibration . . . 62
4.2 Examination of the Measurement System . . . 64
4.3 Summary and Discussion . . . 65

5 Statistical Characteristics of Indoor Radio Channel at 60 GHz 69
5.1 Site Description and Measurement Campaign . . . 69
5.2 General Observation . . . 70
5.3 Statistics of Channel Parameters . . . 73
5.3.1 Time of Arrival Statistics . . . 73
5.3.2 Angle of Arrival Statistics . . . 76
5.4 Statistical Space-Time Channel Models . . . 77
5.4.1 Power Azimuth-Delay Spectrum . . . 77
5.4.2 Power Delay Spectrum . . . 78
5.4.3 Power Azimuth Spectrum . . . 79
5.4.4 Probability Density Function of TOA . . . 80
5.4.5 Probability Density Function of AOA . . . 81
5.5 Summary and Conclusion . . . 83

6 Conclusions and Future Work 84
6.1 Summary of the Main Results . . . 84
6.2 Future Work . . . 86

A Acronyms 94

B Error Statistics to Sec. 3.3.2. E, "Enh.#1". 96

C Error Statistics to Sec. 3.3.2. F. 98

D Figure to Sec. 3.3.2. G. 99

E Site Photos. 100

F Measured and Reconstructed PAPs. 102

Chapter 1

Introduction

In recent years, the market share of wireless communication technology has been growing remarkably. Its lower demand for infrastructure and easy usability of location-independent access to desired contents of information significantly contribute to its success. Thus, modern wireless communication systems such as wireless local area network (WLAN), universal mobile telecommunications system (UMTS), global system for mobile communication (GSM), digital video broadcasting-terrestrial/satellite (DVB-T/S) and digital multimedia broadcasting (DMB) are indispensably established in today's information society. Current efforts of the industry are focused on two terms concerning future products: *convergence* between different systems and *ubiquitous access*. In this context, wireless technology will occupy a central position. In order to accommodate users with integrated services such as voice, data, multimedia and broadcasting, future wireless communication systems require higher bandwidth, which in turn offers enormous potential for growth to the wireless industry.

From the system designer point of view, this trend requires higher system capacity as well as large transmission bandwidth. These can be significantly increased [1] through extension of classical systems to the spatial domain. This has been shown by many researchers (see [2] for an overview). The adaptive antenna array technique (which is also referred to as *Smart Antenna Technique*) and the multiple input multiple output (MIMO) technique are among such systems exploiting the space-time channel structure, which are promising candidates for future wireless systems.

The bandwidth shortage at lower frequencies is a primary limitation to development of broadband wireless systems. Therefore, mm-wave frequencies, especially the 60 GHz frequency band has gradually gained in importance. For short range indoor communication, the 60 GHz frequency band, where a high oxygen absorption occurs (15.5 dB/km), is particularly attractive because of its small frequency reuse distance and the large available unlicensed bandwidth (about 5 GHz) [3]. Furthermore, the small antenna size for 60 GHz (wavelength 5 mm) allows the design of compact devices. For these reasons, a 60 GHz WLAN would be a very interesting option in addition to WLAN based on 802.11a/b/g standards discussed in [4].

Design of a new wireless system typically requires a comprehensive system analysis. For this, both investigation of information-theoretical aspects and system level simulations are required in order to assess feasibility and system performance. Such assessment is usually conducted

based on a relevant propagation channel model for the intended environment. Hence, accurate knowledge of the propagation channel plays a considerable role for the successful establishment of the system.

1.1 Problem Statement

This dissertation deals with the indoor measurement and statistical analysis of time-invariant wideband space-time channel impulse responses in the frequency range at 60 GHz using an antenna array. For the optimization of future 60 GHz system designs, the knowledge of the space-time channels is essential. The multipath structure with respect to the spatial and temporal domain can be characterized by experimental investigations. A well featured design of a 60 GHz measurement system is challenging above all due to high time resolution requirements and the cost of components. The extension of a measurement system to the spatial domain is thus impeded due to the need for multiple system components.

In the first part of the dissertation, we focus on wideband measurement problem with special emphasis on channel reconstruction, when measurement is to be performed with a narrowband system. A wideband channel measurement can be usually achieved when the desired RF-bandwidth is swept in the frequency domain using a narrowband system such as vector network analyzer (VNA). Extension to the spatial domain at 60 GHz using a VNA is not easy. Moreover, channel sounder setup also depends on available components. For the measurement of complex-valued channel impulse response (CIR), one should take great care of the synchronization of oscillators used in the transmitter and receiver. The synchronization is usually carried out by applying a high precision reference source such as a *rubidium atom normal*. If such a reference source is not available and the components to be used are limited to narrowband measurement, wideband measurement can be achieved by partial measurement of sub-channels and concatenation. However, the sub-channels suffer from individual random phase offsets, so that the concatenated channels would not represent the correct CIRs. The goal of investigation in this part is to provide a solution for the proper reconstruction of sub-channels, so that the concatenated wideband CIRs are represented correctly. More precisely, the compensation methods of phase offsets are considered. The considered methods are analyzed in terms of their reliability. For this, the compensation errors are expressed by means of simple mathematical analysis. Improvement features specific to the intended measurement system are proposed. Then, the feasibility of the methods is examined by simulative error analysis.

The second part is concerned with the experimental investigations. A suitable technique for high speed transmission at 60 GHz is supposed to be orthogonal frequency-division multiplex (OFDM) technique due to its easy scalability to different environments, bandwidths or bit rates [4]. The growth of complexity of an OFDM system in conjunction with bit rate increase is small compared to a single carrier system. Furthermore, the future 60 GHz systems may rely on the antenna diversity techniques such as adaptive antenna technique, MIMO technique and space-time coding due to the limited available power as well as the high attenuation. For the

effective employment of these techniques in future systems, accurate knowledge of the space-time channel structure is required. Though some previous work addressing indoor space-time channel characteristics for lower frequencies are given [5–8], relevant publications for 60 GHz environment are scarcely available.
In this part, the measurement system setup for the space-time channel measurement is carried out. Moreover, the statistical analysis of the data provided by the measurement campaign at 60 GHz conducted in the corridors of an office building is performed. Statistical characteristics of channel parameters with respect to the time of arrival (TOA) such as delay spread, coherence bandwidth, K-factor and relating to the angle of arrival (AOA) like azimuth spread are investigated. Furthermore, the empirical stochastic channel models like power spectra - power azimuth spectrum (PAS) and power delay spectrum (PDS) - and probability density functions (PDF) for relative delays and azimuth angles are investigated.

In summary, the main contributions of this thesis comprise:

- The formulation of wideband measurement problem when using a narrowband system
- The proposals of the improvement features for the channel reconstruction methods specific to the intended measurement system
- The feasibility evaluation of the methods by means of simulative error analysis
- The setup of the 60 GHz space-time channel measurement system and the examination of the measurement system by experimental investigations
- The results from statistical analysis of the measured data with respect to the spatial and temporal channel parameter domains

1.2 Related Work and Literature Survey

The history of modern wireless communications began in the 19 th century. *James Clerk Maxwell* elaborated the research works, amongst others, of *Michael Faraday* and *André Marie Ampère* about electricity and magnetism and presented the *Maxwell's* wave equations for the first time in 1864 in the *Royal Society*. His theory was later approved by *Heinrich Rudolf Hertz* through his experiment with the *Hertz's Oscillator* showing the existence of the electromagnetic waves. These results delivered the fundament for the development of today's wireless communication technologies.

For wave propagation in indoor environments, the solution of *Maxwell's* differential equations was found to be highly complex, so that it can be determined only by strong simplifications. For the radio channel in communication systems, the channel was considered as a linear system [9], so that it can be characterized by the channel impulse response (CIR), $h(t, \tau)$, which describes the relationship between the input and the output of a linear system. The parameters associated with

$h(t, \tau)$ are connected with random probability resulting in a stochastic channel model. Based on this point of view, numerous approaches to find the statistical characteristics of $h(t, \tau)$ have been undertaken by means of simulations or experimental investigations. The ray-tracing technique for example is a simulation method for determining the CIR as well as predicting the wave propagation in buildings [10–13]. Radio propagation channel measurements have been conducted for many years at different carrier frequencies and in different environments. The results showed that the measured CIRs often exhibit properties, which are specific to the measured environments and frequencies reflected in diverse values of channel parameters [14, 15]. At 60 GHz, a lot of measurement efforts have been dedicated. Most of them investigated only the temporal domain and investigation of the space-time channel is scarcely available.

If channels are wide sense stationary (WSS) and uncorrelated scattering (US), the delay spread and the coherence time can be defined, which are important for the determination of the frequency selectivity of the channel. For office buildings, corridors and rooms at 60 GHz, root mean square (RMS) delay spreads smaller than 20 ns were reported in [16–20]. But large RMS delay spread values were also reported in [21] and [22]. In [22], delay spread values up to 76 ns for long hallways and up to 41 ns for large rooms were measured, when the transmitter and receiver were not aligned. By fixing the receiver antenna, the values were reduced significantly to values smaller than 47.3 ns for hallways and smaller than 33.9 ns for rooms, respectively. The coherence bandwidth was reported in [23] as remaining below 38 MHz using a 10 dBi Tx horn antenna and an omnidirectional Rx antenna. When the Rx is shadowed by humans, a noticeable decrease of the coherence bandwidth was found. The relationship between the deterministic (dominant, LOS path) component and stochastic contributions (multipath components) is defined as the Ricean K-factor [24]. Some results were reported in [25]. Investigations on effects of antenna diversity and polarization can be found in [16] and [26]. It was shown that multipath components due to wall reflections can be effectively suppressed by employing circular polarization instead of linear polarization.

The space-time channel measurement can be performed using an uniform linear array (ULA) of M elements with an element spacing of $\lambda/2$, which was used in [27]. However, this requires high realization cost due to the need of multiple hardware. A novel measurement technique was proposed in [28] and its principle relies on the multiplexing of M array antenna outputs using a single RF down-converter. Therefore, the hardware expense is much reduced. A similar measurement concept was proposed by [29] using only a single $\lambda/4$ monopole antenna by moving the antenna along the sensor locations forming a virtual antenna array by means of a stepping motor for positioning. Other measurement techniques rely on using a mechanically steerable high gain antenna.

The stochastic channel model proposed by *Bello* in [9] was extended into the spatial domain [30]. Relying on the terminology, researchers investigated models for power spectra such as power delay spectrum (PDS) and power azimuth spectrum (PAS) as well as probability density function (PDF) of propagation delay and azimuth angle through the statistical analysis either based on measurements or analytical approach. Propagation channel measurements at

60 GHz including the angle of arrival (AOA) pattern can be found earlier in [31], [32] and more recently in [22]. Their measurement concepts were commonly based upon using a mechanically steerable Rx antenna with a small beamwidth rotated in the azimuthal direction. Unfortunately, information useful for modeling is missing in [31] and [32], while the angular dispersion was analyzed statistically in [22] showing increasing angular spreads from outdoor to indoor environment as well as from hallway to room. Statistical space-time channel models for lower frequencies were addressed in some publications. For instance, empirical models for outdoor environment were proposed in [5]. Models for indoor environments were addressed in [6–8]. In all reports, the PDS and the PAS were recommended to be used by an exponential decaying function and a Laplacian distribution function, respectively, for both indoor and outdoor. Also, an exponential PDF was proposed to the model for relative propagation delay for indoor and outdoor environment, while different models for the PDF to the azimuth angle were suggested. For models to the azimuth angle, a Laplacian PDF was reported by [6] and [7] from indoor measurements, while a Gaussian PDF was proposed by [5] from outdoor measurements.

1.3 Outline of the Dissertation

- In chapter 2, relevant terms relating to the radio propagation channel and the associated channel parameters are discussed. Furthermore, channel measurement techniques with respect to the temporal and spatial domain, known channel models for smart antenna systems and multi-dimensional parameter estimation techniques are reviewed.

- In chapter 3, wideband channel measurement problem is addressed when using a narrowband system, if the measurement system lacks the required synchronization. Thereby, the measured sub-channels individually suffer from the phase offsets. These have to be compensated to represent the channel impulse response (CIR) correctly when a wideband channel measurement is achieved by concatenation of the consecutively measured sub-channels. Specifically, the concatenation methods are considered as a post signal processing for the channel reconstruction. Improvement aspects to the methods are proposed, which rely on the exploitation of redundant information of the antenna array channels as well as the optimal choice of the reference sub-channel for compensation. The compensation error of the methods is analyzed and the feasibility of the methods is examined by simulative error analysis.

- In chapter 4, the measurement system setup is described. The measurement system is designed to investigate the space-time radio channel at 60 GHz. The system is a narrowband system and is comprised mainly of a 60 GHz patch antenna array and a digital array transceiver that allows parallel baseband conversion of the antenna array signals. The desired measurement bandwidth of about 1 GHz in the frequency domain is achieved by applying the previously considered concatenation method to the consecutively measured sub-channel measurements. This chapter also depicts the system components used

and system calibration. Overall measurement setup is specified and the reliability of the measurement system is evaluated.

- The results from the statistical analysis of the data obtained by measurements at 60 GHz in the corridors of an office building are presented in chapter 5. The channel parameters are extracted with respect to time of arrival (TOA) and angle of arrival (AOA). Moreover, the empirical stochastic space-time channel models are presented, which include the power delay spectrum (PDS), power azimuth spectrum (PAS) and probability density function (PDF) for relative delays and azimuth angles, respectively.

- Chapter 6 draws conclusions and summarizes the main contributions of the dissertation. Finally, some possible research directions through future work are pointed out.

Chapter 2

Theoretical Background

2.1 Radio Propagation Channel

2.1.1 Channel Model

In mobile radio propagation environments, a large number of waves travelling through different paths arrives at the receiver antenna, which are supposed to be sufficiently attenuated after a certain number of propagation mechanisms such as scattering, diffractions, reflections and transmissions through objects (see Fig. 2.1). This phenomenon is referred to as *multipath propagation* and is generally time-varying. For such a scenario, the channels can be represented by their impulse responses $h(t, \tau)$ and can be well described by complex channel gains and propagation delays given in [9] and [14].

$$h(t, \tau) = \sum_{l=0}^{L(t)-1} \alpha_l(t)\delta(t - \tau_l(t)), \tag{2.1}$$

where α_l, τ_l and $\delta(.)$ denote the complex channel gain, the propagation delay of l th multipath component and the dirac impulse, respectively. The $L(t)$ is the varying number of multipath components as the mobile station (MS) moves. For indoor propagation environments, movement of humans typically contributes to the time-varying factors, so it is adequate to consider the channel as quasi-stationary [33]. For the stationary (time-invariant) channel, the expression in (2.1) can be reduced to

$$h(\tau) = \sum_{l=0}^{L-1} \alpha_l \delta(\tau - \tau_l) \tag{2.2}$$

Suppose that the receiver has an uniform linear array (ULA) consisting of M antenna elements located at $r_1, ..., r_M \in \mathbb{R}^2$ with respect to an arbitrary reference point. Furthermore, it is assumed that a finite number L of specular plane waves from the directions $\phi_0, ..., \phi_{L-1}$ are impinging at the base station (BS). The channel model (2.2) can be extended into the spatial domain by superposition of multipath components from L different directions as

$$h(\tau, \phi) = \sum_{l=0}^{L-1} \alpha_l \delta(\tau - \tau_l)\delta(\phi - \phi_l), \tag{2.3}$$

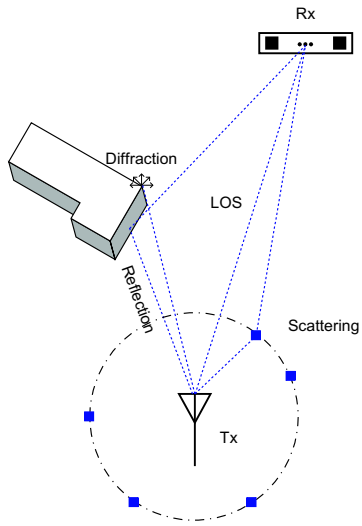

Figure 2.1: Multipath Propagation in mobile radio communication.

where ϕ_l is the azimuthal angle of arrival (AOA) of the wave from the l th path. An equivalent expression to (2.3) in the frequency domain results by fourier transformation of (2.3) to

$$H_m[n] = \sum_{l=0}^{L-1} \alpha_l \exp\{-j2\pi f_n \tau_l\} \exp\{-j2\pi(m-1)\frac{d}{\lambda} sin(\phi_l)\}, 1 \leq n \leq N, \tag{2.4}$$

where H_m denotes the channel frequency response (CFR) of m th antenna element, d is the spacing between the antenna elements, λ is the wavelength, f_n is the n th frequency bin of the frequency response and N is the total number of frequency samples. The CFR functions across the M antenna elements $\mathbf{H}[n] = [\mathbf{H}_1[n], ..., \mathbf{H}_M[n]]^T$ for $m = 1, ..., M$ can be written in Matrix notation as

$$\mathbf{H}[n] = \sum_{l=0}^{L-1} \mathbf{a}(\phi_l)\alpha_l \exp\{-j2\pi f_n \tau_l\} \in \mathbb{C}^{M \times N}, \tag{2.5}$$

where $\mathbf{a}(\phi_l) = [1, e^{-j2\pi \frac{d}{\lambda} sin(\phi_l)}, ..., e^{-j2\pi(M-1)\frac{d}{\lambda} sin(\phi_l)}]^T \in \mathbb{C}^{M \times 1}$ is the steering or array response vector. According to (2.5), the space-time channel can be characterized by the parameter set $\{\alpha_l, \phi_l, \tau_l\}$.

2.1.2 Channel Parameters

Since the propagation channel is regarded as a complex random process, the system correlation functions of $h(t, \tau)$ and $H(t, f)$ are defined as

$$R_h(t, t'; \tau, \tau') = E[h^*(t, \tau)h(t', \tau')] \tag{2.6}$$

$$R_H(t, t'; f, f') = E[H^*(t, f)H(t', f')], \tag{2.7}$$

where $E[.]$ and $(.)^*$ denote the expectation and the complex conjugation operator, respectively. A stochastic process is referred to as *wide sense stationary* (WSS), if its mean value is time-independent and its correlation function depends only on the time difference. Furthermore, an *uncorrelated scattering* (US) process means that signals impinging from different paths are uncorrelated.

The correlation function (2.6) yields for the *wide sense stationary uncorrelated scattering* (WSSUS) channel to

$$R_h(t, t+\Delta t; \tau, \tau') = R_h(\Delta t; \tau, \tau') \tag{2.8}$$

$$R_H(t, t+\Delta t; f, f') = R_H(\Delta t; f, f'), \tag{2.9}$$

If the channel is WSS with respect to t and US with respect to τ, the correlation function can be written as

$$R_h(t, t+\Delta t; \tau, \tau') = P_h(\Delta t, \tau)\delta(\tau' - \tau), \tag{2.10}$$

where $P_h(\Delta t, \tau) = E[h(t,\tau)^* h(t+\Delta t, \tau)]$. For $\Delta t = 0$, we obtain the delay power spectrum expressed as

$$P_h(0, \tau) = E[|h(t,\tau)|^2], \tag{2.11}$$

which represents the average power of a time-variant channel as a function of τ. The expression in (2.11) can be used for a measure of the time dispersion of the channel, which is called RMS delay spread.

The Power Delay Profile: The power delay profile is defined as

$$P(\tau) \triangleq \sum_l |\alpha_l|^2 \delta(\tau - \tau_l) \tag{2.12}$$

The RMS delay spread (σ_τ): The RMS delay spread is the square root of the second central moment of the power delay profile $|h(t)|^2$ given by

$$\overline{\tau^2} = \frac{\sum_l |\alpha_l|^2 \tau_l{}^2}{\sum_l |\alpha_l|^2} \tag{2.13}$$

$$\sigma_\tau \triangleq \sqrt{\overline{\tau^2} - (\bar{\tau})^2}, \tag{2.14}$$

where $\bar{\tau}$ is the mean excess delay defined as:

The mean excess delay ($\bar{\tau}$): This is the first central moment of (2.12) and is defined by

$$\bar{\tau} \triangleq \frac{\sum_l |\alpha_l|^2 \tau_l}{\sum_l |\alpha_l|^2}. \tag{2.15}$$

Under the WSSUS assumption, the correlation function in frequency domain using (2.9) yields

to

$$R_H(t, t+\Delta t; f, f+\Delta f) = R_H(\Delta t; \Delta f), \tag{2.16}$$

which is referred to as the *space-frequency correlation function*, since it depends only on the time difference as well as the frequency difference and not on the particular frequencies. For $\Delta t = 0$, the function (2.16) yields $R_H(\Delta f) \equiv R_H(0, \Delta f)$ and is related to (2.11) as the fourier transform pair. $R_H(0, \Delta f)$ provides information about the channel's coherence in the frequency domain and its measure is defined as the *coherence bandwidth* (B_ρ) as

The coherence bandwidth (B_ρ): The frequency correlation function, $R_H(\Delta f)$, is given by

$$R_H(\Delta f) = \int_{-\infty}^{\infty} H(f)H^*(f+\Delta f)df, \tag{2.17}$$

where $H(f)$ is the complex CFR and Δf is frequency shift. $R_H(\Delta f)$ is a measure of the magnitude of the correlation between the channel responses at two spaced frequencies. The coherence bandwidth B_ρ is a statistical measure of the range of frequencies over which two frequency components have a strong potential for amplitude correlation [34]. In order to determine the B_ρ quantitatively, threshold values are introduced and the usually used values are $\rho = \{0.5,\ 0.9\}$. A channel is *frequency selective* when the B_ρ is small compared to the transmitted signal bandwidth.

The coherence bandwidth B_ρ is related to the RMS delay spread σ_τ as

$$B_\rho \approx \frac{1}{\beta\sigma_\tau}. \tag{2.18}$$

Another channel measure is the *Ricean K-factor* defined as

The Ricean K-factor (K_{dB}): The Ricean K-factor gives the relationship between the power of the LOS component (P_{LOS}) and the power of the reflected multipath components (σ_r).

$$K_{dB} = 10log_{10}\frac{P_{LOS}}{2\sigma_r} \tag{2.19}$$

As a measure for the angular dispersiveness, the *RMS angle spread* is defined similar to (2.14).

The RMS angle spread (σ_ϕ): The RMS angle spread is defined by

$$\sigma_\phi = \sqrt{\frac{\sum_{l=0}^{L-1}|\alpha_l|^2\phi_l^2}{\sum_{l=0}^{L-1}|\alpha_l|^2} - \left(\frac{\sum_{l=0}^{L-1}|\alpha_l|^2\phi_l}{\sum_{l=0}^{L-1}|\alpha_l|^2}\right)^2} \tag{2.20}$$

2.2 Measurement Techniques

A variety of channel sounding systems has been utilized by many researchers so far. The sounding systems used differ depending on the emphasis of the research and available hardware compo-

nents.

2.2.1 Narrowband Technique

In this technique, an unmodulated continuous carrier signal is transmitted and the receiver is usually movable. The advantages of this technique are its simplicity and speed. Thus, this technique is well suited for investigation of path loss measurement, narrowband fading and Doppler effects. The shortcoming of this technique is that multipath information is unavailable, because only the envelope of multipath components can be obtained.

2.2.2 Pulse Technique

If the propagation channel is excited by an ideal δ-impulse as the input signal, its impulse response can be directly obtained at the output of the measurement system. In practice, the input signal of a channel sounder is a series of impulses with a defined pulse duration T_c that are modulated with sinusoidal carrier signals. For the wideband propagation channel measurements, the transmitter has to emit pulses which should possess sufficient power within a short pulse duration, whereby the cost and the complexity are increased. The pulse duration T_c must be less than the minimum relative delay between any two multipath components to distinguish between them. The advantage of the pulse method is its simple realization in conjunction with fast operation, so that it is well applicable for determining the power delay profile. The disadvantage of this method is the need of a wideband receiver due to the short pulse duration. The dynamic range is usually limited to 30 - 40 dB by the nonlinearity of the components (for example the amplifier).

2.2.3 Frequency Sweep Technique

In this method, the RF-bandwidth B_{RF} is swept with a single sinusoidal transmit signal by increasing the carrier frequency successively in Δf steps. The measured frequency response $Y(f)$ is compared with the local saved frequency response $X(f)$

$$H(f) = \frac{Y(f)}{X(f)}. \tag{2.21}$$

The technique is used in VNA. Due to the dual relationship between the time and frequency representation, the CIR can be completely described by the CFR. Though this method is equivalent to time domain measurement using a periodic pulse train, the frequency sweep method provides several advantages. Because this method uses a single tone signal at a time, a narrowband filter can be used to reject interference and noise. This increases the dynamic range. The time resolution is only limited by the range of the frequency sweep bandwidth. Furthermore, the amplitude and phase of channels are measured, while most time domain detectors do not provide information about the phase. The drawback of this method is that the channel has to be absolutely stationary during the measurements. The need of the phase reference at the

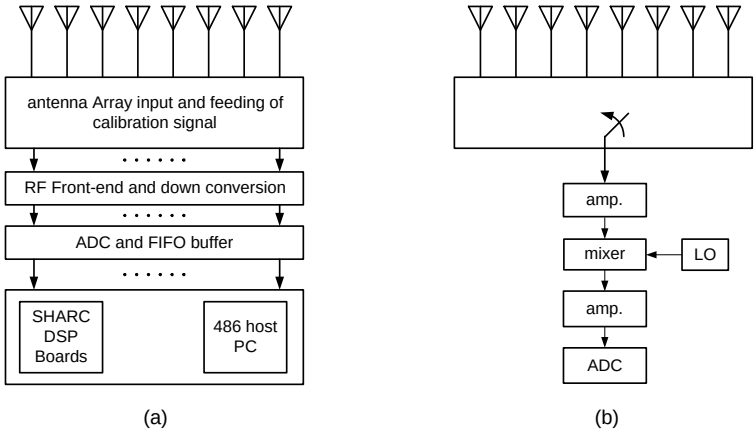

Figure 2.2: Spatial measurement using an antenna array: (a) real time parallel measurement [27], (b) measurement by multiplexing of array outputs [28].

receiver site is another downside. The reference phase is usually supplied by a cable, which limits mobility.

2.2.4 Correlation Technique

In the correlation method, modulated periodic pseudo random binary signals are transmitted over a channel. At the receiver, the same pseudo random binary signals are used to retrieve the transmitted signals, which are convolved with the channel. Thus, the complex CFR function can be estimated. The implementation of the correlator is different as the case arises: the hardware implementation of a sliding correlator [22] or A/D sampling with subsequently correlation with a microprocessor. The advantage of the method is the fast measurement speed, while the available maximum measurement bandwidth is limited by the bandwidth and speed of the components used.

2.2.5 Spatial Measurement Techniques

- **Real Adaptive Antenna Array:** Spatial channel information can be obtained by using an adaptive antenna system. Using an ULA, the incidence azimuth or elevation angle of waves can be resolved. To include both the azimuth and the elevation angles, an uniform rectangular array (URA) is usually employed. The realization of a real time channel sounder equipped with an adaptive antenna results in high cost and complexity. Furthermore, the antenna array must be accurately calibrated to avoid undesired effects such as inter-element coupling and gain mismatching. An example for such a real time adaptive antenna array system is depicted in Fig. 2.2 (a), which was used for outdoor measurements at carrier frequency 1.8 GHz [27].

- **Antenna Array with Multiplexing:** A measurement technique utilizing multiplexing at the outputs of the antenna array is shown in Fig. 2.2 (b). Therefore, the sounding system

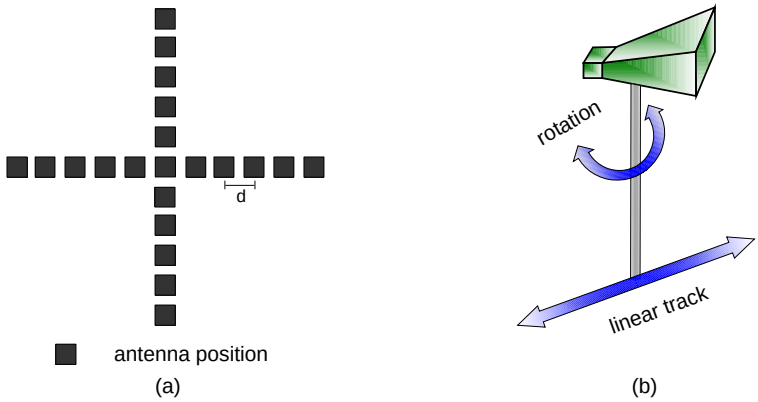

Figure 2.3: Other spatial measurement examples: (a) virtual cross array using a single $\lambda/4$ monopole antenna and positioning by a stepping motor [29], (b) measurement using a highly directional antenna rotated in the azimuthal directions [22].

is realized using only one RF-frontend as well as one based band conversion module. The depicted system was deployed for measurements at 5.2 GHz.

- **Virtual Antenna Array:** A single antenna can also be used for spatial measurement when a positioning system is available. This technique is referred to as *synthetic aperture array*, where a single antenna is moved to different antenna locations. A virtual cross array with total of 11 antenna positions in each dimension was utilized in [29] as illustrated in Fig. 2.3 (a). A single $\lambda/4$ monopole antenna moves step by step on a motor-driven platform along the coordinates of array element positions.

- **High Gain Directional Antenna:** A mechanically steered directional antenna can be used for AOA measurements. By rotating a high directional antenna in the azimuthal directions, the waves from different directions can be resolved. Fig. 2.3 (b) shows a such system used in [22].

2.3 Space-Time Channel Models for Smart Antennas

In this section, the known space-time channel models are reviewed and their key results are discussed.

2.3.1 Lee's Model

In this model, the following assumptions are made:

- N scatterers are uniformly distributed on the circle around the mobile with radius R. They are referred to as *effective scatterers* and each of them should represent the effect of many scatterers within the region (see. Fig. 2.4).

- A scatterer is located on the LOS.

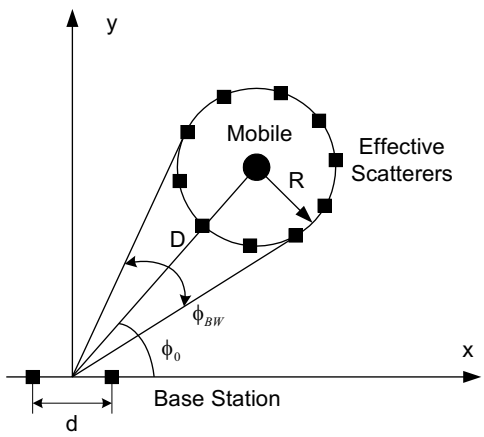

Figure 2.4: Lee's Model.

The discrete DOAs are given [35]

$$\phi_i \approx \frac{R}{D}\sin(\frac{2\pi}{N}i). \tag{2.22}$$

From (2.22), the correlation of the narrowband signals between any two elements of the array can be found using [35]

$$r(d, \phi_0, R, D) = \frac{1}{N}\sum_{i=0}^{N-1} e^{\{-j2\pi d\cos(\phi+\phi_i)\}} \tag{2.23}$$

where d is the element spacing and ϕ_0 is measured with respect to the line between the two elements as illustrated in Fig. 2.4. This model is used to indicate the performance of spatial diversity methods by determining the level of correlation [35, 36]. The model reveals that the necessary element spacing for good diversity is about 0.2λ for a mobile receiver and about 40λ for a tall base station.

2.3.2 Stapleton's Model

This model describes an extension to Lee's model proposed by *Stapleton et al.* in [37] by introducing an angular velocity on the ring of scatterers. Stapleton proposed a further extended model [38], in which supplementary scatterer rings are added to support different power delay profiles. This model is quite useful in predicting the correlation between any two elements of the array. However, it is not well suited for simulations requiring a complete model of vector channel impulse response of the wireless channel [1].

2.3.3 Geometrically Based Single Bounce Statistical Channel Models

A spatial scatterer density function is introduced to geometrically based single bounce statistical channel models (GBSBSCM). From the location of each of the randomly placed scatterers, the

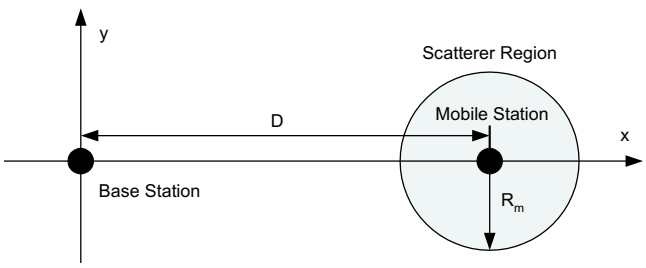

Figure 2.5: Circular scatterer density geometry.

DOA, TOA and signal amplitude are determined. Two variations of the GBSB are considered: the GBSB Circular Model and the GBSB Elliptical Model.

GBSB Circular Model

This model assumes that the scatterers are located at any position within the region of a circle with the radius R_m around the mobile (see. Fig. 2.5). This idea originated in the earlier publications [39] and [36]. Moreover, the scatterers near the base station are considered to be negligibly small(e.g. in macrocell environments). From this model, the joint TOA and DOA probability density functions (PDF) at the base station as well as at the mobile are derived. According to the obtained PDFs, this model appears to predict a relatively high probability of multipath components within a small range of angles. Measurement results suggest that typical angle spreads for macrocell environments with Tx-Rx separation of 1 km are approximately two to six degrees [1].

GBSB Elliptical Model

This model was developed for microcell and picocell environments where multipath components and the base station are located near the mobile station. Uniformly distributed scatterers are assumed to be within an ellipse, as shown in Fig. 2.6. Similar to GBSB Circular Model, the joint TOA and DOA PDFs are derived.

2.3.4 The gaussian wide sense stationary uncorrelated scattering (GWSSUS) Model

In the GWSSUS model, scatterers are grouped into clusters in space as depicted in Fig. 2.7. The location and delay associated with each cluster are assumed to remain constant over r data bursts. The received signal vector is

$$\mathbf{y}_r(t) = \sum_{k=0}^{C-1} \mathbf{a}_{k,r} s(t - \tau_k) \tag{2.24}$$

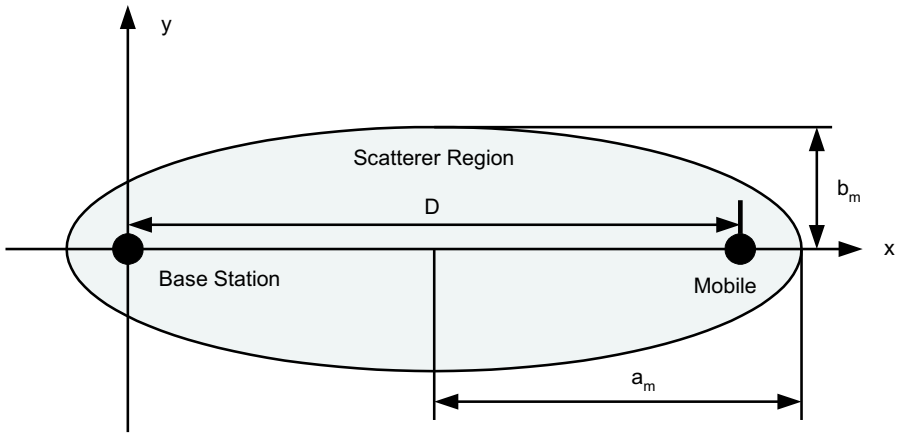

Figure 2.6: Elliptical scatterer density geometry.

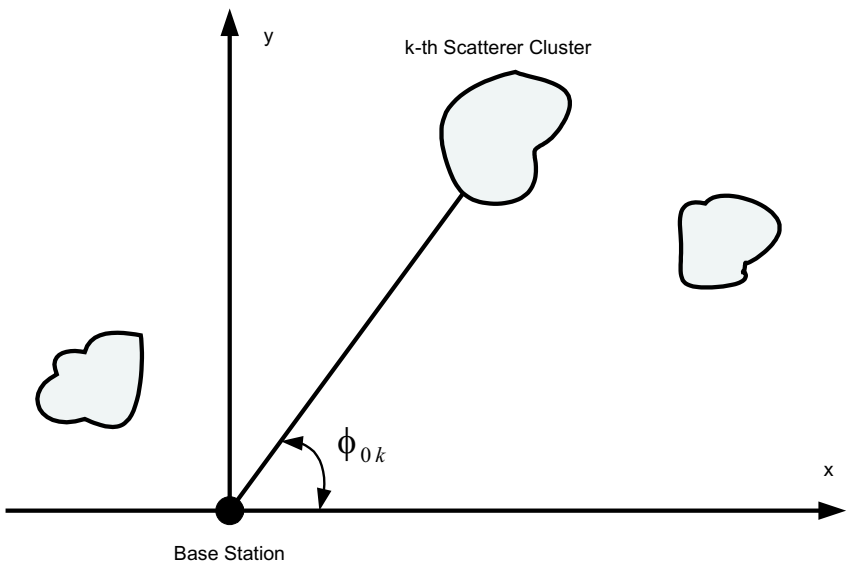

Figure 2.7: GWSSUS geometry with three clusters and the mean DOA ϕ_{0k}.

where $\mathbf{a}_{k,r}$ is the superposition of the steering vectors $\mathbf{a}(\phi)$ during the r th data burst within the k th cluster and may be expressed as

$$\mathbf{a}_{k,r} = \sum_{i=0}^{N_k-1} \beta_{k,i} e^{\{j\psi_{k,i}\}} \mathbf{a}(\phi_{0k} - \phi_{k,i}) \tag{2.25}$$

where C denotes the number of clusters, N_k is the number of scatterers in the k th cluster, $\beta_{k,i}$ is the amplitude, $\psi_{k,i}$ is the phase, ϕ_{0k} is the mean DOA for the k th cluster, $\phi_{k,i}$ is the DOA of the i th reflected scatterers of the k th cluster and $\mathbf{a}(\phi)$ is the steering vector in the direction of ϕ. It is assumed that the steering vectors are independent for different k. For sufficiently large N_k, the central limit theorem may be applied to the elements of $\mathbf{a}_{k,r}$. Under this condition, the elements of $\mathbf{a}_{k,r}$ are Gaussian distributed. It is assumed that the time delay τ_k is constant over several bursts and the vectors $\mathbf{a}_{k,r}$ are zero mean, complex Gaussian wide sense stationary random processes. When no line of sight component is present, the mean will be zero due to the random phase $\psi_{k,i}$, which is assumed to be uniformly distributed in $[0, 2\pi]$. When a line of sight component is present, the mean becomes a scaled version of the corresponding array response vector $E\{\mathbf{a}_{k,r}\} \propto \mathbf{a}(\phi_{0k})$. The covariance matrix for the k th cluster is given by

$$\mathbf{R}_k = E\{\mathbf{a}_{k,r}\mathbf{a}_{k,r}^H\} \tag{2.26}$$

$$= \sum_{i=0}^{N_k-1} \mid \beta_{k,i} \mid^2 E\{\mathbf{a}(\phi_{0k} - \phi_{k,i})\mathbf{a}^H(\phi_{0k} - \phi_{k,i})\} \tag{2.27}$$

This model provides a general result for the form of the covariance matrix. Since it does not indicate the number or location of the scattering clusters, it requires some additional information for application to typical environments.

2.3.5 Time-Varying Vector Channel Model

This model developed by *Raleigh* [40] provides small scale Rayleigh fading as well as theoretical spatial correlation properties. The regarded propagation environments are densely populated with large dominant reflectors. Thus, the channel can be characterized by L dominant reflectors at a particular instant of time. The received signal vector is given by

$$\mathbf{y}(t) = \sum_{l=0}^{L(t)-1} \mathbf{a}(\phi_l)\alpha_l(t)s(t-\tau) + \mathbf{n}(t) \tag{2.28}$$

where $\mathbf{a}(\phi)$ is the steering vector, $\alpha_l(t)$ is the complex amplitude, $s(t)$ is the modulated signal and $\mathbf{n}(t)$ is the additive noise vector. The complex amplitude is calculated by

$$\alpha_l(t) = \beta_l(t)\sqrt{\Gamma_l \Psi(\tau_l)} \tag{2.29}$$

where Γ_l and $\Psi(\tau_l)$ denote log-normal fading and the total received power delay profile, respectively. $\beta_l(t)$ is the complex intensity of the radiation pattern and is expressed by

$$\beta_l(t) = K \sum_{n=0}^{N_t-1} C_n(\phi_l) e^{\{j2\pi f_d \cos(\Omega_{n,l})t\}} \tag{2.30}$$

where N_t is the number of signal components contributing to the l th dominant reflector, K denotes the antenna gain and transmit signal power, $C_n(\phi_l)$ is the complex radiation on the n th component of the l th dominant reflecting surface in the direction of ϕ_l, f_d is the maximum Doppler shift, and $\Omega_{n,l}$ is the angle toward the n th component of the l th dominant reflector with respect to the motion of the mobile. The $\beta_l(t)$ shows a complex Gaussian distribution in all direction away from the mobile [40].

2.3.6 Two GSM Simulation Models

Spatial channel models for the typical Urban (TU) and the Band Urban (BU) are developed in the GSM standard. The received signal vector of these models is given by

$$\mathbf{y}(t) = \sum_{n=0}^{N-1} \alpha_n(t) e^{\{-j2\pi f_c \frac{d_n(t)}{c} + \Psi\}} s(t - \frac{l_n(t)}{c} + \Delta_t) \mathbf{a}(\phi_n(t)) \tag{2.31}$$

where N is the number of scatterers, f_c is the carrier frequency, c is the speed of light, $l_n(t)$ is the path propagation distance, Ψ is a random phase and Δ_t is random delay for each multipath component.

2.3.7 The Uniform Sectored Distribution Model

This model assumes that scatterers are uniformly distributed within an angle distribution of ϕ_{ad} and a radial range of Δ_R centered about the mobile which is shown in Fig. 2.8. The amplitude and phase associated with each scatterer are chosen from an uniform distribution of $[0, 1]$ and $[0, 2\pi]$, respectively. By approaching the number of scatterers to infinity, the signal fading envelope becomes *Rayleigh* with uniform phase.

2.3.8 Modified Saleh-Valenzuela's Model

Saleh and Valenzuela proposed a channel model for indoor environments observed in measured data [41]. The key result of them is the clustering phenomenon, i.e. multipath components arrive at the receiver antenna in groups. The resulting impulse response is expressed by

$$h(\tau) = \sum_{i=0}^{\infty} \sum_{j=0}^{\infty} \alpha_{i,j} \delta(\tau - T_i - \tau_{i,j}) \tag{2.32}$$

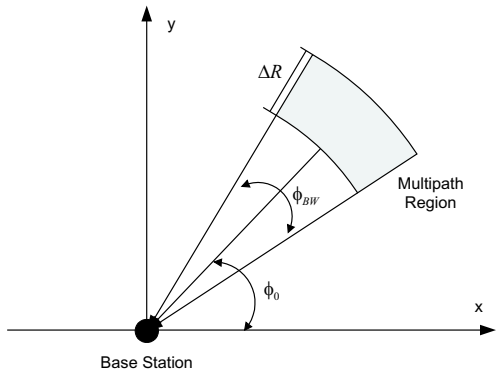

Figure 2.8: Geometry of the uniform sectored distribution.

where the indices i and j represent the sum over clusters and sum over rays within a cluster, respectively and T_i denotes cluster arrival time. The path attenuations $\alpha_{i,j}$ are regarded as Rayleigh distributed and their mean square value exhibits a double-exponential decaying function as

$$\overline{\alpha_{i,j}^2} = \overline{\alpha_{0,0}^2} \exp(-\frac{T_i}{\Gamma}) \exp(\frac{\tau_{i,j}}{\gamma}) \tag{2.33}$$

where Γ and γ are the cluster and ray time decay constants, respectively. Motivated by the model, the angular impulse response is proposed in [42] based on measurements assuming that TOA and AOA are statistically independent (i.e. $h(\tau, \phi) = h(\tau)h(\phi)$ is valid) and the angular impulse response is expressed by

$$f(\phi) = \frac{1}{\sqrt{2}\sigma_\phi} \exp(- \mid \frac{\sqrt{2}\phi}{\sigma_\phi} \mid) \tag{2.34}$$

where σ_ϕ is the RMS angle spread of each cluster.

2.3.9 Extended Tap-Delay-Line Method

A wideband space-time tap-delay-line model is proposed in [43] representing the channel impulse response by

$$h(\tau, t, \phi) = \sum_{i=0}^{K-1} \alpha_i(t)\delta(\tau - \tau_i)\delta(\phi - \phi_i) \tag{2.35}$$

where K, τ_i, α_i and ϕ_i are the number of taps, time delay, complex amplitude and AOA associated with i th tap, respectively. The joint density functions of the model should be determined by measurements.

2.3.10 Other Models

The elliptical subregions model proposed in [44] is primarily the same as the GBSB elliptical model described in section 2.3.3. The difference is that the elliptical scatterer density geometry

is partitioned into subregions, where each of the subregions is related to one range of the excess delay time.

The measurements based channel model is proposed by *Blanz. et al.* [45] by characterizing the propagation environments with respect to scattering points.

Applying ray-tracing techniques, propagation channels can be modeled deterministically by using site-specific information [46]. In spite of the high computational burden and the difficulty in obtaining detailed environment specific database, progress has been achieved.

2.4 Multi-Dimension Parameter Estimation Techniques

In this section, multi-dimensional joint parameter estimation techniques such as Unitary ESPRIT (Estimation of Signal Parameters via Rotational Invariance Technique), the SAGE (Space-Alternating Generalized Expectation) and other techniques are reviewed. The review is, however, emphasized on the SAGE algorithm, which was reported in the literature to have been applied successfully to measured channel data. In the following, the ideas behind those algorithms are outlined first. Then, the performance of the algorithms is discussed in conjunction with other known techniques.

2.4.1 SAGE Algorithm

This algorithm is originally based on the expectation maximization (EM) algorithm proposed in [47]. The SAGE algorithm was proposed by [48] and it was introduced recently by *Fleury et al.* [49] contributing to the application of mobile communication, especially to multi-dimensional parameter estimation for measured channel data.

Maximum Likelihood Estimation

Adapting the terms and keeping the notation described in [49], the received signal vector $\mathbf{Y}(t) \triangleq [Y_1(t), ..., Y_M(t)]^T$ at the output of the antenna array yields

$$\mathbf{Y}(t) = \sum_{\ell=1}^{L} \mathbf{s}(t;\theta_\ell) + \sqrt{\frac{N_0}{2}}\mathbf{N}(t), \tag{2.36}$$

where

$$\begin{aligned} \mathbf{s}(t;\theta_\ell) &:= [s_1(t;\theta_\ell), ..., s_M(t;\theta_\ell)] && (2.37)\\ &= \mathbf{a}(\phi_\ell)\alpha_\ell \exp\{j2\pi\nu_\ell t\}u(t-\tau_\ell), && (2.38) \end{aligned}$$

where $\mathbf{a}(\phi_\ell)$, α_ℓ, τ_ℓ and ν_ℓ are the steering vector, the complex amplitude, the relative delay, the Doppler frequency of ℓ th wave, respectively. L denotes the total number of impinging waves. θ_ℓ refers to the channel parameter set $\theta_\ell := \{\tau_\ell, \phi_\ell, \nu_\ell\}$ of the ℓ th wave. $\mathbf{N}(t) \in \mathbb{C}^{M\times 1}$ is a

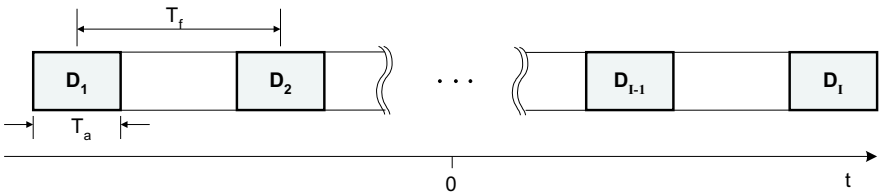

Figure 2.9: Observation window for $\mathbf{Y}(t)$.

spatially independent, complex white gaussian noise vector and N_0 is a positive constant. To keep a compact notation we also define

$$\mathbf{s}(t;\theta) \triangleq \sum_{\ell=1}^{L} \mathbf{s}(t;\theta_\ell) \tag{2.39}$$

where $\theta := [\theta_1, ..., \theta_L]$.

Consideration of the observation window: The $\mathbf{Y}(t)$ is observed over I window, whose duration is T_a, as depicted in Fig. 2.9. T_f denotes the spacing between the centers of two consecutive observation intervals and $1/T_f$ must be chosen larger than twice the maximum occurring Doppler frequency to fulfill the sampling theorem. The observation duration and the observation span are IT_a and $(I-1)T_f + T_a$. Selecting $T_f > T_a$, the Doppler resolution increases, while reducing the amount of measured data to be stored. Thus, the observation window is expressed with respect to its center of gravity as

$$D_0 = \bigcup_{i=1}^{I} [(i - ((I+1)/2))T_f - (T_a/2), (i - ((I+1)/2))T_f + (T_a/2)]. \tag{2.40}$$

The log-likelihood function of $\theta = [\theta_1, ..., \theta_L]$ given an observation $\mathbf{Y}(t) = \mathbf{y}(t)$ over D_0 is [49]

$$\Lambda(\theta;\mathbf{y}) \triangleq \frac{1}{N_0}[2\int_{D_0} \Re\{\mathbf{s}^H(t';\theta)\mathbf{y}(t')\}dt' - \int_{D_0} \|\mathbf{s}(t';\theta)\|^2 dt'], \tag{2.41}$$

where $\Re(.)$ and $\|.\|$ designate the real part and the norm of the argument, respectively. The maximum likelihood estimation (MLE) of θ can be given by

$$\hat{\theta}_{ML}(\mathbf{y}) \in \arg\max_{\theta}\{\Lambda(\theta;\mathbf{y})\} \tag{2.42}$$

The calculation of (2.42) is computationally intensive due to the high dimension of θ for large L and because of lack of a closed formula.

EM algorithm

Key terms to derive the EM algorithm are the *complete* (unobservable) and *incomplete* (observable) data. The individual signals of (2.36) can be expressed as

$$\mathbf{X}_\ell(t) = \mathbf{s}(t;\theta_\ell) + \sqrt{\frac{\beta_\ell N_0}{2}}\mathbf{N}_\ell(t), \ell = 1, ..., L. \tag{2.43}$$

The nonnegative parameters β_ℓ must be chosen to satisfy $\sum_{\ell=1}^{L}\beta_\ell = 1$, so that the set $\{\sqrt{\beta_1}\mathbf{N}_1(t), ..., \sqrt{\beta_L}\mathbf{N}_L(t)\}$ forms the decomposition of $\mathbf{N}(t)$. The $\mathbf{Y}(t)$ is related to the complete data according to

$$\mathbf{Y}(t) = \sum_{\ell=1}^{L}\mathbf{X}_\ell(t). \tag{2.44}$$

Corresponding to (2.41), the log-likelihood function of θ_ℓ for the observation $\mathbf{X}_\ell(t) = \mathbf{x}_\ell(t)$ over D_0 is

$$\Lambda(\theta_\ell;\mathbf{x}_\ell) \triangleq \frac{1}{\beta_\ell N_0}[2\int_{D_0}\Re\{\mathbf{s}^H(t';\theta_\ell)\mathbf{x}_\ell(t')\}dt' - \int_{D_0}\|\mathbf{s}(t';\theta_\ell)\|^2 dt'] \tag{2.45}$$

The estimation of the unobservable data $\mathbf{X}_\ell(t)$ is performed based on the incomplete data $\mathbf{Y}(t) = \mathbf{y}(t)$ and a previous estimate $\hat{\theta}'$, which is in turn defined by its conditional expectation given $\mathbf{Y}(t) = \mathbf{y}(t)$ assuming $\theta = \hat{\theta}'$ as expressed in (2.46).

- **Expectation step:** The estimation of the complete data according to [50] and [49]

$$\hat{\mathbf{x}}_\ell(t;\hat{\theta}') \triangleq E[\mathbf{X}_\ell(t) \mid \mathbf{y}] \tag{2.46}$$

$$= \mathbf{s}(t;\hat{\theta}'_\ell) + \beta_\ell\,\overbrace{[\mathbf{y}(t) - \sum_{\ell'=1}^{L}\mathbf{s}(t;\hat{\theta}'_{\ell'})]}^{noise\ estimate} \tag{2.47}$$

  Using the estimate $\hat{\mathbf{x}}_\ell(t;\hat{\theta}')$ from (2.47), the parameter vector θ_ℓ can be re-estimated in the maximization step by computing its MLE.

- **Maximization step:** The maximum likelihood estimate of the parameter set $\theta_\ell = \{\tau_\ell, \phi_\ell, \nu_\ell\}$ is given by

$$\hat{\theta}''_\ell = (\hat{\theta}_\ell)_{ML}(\hat{\mathbf{x}}_\ell(t;\hat{\theta}')) \tag{2.48}$$

  Putting (2.38) and (2.39) into (2.45), the MLE yields

$$(\widehat{\theta_\ell})_{ML}(\hat{\mathbf{x}}_\ell) = (\widehat{\tau_\ell, \phi_\ell, \nu_\ell})_{ML}(\hat{\mathbf{x}}_\ell) = \arg\max_{\{\tau,\phi,\nu\}}\{\mid z(\tau,\phi,\nu;\hat{\mathbf{x}}_\ell)\mid\} \tag{2.49}$$

$$(\hat{\alpha}_\ell)_{ML}(\hat{\mathbf{x}}_\ell) = \frac{1}{I\|\mathbf{a}((\hat{\phi}_\ell)_{ML}(\hat{\mathbf{x}}_\ell))\|^2 T_a P_u} z((\widehat{\tau_\ell, \phi_\ell, \nu_\ell})_{ML}(\hat{\mathbf{x}}_\ell);\hat{\mathbf{x}}_\ell) \tag{2.50}$$

$$
\begin{aligned}
z(\underbrace{\tau,\phi,\nu}_{\theta};\hat{\mathbf{x}}_\ell) &\equiv \int_{D_0} u^*(t'-\tau)\exp\{-j2\pi\nu t'\}\mathbf{a}^H(\phi)\hat{\mathbf{x}}_\ell(t')dt' \\
&= \sum_{i=1}^{I}\int_{D_i} u^*(t'-\tau)\exp\{-j2\pi\nu t'\}\mathbf{a}^H(\phi)\hat{\mathbf{x}}_\ell(t')dt'
\end{aligned}
\tag{2.51}
$$

SAGE algorithm

The SAGE algorithm can be seen as an extended version of the EM algorithm mainly in two aspects.

- *Space-Alternating*: A subset of the components of $\hat{\theta}$ (associated with *admissible hidden data*[1]) is updated at each iteration while keeping the other components fixed.
- *Generalization*: The mapping from the complete data space to the incomplete data space may be random rather than deterministic as primarily proposed [47].

The SAGE algorithm nevertheless maintains the remarkable monotonicity property of the EM algorithm. We now apply the SAGE algorithm to the parameter estimation of the propagation channels. [2]With $\beta_\ell = 1$, the expression for $\hat{\mathbf{x}}_\ell(t;\hat{\theta}')$ in (2.47) is simplified to

$$
\hat{\mathbf{x}}_\ell(t;\hat{\theta}') = \mathbf{y}(t) - \sum_{\substack{\ell'=1\\ \ell'\neq\ell}}^{L}\mathbf{s}(t;\hat{\theta}'_{\ell'})
\tag{2.52}
$$

The expression in (2.52) is suggesting to the implementation of the parallel interference cancellation (PIC) scheme. The sum signal of the (*L-1*) components is calculated using the current values of the parameter estimates. Hence, the signal from the ℓ th path can be well separated by subtracting this (*L-1*) sum signal from the incomplete signal $\mathbf{y}(t)$. The computational complexity is reduced by introducing the coordinate-wise updating procedure of the parameters and splitting the parameter sets into three subsets $\{\tau_\ell,\alpha_\ell\}$, $\{\phi_\ell,\alpha_\ell\}$ and $\{\nu_\ell,\alpha_\ell\}$ as suggested in [49].

$$
\hat{\tau}''_\ell = \arg\max_{\tau}\{|\ z(\tau,\hat{\phi}'_\ell,\hat{\nu}'_\ell;\hat{\mathbf{x}}_\ell(t;\hat{\theta}'))\ |\}, \tag{2.53}
$$

$$
\hat{\phi}''_\ell = \arg\max_{\phi}\{|\ z(\hat{\tau}''_\ell,\phi,\hat{\nu}'_\ell;\hat{\mathbf{x}}_\ell(t;\hat{\theta}'))\ |\}, \tag{2.54}
$$

$$
\hat{\nu}''_\ell = \arg\max_{\nu}\{|\ z(\hat{\tau}''_\ell,\hat{\phi}''_\ell,\nu;\hat{\mathbf{x}}_\ell(t;\hat{\theta}'))\ |\}, \tag{2.55}
$$

$$
\hat{\alpha}''_\ell = \frac{1}{IMT_aP_u}z(\hat{\tau}''_\ell,\hat{\phi}''_\ell,\hat{\nu}''_\ell;\hat{\mathbf{x}}_\ell(t;\hat{\theta}')) \tag{2.56}
$$

The SAGE algorithm discussed above was based on the signal model in the time domain. In some applications, it is more convenient to use the algorithm directly in frequency domain such as the channel sounding data using VNA technique. For the frequency domain SAGE (FDSAGE),

[1]Data are admissible for a given subset if they are complete for this subset under the hypothesis that the components of θ belonging to the complement of this subset are known.

[2]The conditional Fisher information of $\mathbf{X}_\ell(t)$ is maximized by setting $\beta = 1$ [49]

the expression (2.38) should be substituted by (2.5) for a stationary channel, whereby they are related each other by fourier transformation pair.
The resolution in delay, azimuth and Doppler frequency is defined to be the half-width of the main lobe of the magnitude of the corresponding correlation function. For ULA, the half-widths are given by [49]

$$\tau_c = T_s, \quad \phi_c = \frac{360^\circ}{\pi M} \quad \text{and } \nu_c = \frac{1}{IT_f}$$

Two waves are well separable when the condition is satisfied:

$$\Delta\tau > \tau_c \quad \text{or } \Delta\phi > \phi_c \quad \text{or } \Delta\nu > \nu_c$$

2.4.2 Unitary Multi-dimensional ESPRIT

The 1-D Unitary ESPRIT algorithm was extended to the multi-dimension parameter estimation problem, amongst others, by [51] and [52]. We summarize the algorithm proposed therein for 2-D joint angle estimation applied for uniform rectangular array (URA). Then, the formulation is adapted to the 2-D joint angle and delay estimation applied for ULA.
Let URA of $M \times L$ elements be locating in the x-y plane, equi-spaced by Δ_x in the x direction and Δ_y in the y direction. The array manifold can be expressed by

$$\mathbf{A}(\mu, \nu) = \mathbf{a}_M(\mu)\mathbf{a}_L^T(\nu) \tag{2.57}$$

where $\mathbf{a}_M(\mu)$ and $\mathbf{a}_L^T(\nu)$ are the array response vectors for the spatial frequencies μ and ν, respectively. The complex-valued array manifold can be transformed to the real-valued array manifold through the matrix [1] $\mathbf{Q}_{M(or\ L)}$ by

$$\begin{aligned} \mathbf{D}(\mu, \nu) &= \mathbf{Q}_M^H \mathbf{A}(\mu, \nu)\mathbf{Q}_L^* \\ &= \mathbf{d}_M(\mu)\mathbf{d}_L(\nu)^T \end{aligned} \tag{2.58}$$

The real-valued array response vector $\mathbf{d}(\mu, \nu)$ is related to $\mathbf{D}(\mu, \nu)$ with the $vec(.)$[2] operator by

$$\mathbf{d}(\mu, \nu) = vec(\mathbf{D}(\mu, \nu)). \tag{2.59}$$

We define

$$\mathbf{K}_1 = Re(\mathbf{Q}_{M-1}^H \mathbf{J}_1 \mathbf{Q}_M),\ \mathbf{K}_2 = Im(\mathbf{Q}_{M-1}^H \mathbf{J}_1 \mathbf{Q}_M), \tag{2.60}$$

$$\mathbf{K}_3 = Re(\mathbf{Q}_{L-1}^H \mathbf{J}_2 \mathbf{Q}_L),\ \mathbf{K}_4 = Im(\mathbf{Q}_{L-1}^H \mathbf{J}_2 \mathbf{Q}_L), \tag{2.61}$$

[1] The matrix $\mathbf{Q}_{M(orL)}$ is a sparse unitary matrix that transforms a vector into a real-valued vector [51].
[2] $vec(.)$ operator maps a $M \times L$ matrix to a $ML \times 1$ vector by stacking the columns of the matrix.

with

$$\mathbf{J}_1 = \begin{pmatrix} 1 & 0 & 0 & \dots & 0 & 0 \\ 0 & 1 & 0 & \dots & 0 & 0 \\ \vdots & \vdots & \vdots & \ddots & \vdots & \vdots \\ 0 & 0 & 0 & \dots & 1 & 0 \end{pmatrix} \in \mathbb{R}^{(M-1)\times M}$$

$$\mathbf{J}_2 = \begin{pmatrix} 0 & 1 & 0 & \dots & 0 & 0 \\ 0 & 0 & 1 & \dots & 0 & 0 \\ \vdots & \vdots & \vdots & \ddots & \vdots & \vdots \\ 0 & 0 & 0 & \dots & 0 & 1 \end{pmatrix} \in \mathbb{R}^{(L-1)\times L}$$

Here, the following relationships satisfy.

I. Invariance relationship for μ:

$$\{\tan(\frac{\mu}{2})\mathbf{K}_1\mathbf{D}(\mu,\nu) = \mathbf{K}_2\mathbf{D}(\mu,\nu)\} \overset{(2.59)}{\Longrightarrow} \{\tan(\frac{\mu}{2})\mathbf{K}_{\mu 1}\mathbf{d}(\mu,\nu) = \mathbf{K}_{\mu 2}\mathbf{d}(\mu,\nu)\}, \tag{2.62}$$

where $\mathbf{K}_{\mu 1}$ and $\mathbf{K}_{\mu 2}$ are related to $\mathbf{K}_1$ and $\mathbf{K}_2$ by

$$\mathbf{K}_{\mu 1} = \mathbf{I}_L \otimes \mathbf{K}_1; \quad \mathbf{K}_{\mu 2} = \mathbf{I}_L \otimes \mathbf{K}_2,$$

respectively. The operator $\otimes$ denotes the *Kronecker matrix product*[1].

II. Invariance relationship for ν:

$$\{\tan(\frac{\nu}{2})\mathbf{K}_3\mathbf{D}(\mu,\nu) = \mathbf{K}_4\mathbf{D}(\mu,\nu)\} \overset{(2.59)}{\Longrightarrow} \{\tan(\frac{\nu}{2})\mathbf{K}_{\nu 1}\mathbf{d}(\mu,\nu) = \mathbf{K}_{\nu 2}\mathbf{d}(\mu,\nu)\}, \tag{2.63}$$

where $\mathbf{K}_{\nu 1}$ and $\mathbf{K}_{\nu 2}$ are related to $\mathbf{K}_3$ and $\mathbf{K}_4$ by

$$\mathbf{K}_{\nu 1} = \mathbf{K}_3 \otimes \mathbf{I}_M; \quad \mathbf{K}_{\nu 2} = \mathbf{K}_4 \otimes \mathbf{I}_M,$$

respectively.

From (2.62) and (2.63), the following relationships are valid:

$$\mathbf{K}_{\mu 1}\mathbf{D}\mathbf{\Omega}_\mu = \mathbf{K}_{\mu 2}\mathbf{D} \tag{2.64}$$

$$\mathbf{K}_{\nu 1}\mathbf{D}\mathbf{\Omega}_\nu = \mathbf{K}_{\nu 2}\mathbf{D}, \tag{2.65}$$

where $\mathbf{\Omega}_\mu = diag[tan(\frac{\mu_1}{2}), ..., tan(\frac{\mu_P}{2})]$ and $\mathbf{\Omega}_\nu = diag[tan(\frac{\nu_1}{2}), ..., tan(\frac{\nu_P}{2})]$, respectively. Observing the output of URA at a time instance t_0, we obtain a snapshot matrix $\mathbf{S} \in \mathbb{C}^{M\times L}$. We collect the resulting column vector from $vec(\mathbf{S})$ as a column of a matrix $\mathbf{X}$, which denotes the $ML \times P$ complex-valued element space data matrix. We compute the matrix $\mathbf{Y} \in \mathbb{C}^{ML\times P}$ by

$$\mathbf{Y} = (\mathbf{Q}_L^H \otimes \mathbf{Q}_M^H)\mathbf{X} \tag{2.66}$$

[1] If $\mathbf{A}$ is a m by n matrix and $\mathbf{B}$ is a p by q matrix, then the Kronecker product $\mathbf{C} = \mathbf{A} \otimes \mathbf{B}$ is the mp by nq block matrix, $\mathbf{C} = (a)_{ij} \cdot \mathbf{B}$

We determine the matrix $\mathbf{E}_s$ as the P largest left singular vectors of the real-valued matrix $[Re\{\mathbf{Y}\}, Im\{\mathbf{Y}\}]$. Asymptotically, $\mathbf{E}_s = \mathbf{DT}$, where $\mathbf{T}$ is an unknown $P \times P$ real-valued matrix. Putting $\mathbf{D} = \mathbf{E}_s\mathbf{T}^{-1}$ into (2.62) and (2.63) yields the following relationship

$$\mathbf{K}_{\mu 1}\mathbf{E}_s\mathbf{\Psi}_\mu = \mathbf{K}_{\mu 2}\mathbf{E}_s, \ with \ \mathbf{\Psi}_\mu = \mathbf{T}^{-1}\mathbf{\Omega}_\mu\mathbf{T} \tag{2.67}$$

$$\mathbf{K}_{\nu 1}\mathbf{E}_s\mathbf{\Psi}_\nu = \mathbf{K}_{\nu 2}\mathbf{E}_s, \ with \ \mathbf{\Psi}_\nu = \mathbf{T}^{-1}\mathbf{\Omega}_\nu\mathbf{T} \tag{2.68}$$

Automatically pairing of the spatial frequency estimates can be given by following spectral decomposition

$$\mathbf{\Psi}_\mu + j\mathbf{\Psi}_\nu = \mathbf{T}^{-1}\{\mathbf{\Omega}_\mu + j\mathbf{\Omega}_\nu\}\mathbf{T}. \tag{2.69}$$

The algorithm is summarized as follows.:

1. Compute the real-valued matrix of signal eigenvector $\mathbf{E}_s \in \mathbb{R}^{M\times P}$ by utilizing the singular value decomposition (SVD) to the matrix $[Re\{\mathbf{Y}\}, Im\{\mathbf{Y}\}]$.

2. (i) Compute $\mathbf{\Psi}_\mu$ as the solution to the (M-1)L x P matrix equation as:

$$\mathbf{K}_{\mu 1}\mathbf{E}_s\mathbf{\Psi}_\mu = \mathbf{K}_{\mu 2}\mathbf{E}_s.$$

   (ii) Compute $\mathbf{\Psi}_\nu$ as the solution to the (M-1)L x P matrix equation as:

$$\mathbf{K}_{\nu 1}\mathbf{E}_s\mathbf{\Psi}_\nu = \mathbf{K}_{\nu 2}\mathbf{E}_s.$$

3. Compute $\lambda_i, i = 1, ..., P$ as the eigenvalues of the matrix $\mathbf{\Psi}_\mu + j\mathbf{\Psi}_\nu \in \mathbb{C}^{P\times P}$.

4. Compute spatial frequency estimates by

$$\mu_i = 2\tan^{-1}[Re(\lambda_i)], \ \ \nu_i = 2\tan^{-1}[Im(\lambda_i)], \ \ i = 1, ..., P.$$

The maximum number of sources 2-D Unitary ESPRIT can deal is given by

$$\min[M(L-1), \ L(M-1)].$$

The adaptation to joint delay and azimuth angle estimation for ULA can be simply executed as below:
With similar consideration to the URA case, the received signal from L paths associated with each antenna element can be viewed as $(L \times 1)$ column vectors (i.e. viewing as a virtual URA). For ULA, the receiver output vector is collected for L sampling time instances and these vectors can be stacked to form a single $(ML \times 1)$ snapshot vector using the $vec(.)$ operator. Collecting the resulting $(ML \times 1)$ column vector as a column vector of a matrix $\widetilde{\mathbf{X}}$, we can form the complex-valued element space data matrix for joint delay and azimuth angle estimation. Similarly, the matrix $\mathbf{Y}$ given in (2.66) must be substituted by the new matrix $\widetilde{\mathbf{Y}}$ as

$$\widetilde{\mathbf{Y}} = (\mathbf{Q}_L^H \otimes \mathbf{Q}_M^H)\widetilde{\mathbf{X}} \tag{2.70}$$

Using $\widetilde{\mathbf{Y}}$, the 2-D Unitary ESPRIT can be conducted as described previously. The relative delay is calculated by $\tau_i = \frac{\tan^{-1}[Im(\lambda_i)]\cdot N_s}{\pi}$, where $N_s = L \cdot P$. The main advantage of the Unitary ESPRIT is fast operation due to the close form expression.

2.4.3 Other Techniques

Other techniques proposed for joint parameter estimation are e.g. the multi-dimensional multiple signal classification (MUSIC) [53] and the joint angle and delay estimation (JADE) [54] for ULA. The JADE algorithm utilizes the ESPRIT-like shift invariance property and the knowledge of the transmitted pulse shape form for joint estimation. The multi-dimensional MUSIC exploits the eigenstructure of the covariance matrix of the input data like the one-dimensional MUSIC algorithm. For 2-D estimation problem (delay and azimuth angle) for ULA, the 2-D MUSIC algorithm shares the same idea of introducing a virtual array as shown for 2-D Unitary ESPRIT before. The algorithm is summarized briefly as below.
Consider the output of an ULA for ℓ th impinging wave. The collected signal output matrix $\mathbf{S} \in \mathbb{C}^{M\times K}$ after K sampling time instances is transformed to the vector $\tilde{\mathbf{x}}$ after stacking using $vec(\mathbf{S})$.

$$\tilde{\mathbf{x}} = \tilde{\mathbf{a}}(\phi_\ell, \tau_\ell)\alpha_\ell + \mathbf{n} \in \mathbb{C}^{MK\times 1}, \tag{2.71}$$

where K, $\tilde{\mathbf{a}}(\phi_\ell, \tau_\ell)$, α_ℓ and $\mathbf{n}$, respectively, denote the stacking factor, the steering vector, the complex amplitude and the spatially independent, complex white gaussian noise vector. Explicitly, $\tilde{\mathbf{a}}$ is given by

$$\tilde{\mathbf{a}} = \begin{pmatrix} u(t_1 - \tau_\ell) \\ \vdots \\ u(t_K - \tau_\ell) \\ ---------- \\ u(t_1 - \tau_\ell)\exp\{-j\pi\sin(\phi_\ell)\} \\ \vdots \\ u(t_K - \tau_\ell)\exp\{-j\pi\sin(\phi_\ell)\} \\ ---------- \\ \vdots \\ ---------- \\ u(t_1 - \tau_\ell)\exp\{-j\pi\sin(\phi_\ell)(M-1)\} \\ \vdots \\ u(t_K - \tau_\ell)\exp\{-j\pi\sin(\phi_\ell)(M-1)\}. \end{pmatrix}$$

When there are L waves, the array manifold $\widetilde{\mathbf{A}}$ yields:

$$\tilde{\mathbf{x}} = \widetilde{\mathbf{A}}\boldsymbol{\alpha} + \mathbf{n},\ \boldsymbol{\alpha} = [\alpha_1, ..., \alpha_L]^T, \tag{2.72}$$

with $\widetilde{\mathbf{A}} = [\tilde{\mathbf{a}}_1, ..., \tilde{\mathbf{a}}_L] \in \mathbb{C}^{MK\times L}$. Now, the 2-D MUSIC algorithm can be performed as follows:

1. Collect the vectors $\tilde{\mathbf{x}}_i,\ i = 1, ..., N$ into the data Matrix $\widetilde{\mathbf{X}} = [\tilde{\mathbf{x}}_1, ..., \tilde{\mathbf{x}}_N]$.
2. Estimate the covariance matrix $\hat{\mathbf{R}}_{xx} = \widetilde{\mathbf{X}}\widetilde{\mathbf{X}}^H \in \mathbb{C}^{MK \times MK}$
3. Decompose $\hat{\mathbf{R}}_{xx}$ via SVD and compute $MK - L$ eigenvectors $\mathbf{v}_j$.
4. Determine L peaks from $\Phi(\tau, \phi) = \frac{\tilde{\mathbf{a}}(\tau,\phi)\tilde{\mathbf{a}}(\tau,\phi)^*}{\sum_{j=L+1}^{MK}(\tilde{\mathbf{a}}(\tau,\phi)^*\mathbf{v}_j)^2}$, which corresponds L intersections of $\widetilde{\mathbf{A}}$.

The MUSIC type algorithms are associated with a multi-dimensional exhaustive search. The multi-dimensional Unitary ESPRIT and SAGE were applied in some channel measurements [28], [55]. A comparison between Unitary ESPRIT and SAGE algorithm has been conducted on propagation data generated by a ray-tracing model, which was based on indoor channel measurements [56]. Both algorithms were able to estimate all impinging wavefronts. It was found that Unitary ESPRIT appeared to be sensitive to the sub-array size, while SAGE algorithm was influenced by the choice of the angle and delay discretization.

Chapter 3

Simulative Analysis

The setup of a measurement system for radio channel measurements depends mainly on the emphasis of the investigation and available hardware components. Unless the measurement speed is a concern, VNA based on the frequency sweep technique is usually employed. The frequency sweep technique allows a wideband channel measurement since the achievable measurement time resolution is only limited by the swept RF-bandwidth, provided that the components used support the needed wideband characteristics.

Directional channel sounding (i.e. space-time channel measurement) is generally associated with high hardware requirements and cost. Particulary at 60 GHz, the cost and complexity of configuring a sounding system increase largely, when an antenna array is used. The RF components for 60 GHz are costly and some components are hardly commercially available. To extend to the spatial domain using a classical VNA technique would not be simple, because the antenna array outputs would have to be multiplexed for feeding to VNA input. Multiplexing at 60 GHz directly at the antenna array outputs appears to be difficult, since such a switching network is commercially not available, which otherwise would represent a great advantage in design. Instead, the IF-multiplexing technique can be deployed. Thus, the aimed use of a single RF-frontend can not be achieved and the complexity of system setup increases or at least remains as considered.

For measurement of complex-valued CIR, one should take great care of the synchronization of oscillators to obtain the correct phase response functions. The synchronization is usually carried out by applying a high precision reference source e.g. *rubidium atom normal* for both transmitter (Tx) and receiver (Rx) parts. Consider that a channel sounder should be designed based on available hardware components. If such a reference source is not available and the hardware components to be used are limited to narrowband measurement, wideband measurement can be achieved by concatenating the consecutively measured sub-channels. If the system lacks synchronization of oscillators, the concatenated wideband measurements would not represent correct CIRs. In this chapter, the channel reconstruction problem is investigated. More specifically, the channel concatenation methods are considered when wideband measurements are to be performed with a narrowband system that provides no perfect synchronization of oscillators.

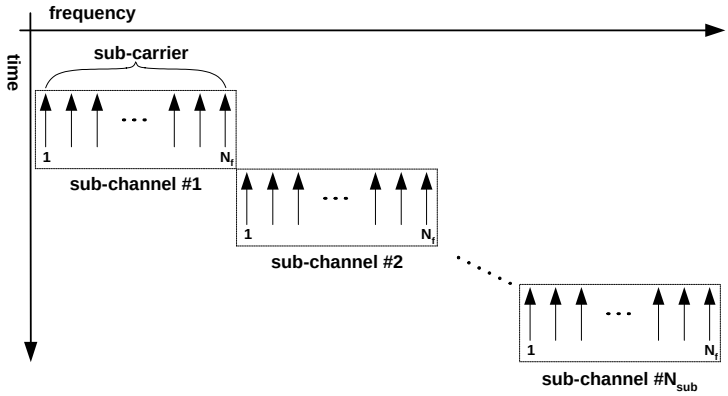

Figure 3.1: Measurement procedure by sweep of RF center frequency: total measurement RF-bandwidth B_{total} is divided into N_{sub} bandwidths. A sub-channel provides the bandwidth of B_{sub} consisting of N_f sub-carriers.

3.1 Problem Statement

Suppose that a narrowband system providing a measurement bandwidth of B_{sub} is used to achieve the wideband radio channel measurement of the total measurement bandwidth B_{total} by stepping the RF center frequency $(f_{start} + f_{c,n})$ in the frequency domain. Here, the following relations hold: $B_{sub} \ll B_{total}$, $B_{total} = N_{sub} \times B_{sub}$. N_{sub} denotes the number of consecutively measured sub-channels. Fig. 3.1 shows the described measurement procedure. Generally, the sub-channel measurements will exhibit phase discontinuities between them, if the oscillators at Tx and Rx used are not perfectly synchronized. Each of the measured sub-channels is affected by an unknown arbitrary constant phase offset $\xi_n \in [-\pi,\ \pi]$ resulting in a shift of its phase response function, which is caused by the carrier phase difference between Tx and Rx. Moreover, the sampling timing offsets will shift the phase response functions linearly by the bandwidth dependent factor η_n, so that the outermost frequency component suffers the largest.

The baseband representation of such a real channel frequency response function, $\widetilde{\mathbf{H}}_{total}$, obtained by using a narrowband channel sounder of bandwidth B_{sub} and applying an $1 \times M$ ULA can be expressed by

$$\mathbf{H}_n = \sum_{l=1}^{L} \mathbf{a}(\phi_l)\alpha_l \exp\{-j(2\pi[\mathbf{f}_v{}^T + f_{c,n}]\tau_l)\},\ \mathbf{H}_{total} = [\mathbf{H}_1, ..., \mathbf{H}_{N_{sub}}] \tag{3.1}$$

$$\widetilde{\mathbf{H}}_n = [\mathbf{H}_n + \mathbf{\Gamma}_n]\mathbf{D}_n \exp\{j\xi_n\},\ n = 1, ..., N_{sub}, \tag{3.2}$$

$$\widetilde{\mathbf{H}}_{total} = [\widetilde{\mathbf{H}}_1, ..., \widetilde{\mathbf{H}}_{N_{sub}}], \tag{3.3}$$

where $\widetilde{\mathbf{H}}_{total} \in \mathbb{C}^{M \times N_f \cdot N_{sub}}$ is the total channel matrix, $\widetilde{\mathbf{H}}_n \in \mathbb{C}^{M \times N_f}$ is the channel matrix for the n th sub-channel, $\mathbf{D}_n \in \mathbb{C}^{N_f \times N_f}$ is a square matrix whose elements are zeros except for its main diagonal elements given as $diag[\exp\{-j2\pi\eta_n\Delta_f\}, ..., \exp\{-j2\pi\eta_n N_f \Delta_f\}]^T$, $\mathbf{\Gamma}_n \in \mathbb{C}^{M \times N_f}$ denotes the additive noise matrix for the n th sub-channel, $\mathbf{f}_v{}^T = [\Delta_f, ..., N_f\Delta_f] \in \mathbb{R}^{1 \times N_f}$ is

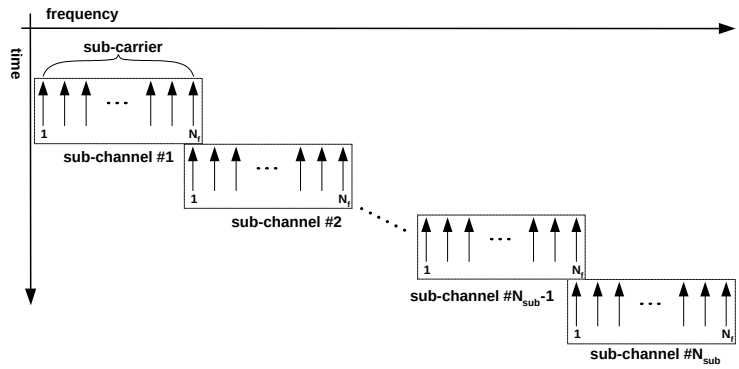

Figure 3.2: Measurement procedure for the overlap method.

the frequency vector of a sub-channel, $f_{c,n}$ is the n th center frequency, $N_f \in \mathbb{N}$ is the number of carriers within a sub-channel and $\Delta_f \in \mathbb{R}$ is the carrier spacing, respectively. If ξ_n and η_n are not sufficiently compensated, they degrade the measurement significantly or even make it impossible. In the following, compensation methods are considered, whereby it is assumed that the sampling timing offset η_n is effectively reduced to be negligibly small ($\eta_n \approx 0$) by an appropriate hardware-sided design approach. Thus, the consideration is mainly focused on compensation methods to the phase offset ξ_n.

3.2 Concatenation Methods

Two concatenation methods are considered: the overlap and the extrapolation method. In this section, the methods are described and their compensation errors are expressed by simple mathematical analysis.

3.2.1 Overlap Method

In this method, the measurement center frequencies ($f_{c,n} + f_{start}$) are so construed that at least one sub-carrier between any two consecutively measured sub-channels overlaps at frequency position (see Fig. 3.2). In case that one sub-carrier overlaps, the n th center frequency $f_{c,n}$ can be expressed by

$$f_{c,n} = \begin{cases} (n-1)B_{sub}, & \text{(a) overlapped sub-carriers} \\ (n-1)B_{sub} + (n-1)\Delta f, & \text{(b) equally spaced sub-carriers} \end{cases} \tag{3.4}$$

Each sub-channel $\mathbf{H}_n$ is perturbed individually by an arbitrary phase offset ξ_n caused by imperfect synchronization of the oscillators used. The unknown ξ_n must be estimated and subsequently compensated, which is referred to as *channel concatenation* or *reconstruction*. For the compensation procedure, we use the first sub-channel as the reference at first. Then, the previously compensated sub-channel is used for the compensation of the next sub-channel. For better understanding, we describe the notation and definitions used as follows.

Notation. 1. *For a matrix* $\mathbf{A} := (a_{i,j})_{1\le i\le M,\, 1\le j\le N}$*, we use the following notation:*

$$\begin{aligned}
\boldsymbol{A}[p,q;r,s] &:= (a_{i,j})_{p\le i\le q,\, r\le j\le s}\\
\boldsymbol{A}[p;r,s] &:= \boldsymbol{A}[p,p;r,s]\\
\boldsymbol{A}[p,q;r] &:= \boldsymbol{A}[p,q;r,r]\\
\boldsymbol{A}[p;q] &:= \boldsymbol{A}[p,p;r,r] = a_{p,q}
\end{aligned}$$

Property. 1. *For the overlap method, the following relationship is valid*

$$\mathbf{H}_n[1,M;N_f] = \mathbf{H}_{n+1}[1,M;1] \tag{3.5}$$

$$= \mathbf{H}_{total}[1,M;n\cdot(N_f-1)+1],\ 1\le n\le N_{sub}. \tag{3.6}$$

Definition. 1. *Let the total number of sub-channels be* N_{sub} *and each sub-channel consists of* N_f *sub-carriers. We define a matrix* $\mathbf{\Phi}_{H_{total}} \triangleq (\phi_{m,k})_{1\le m\le M,\, 1\le k\le N_{sub}\cdot N_f}$ *as the matrix containing true phase values of noiseless channels identified by*

$$\mathbf{\Phi}_{H_{total}} = \angle\, \mathbf{H}_{total} \in \mathbb{R}^{M\times N_{sub}\cdot N_f}. \tag{3.7}$$

We denote the matrix $\widetilde{\mathbf{\Phi}}_{H_n} = \angle\, \widetilde{\mathbf{H}}_n$ *from (3.2) as the measured real phase matrix. By neglecting the contribution of* $\mathbf{D}_n$ *(*$\mathbf{D}_n \approx diag[1,...,1]^T$*), the matrix* $\widetilde{\mathbf{\Phi}}_{H_n}$ *consists of the true phase, the contribution of the additive noise and the phase offset, which are resulted from the addition of the phasors (*$\widetilde{\mathbf{\Phi}}_{H_n} = \arctan[\frac{Im\{\mathbf{H}_n+\mathbf{\Gamma}_n\}}{Re\{\mathbf{H}_n+\mathbf{\Gamma}_n\}}] + \xi_n$*).*

To enable further analysis, we simplify the equation by decomposing the matrix $\widetilde{\mathbf{\Phi}}_{H_n}$ *as follows:* $\widetilde{\mathbf{\Phi}}_{H_n} = \mathbf{\Phi}_{H_n} + \mathbf{\Phi}_{\Gamma_n} + \xi_n$*, where* $\mathbf{\Phi}_{H_n}$*,* $\mathbf{\Phi}_{\Gamma_n}$ *and* ξ_n *are the true phase matrix, the phase matrix contributed by the addition of the additive noise phasor and the phase offset of the* n *th measurement instance at the outputs of ULA in the frequency domain, respectively.*

A. Estimation of the Phase Offset

The phase matrix $\widetilde{\mathbf{\Phi}}_{H_n}$ of the n th sub-channel according to *Definition. 1* is

$$\widetilde{\mathbf{\Phi}}_{H_n} = \mathbf{\Phi}_{H_n} + \mathbf{\Phi}_{\Gamma_n} + \xi_n \tag{3.8}$$

$$= \mathbf{\Phi}_{H_{total}}[1,M;(n-1)\cdot(N_f-1)+1, n\cdot(N_f-1)+1] + \mathbf{\Phi}_{\Gamma_n} + \xi_n. \tag{3.9}$$

Specifically for a particular frequency position k, the following identity holds true.

$$\mathbf{\Phi}_{H_n}[1,M;k] = \mathbf{\Phi}_{H_{total}}[1,M;(n-1)\cdot(N_f-1)+k],\ 1\le k\le N_f. \tag{3.10}$$

Since the overlap frequency positions (the outermost sub-carrier of $\mathbf{H}_n$ and the innermost sub-carrier of $\mathbf{H}_{n+1}$) are common, the following constraint between $\widetilde{\mathbf{\Phi}}_{H_n}$ and $\widetilde{\mathbf{\Phi}}_{H_{n+1}}$ from (3.5) and

(3.10) should be fulfilled

$$\widetilde{\mathbf{\Phi}}_{H_n}[1, M; N_f] \stackrel{!}{=} \widetilde{\mathbf{\Phi}}_{H_{n+1}}[1, M; 1]. \tag{3.11}$$

Using the relationship (3.11), the estimate $\hat{\xi}_{1,OL}$ for ξ_1 for the m th antenna array channel can be derived simply by

$$\begin{aligned}\hat{\xi}_{1,OL} &= \widetilde{\mathbf{\Phi}}_{H_1}[m; N_f] - \widetilde{\mathbf{\Phi}}_{H_2}[m; 1] \\ &\stackrel{(3.8),(3.10)}{=} (\mathbf{\Phi}_{H_{total}}[m; N_f] + \mathbf{\Phi}_{\Gamma_1}[m; N_f] + \xi_1) - (\mathbf{\Phi}_{H_{total}}[m; N_f] + \mathbf{\Phi}_{\Gamma_2}[m; 1] + \xi_2) \\ &= (\mathbf{\Phi}_{\Gamma_1}[m; N_f] - \mathbf{\Phi}_{\Gamma_2}[m; 1]) + (\xi_1 - \xi_2). \end{aligned} \tag{3.12}$$

Performing the estimation successively, we can express the estimate $\hat{\xi}_{n,OL}$ for the n th pair of sub-channels as

$$\begin{aligned}\hat{\xi}_{n,OL} &= \widetilde{\mathbf{\Phi}}_{H_n}[m; N_f] - \widetilde{\mathbf{\Phi}}_{H_{n+1}}[m; 1] \\ &= (\mathbf{\Phi}_{H_{total}}[m; n \cdot (N_f - 1) + 1] + \mathbf{\Phi}_{\Gamma_n}[m; N_f] + \xi_n) - \\ &(\mathbf{\Phi}_{H_{total}}[m; n \cdot (N_f - 1) + 1] + \mathbf{\Phi}_{\Gamma_{n+1}}[m; 1] + \xi_{n+1}) \\ &= (\mathbf{\Phi}_{\Gamma_n}[m; N_f] - \mathbf{\Phi}_{\Gamma_{n+1}}[m; 1]) + (\xi_n - \xi_{n+1}).\end{aligned}$$

B. Compensation of the Phase Offset

Using the estimates $[\hat{\xi}_{1,OL}, ..., \hat{\xi}_{N_{sub}-1,OL}]$, the phase compensation as well as the channel concatenation can be carried out. We denote the matrix $\widetilde{\mathbf{\Phi}}'_{H_n,OL}$ as the compensated phase matrix. The compensation procedure can be executed as below

$$\widetilde{\mathbf{\Phi}}'_{H_1,OL} = \widetilde{\mathbf{\Phi}}_{H_1} \tag{3.13}$$

$$\widetilde{\mathbf{\Phi}}'_{H_2,OL} = \widetilde{\mathbf{\Phi}}_{H_2} + \hat{\xi}_{1,OL} \tag{3.14}$$

$$\widetilde{\mathbf{\Phi}}'_{H_3,OL} = \widetilde{\mathbf{\Phi}}_{H_3} + (\hat{\xi}_{1,OL} + \hat{\xi}_{2,OL}) \tag{3.15}$$

$$\vdots$$

$$\widetilde{\mathbf{\Phi}}'_{H_n,OL} = \widetilde{\mathbf{\Phi}}_{H_n} + \underbrace{\sum_{k=1}^{n-1} \hat{\xi}_{k,OL}}_{\triangleq \mathbf{w}_{OL}[n]} \tag{3.16}$$

$$\vdots$$

$$\widetilde{\mathbf{\Phi}}'_{H_{N_{sub}},OL} = \widetilde{\mathbf{\Phi}}_{H_{N_{sub}}} + \sum_{k=1}^{N_{sub}-1} \hat{\xi}_{k,OL}, \tag{3.17}$$

where we denote $\mathbf{w}_{OL}[n]$ as the vector containing the compensation phase for n th sub-channel. The n th compensation error yields by observing $\mathbf{w}_{OL}[n]$ as

$$\begin{aligned}
\mathbf{w}_{OL}[n] &= \sum_{k=1}^{n-1} \hat{\xi}_{k,OL} \\
&= (\mathbf{\Phi}_{\Gamma_1}[m;N_f] - \mathbf{\Phi}_{\Gamma_2}[m;1]) + (\xi_1 - \xi_2) +, ..., +(\mathbf{\Phi}_{\Gamma_{n-1}}[m;N_f] - \mathbf{\Phi}_{\Gamma_n}[m;1]) + (\xi_{n-1} - \xi_n) \\
&= \sum_{k=1}^{n-1} \mathbf{\Phi}_{\Gamma_k}[m;N_f] - \sum_{k=2}^{n} \mathbf{\Phi}_{\Gamma_k}[m;1]) + (\xi_1 - \xi_n) \\
&= \underbrace{\sum_{k=1}^{n-1} (\mathbf{\Phi}_{\Gamma_k}[m;N_f] - \mathbf{\Phi}_{\Gamma_{k+1}}[m;1])}_{\triangleq \zeta_{n,OL}} + (\xi_1 - \xi_n),
\end{aligned} \tag{3.18}$$

where $(\xi_1 - \xi_n)$ is the relative phase offset and we denote $\zeta_{n,OL}$ as the compensation error for the n th pair of sub-channels for the overlap method. The concatenation of the compensated channel phases is performed as

$$\widetilde{\mathbf{\Phi}}'_{H_{total,OL}} = [\widetilde{\mathbf{\Phi}}'_{H_1,OL}[1,M;1,N_f-1], ..., \widetilde{\mathbf{\Phi}}'_{H_{N_{sub}},OL}[1,M;1,N_f-1]]. \tag{3.19}$$

3.2.2 Extrapolation Method

In contrast to the overlap method, the center frequencies are chosen as given in (3.4 (b)), so that the sub-carriers of all measured sub-channels are spaced equally. Due to the absence of common frequency positions, their phase information is determined by applying extrapolation technique. However, the lack of absolute phase reference leads to the same compensation procedure as the overlap method.

Definition. 2. *An operator extrap(.) is defined, which performs an extrapolation for a given input vector* $\mathbf{y_{in}} \in \mathbb{R}^{K\times 1}$ *of having values at equally spaced points* $x = x_0, ..., x_{k-1}$*, to be*

$$y_{out} \triangleq extrap(\mathbf{y}_{in}), \tag{3.20}$$

where y_{out} *denotes the extrapolation value at point* $x = x_k$*.*

Definition. 3. *For the operator extrap(.), the following relation is valid*

$$\begin{aligned}
y_{out} &= extrap(\mathbf{y}_{in}) \\
&= extrap(\mathbf{y}_0 + \mathbf{r} + q) \\
&= extrap(\mathbf{y}_0 + \mathbf{r}) + q.
\end{aligned} \tag{3.21}$$

$\mathbf{y}_0$ *and* $\mathbf{r}$ *denote the vectors containing the true and noise values, respectively. The constant* q

describes an offset value. Moreover, y_{out} is defined to be decomposed by

$$y_{out} \triangleq y_{true} + y_{error} + q, \tag{3.22}$$

where y_{true} and y_{error} describe the true value and an error term, respectively.

Adopting the notations used in Sec. 3.2.1, we determine the extrapolation values at $(n \cdot N_f + 1)$ th frequency positions for $\widetilde{\mathbf{\Phi}}_{H_n}$ across the m th row using (3.20) and collect the results into the vector $\mathbf{v}_n$ as

$$\mathbf{v}_n[m] = extrap(\widetilde{\mathbf{\Phi}}_{H_n}[m; 1, N_f]),\ m = 1, ..., M. \tag{3.23}$$

Applying (3.22), the decomposition of $\mathbf{v}_n[m]$ and $\widetilde{\mathbf{\Phi}}_{H_{n+1}}[m; 1]$ yields as

$$\mathbf{v}_n[m] = \underbrace{\mathbf{\Phi}_{H_{total}}[m; n \cdot N_f + 1]}_{true\ phase} + \underbrace{\mathbf{z}_n[m]}_{error} + \xi_n, \tag{3.24}$$

$$\widetilde{\mathbf{\Phi}}_{H_{n+1}}[m; 1] = \mathbf{\Phi}_{H_{total}}[m; n \cdot N_f + 1] + \mathbf{\Phi}_{\Gamma_{n+1}}[m; 1] + \xi_n. \tag{3.25}$$

Since $\mathbf{v}_n[m]$ and $\widetilde{\mathbf{\Phi}}_{H_{n+1}}[m; 1]$ should provide phase values at common frequency position, the following constraint should be satisfied

$$\mathbf{v}_n[m] \stackrel{!}{=} \widetilde{\mathbf{\Phi}}_{H_{n+1}}[m; 1]. \tag{3.26}$$

A. Estimation of the Phase Offset

Using (3.26), the estimate $\hat{\xi}_{1,EP}$ for ξ_1 can be performed by

$$\begin{aligned}\hat{\xi}_{1,EP} &= \mathbf{v}_1[m] - \widetilde{\mathbf{\Phi}}_{H_2}[m; 1] \\ &= (\mathbf{\Phi}_{H_{total}}[m; N_f + 1] + \mathbf{z}_1[m] + \xi_1) - (\mathbf{\Phi}_{H_{total}}[m; N_f + 1] + \mathbf{\Phi}_{\Gamma_2}[m; 1] + \xi_2) \\ &= (\mathbf{z}_1[m] - \mathbf{\Phi}_{\Gamma_2}[m; 1]) + (\xi_1 - \xi_2).\end{aligned} \tag{3.27}$$

The estimate $\hat{\xi}_{n,EP}$ for ξ_n can be determined by

$$\begin{aligned}\hat{\xi}_{n,EP} &= \mathbf{v}_n[m] - \widetilde{\mathbf{\Phi}}_{H_{n+1}}[m; 1] \\ &= (\mathbf{\Phi}_{H_{total}}[m; n \cdot N_f + 1] + \mathbf{z}_n[m] + \xi_n) - (\mathbf{\Phi}_{H_{total}}[m; n \cdot N_f + 1] + \mathbf{\Phi}_{\Gamma_{n+1}}[m; 1] + \xi_{n+1}) \\ &= \mathbf{z}_n[m] - \mathbf{\Phi}_{\Gamma_{n+1}}[m; 1]) + (\xi_n - \xi_{n+1}).\end{aligned} \tag{3.28}$$

B. Compensation of the Phase Offset

Using the estimates $[\hat{\xi}_{1,EP}, ..., \hat{\xi}_{N_{sub}-1,EP}]$ and denoting the matrix $\widetilde{\mathbf{\Phi}}'_{H_n,EP}$ as the compensated phase matrix, the compensation can be performed by

$$\begin{aligned}
\widetilde{\mathbf{\Phi}}'_{H_1,EP} &= \widetilde{\mathbf{\Phi}}_{H_1} \\
\widetilde{\mathbf{\Phi}}'_{H_2,EP} &= \widetilde{\mathbf{\Phi}}_{H_2} + \hat{\xi}_{1,EP} \\
\widetilde{\mathbf{\Phi}}'_{H_3,EP} &= \widetilde{\mathbf{\Phi}}_{H_3} + (\hat{\xi}_{1,EP} + \hat{\xi}_{2,EP}) \\
&\vdots \qquad (3.29)
\end{aligned}$$

$$\widetilde{\mathbf{\Phi}}'_{H_n,EP} = \widetilde{\mathbf{\Phi}}_{H_n} + \underbrace{\sum_{k=1}^{n-1} \hat{\xi}_{k,EP}}_{\triangleq \mathbf{w}_{EP}[n]} \qquad (3.30)$$

$$\vdots \qquad (3.31)$$

$$\widetilde{\mathbf{\Phi}}'_{H_{N_{sub}},EP} = \widetilde{\mathbf{\Phi}}_{H_{N_{sub}}} + \sum_{k=1}^{N_{sub}-1} \hat{\xi}_{k,EP}, \qquad (3.32)$$

where we denote $\mathbf{w}_{EP}[n]$ as the vector containing the compensation phase for n th sub-channel and $\mathbf{w}_{EP}[n]$ is to be expressed explicitly

$$\begin{aligned}
\mathbf{w}_{EP}[n] &= \sum_{k=1}^{n-1} \hat{\xi}_{k,EP} \qquad (3.33) \\
&= \sum_{k=1}^{n-1} \mathbf{z}_k[m] - \sum_{k=2}^{n} \mathbf{\Phi}_{\Gamma_k}[m;1] + (\xi_1 - \xi_n) \qquad (3.34) \\
&= \underbrace{\sum_{k=1}^{n-1} \{\mathbf{z}_k[m] - \mathbf{\Phi}_{\Gamma_{k+1}}[m;1]\}}_{\triangleq \zeta_{n,EP}} + (\xi_1 - \xi_n) \qquad (3.35)
\end{aligned}$$

where $(\xi_1 - \xi_n)$ is the relative phase offset and we denote $\zeta_{n,EP}$ as the compensation error for the n th pair of sub-channels for the extrapolation method. The concatenation of the compensated channel phases is performed as

$$\widetilde{\mathbf{\Phi}}'_{H_{total},EP} = [\widetilde{\mathbf{\Phi}}'_{H_1}[1, M; 1, N_f], ..., \widetilde{\mathbf{\Phi}}'_{H_{N_{sub}}}[1, M; 1, N_f]]. \qquad (3.36)$$

3.3 Simulative Examination

3.3.1 Preliminary Consideration

The impact of phase offset on channel parameters such as delay spread and mean excess delay were investigated. Simulation study has been conducted using synthetic channels, where phase

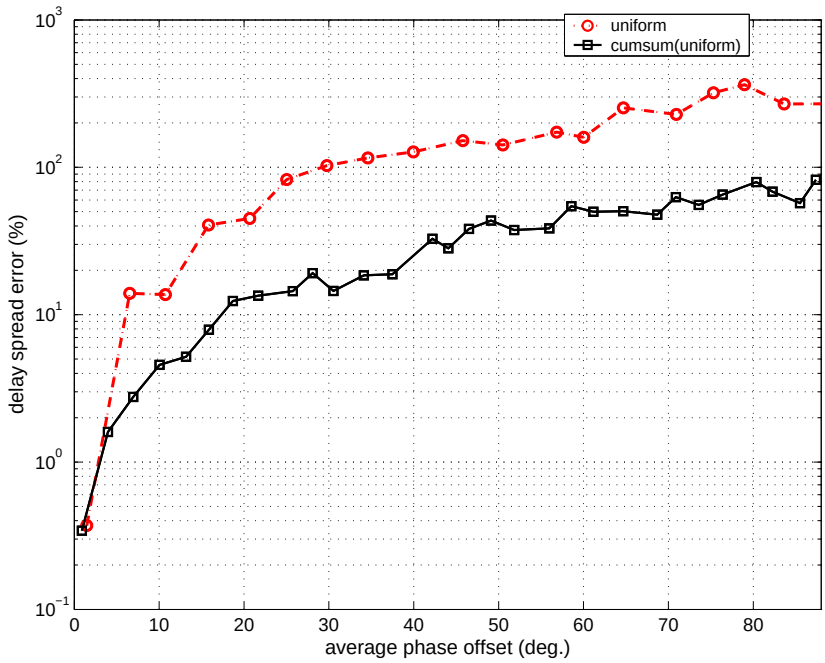

Figure 3.3: Relative delay spread error in (%) as a function of the averaged phase offset over 160 sub-channels.

offsets were assumed to be uniformly distributed over N_{sub} sub-channels. Furthermore, another distribution was used obtaining by cumulative sum of a realization of uniform distribution. The sampling timing offset discussed previously was preconditioned to be negligibly small, so that this has no effect on the results. In Fig. 3.3 and 3.4, the results are depicted showing the delay spread errors and mean excess delay errors relative to the reference values (channels free from phase offsets) in % as functions of the averaged phase offset over 160 sub-channels.

Large deviations with respect to two considered distributions are observed despite the same average phase offset, where the reason is related to the characteristic of the distributions of phase offset. If the phase offsets were changing rapidly as it is the case for uniform distribution, they produced undesired spurious peaks in the impulse response functions as shown in Fig. 3.5. These peaks are usually higher than the noise floor, so that they lead to an incorrect calculation of the delay spread. Hence, the error statistics of an uniform phase offset distribution are more sensitive to a small change of phase offset. The second distribution would be more a reasonable one when regarding it as the distribution of compensation error, since the compensation errors for the considered concatenation methods are expressed by the cumulative sum of phase offset estimates. From Fig. 3.3, an average phase offset of about 4° is needed to reach a relative delay spread error smaller than 1.6 % for both cases. A delay spread error of about 7.9 % corresponds to an average phase offset of 15.9° for the latter distribution, while a mean excess delay error less than 7 % is approached for an average phase offset of 22°. Though these values provide no immediate connection to the performance of the considered concatenation methods, it points out some useful clues for further investigation. In the following, the feasibility of considered

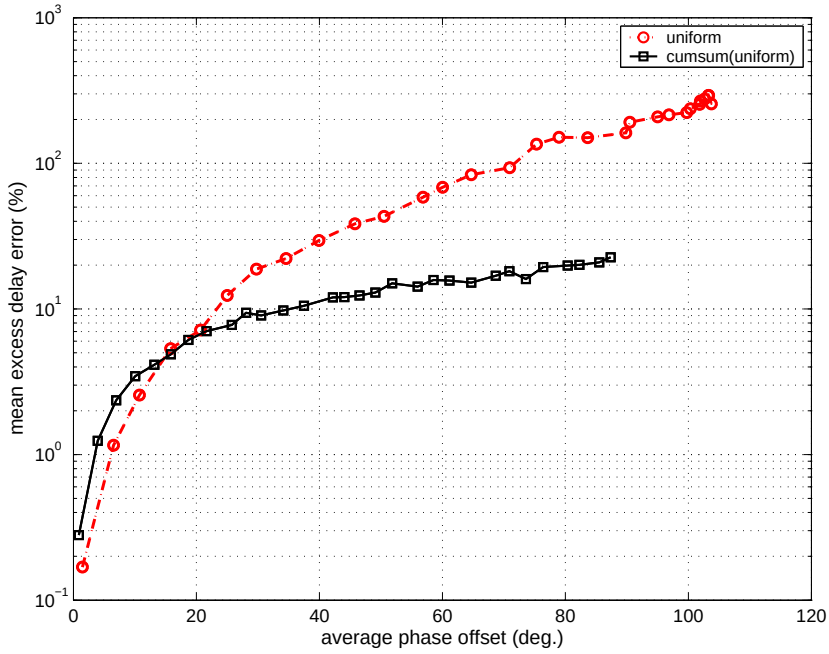

Figure 3.4: Relative mean excess delay error in (%) as a function of the averaged phase offset over 160 sub-channels.

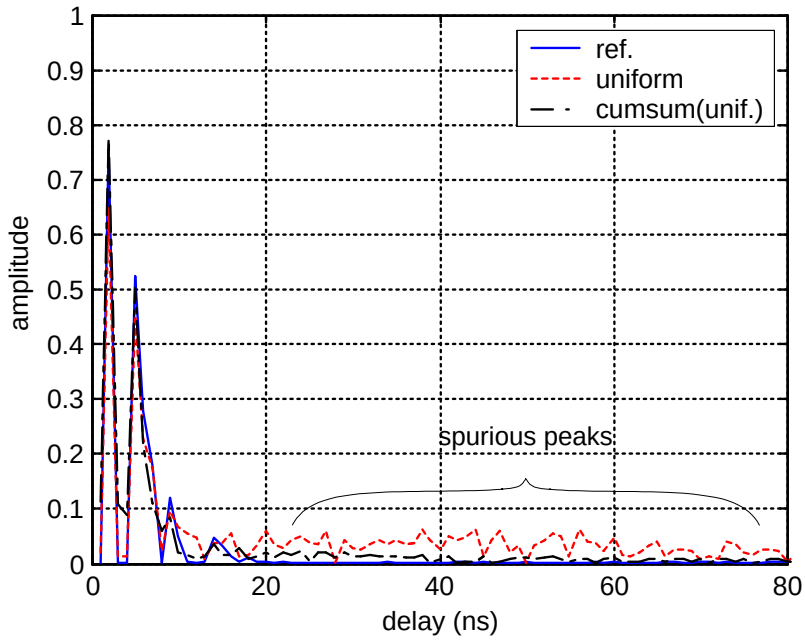

Figure 3.5: Spurious peaks cased by rapidly changing phase offsets.

concatenation methods is dwelt upon by means of simulative error analysis.

3.3.2 Simulative Error Analysis

A. Description of the Simulation Environment

The simulation environment, in which the channel concatenation methods were examined by using synthetic channels, is described as follows. In synthetic channels, path attenuations were supposed to be Ricean distributed and the K-factors were chosen in the value range $[0, 40]$ dB. Exponential decaying power delay profiles were used. The number of multipath components was selected at each simulation run from [20, 60] and the rays were located within a maximum delay window of 80 ns, which corresponds to an excess delay length of about 24 m. A synthetic channel consisting of $N_{sub} = 160$ sub-channels was defined in the frequency domain and a sub-channel provides a constant bandwidth of B_{sub} of 6 MHz. The N_f sub-carriers were equally spaced within a sub-channel, where N_f was chosen from the set $N_f \in \{8, 16, 32\}$. The phase offset $\xi_n \in [-\pi, \pi]$ was assumed to be randomly distributed over N_{sub} sub-channels. Phase noises for M antenna channels were added from independently generated wiener process with a variance of 4.65° [57], [58]. The SNR values were varied between $[20, 70]$ dB in 5 dB steps. A total of 500 simulation runs were conducted to obtain a statistically reasonable statement. To the extrapolation method, the linear, spline and cubic extrapolation techniques were combined: first, $N_f - 1$ sub-carriers were used to determine the extrapolated phase at the N_f th frequency position. Since the phase at the N_f th frequency position is known, the extrapolated phases at the N_f th frequency position from three methods were compared with the known phase by minimum mean square error (MMSE) sense. Then, the method providing minimum error was used for the estimation of the current sub-channel and the procedure was repeated up to sub-channel N_{sub}. As performance measure, the RMS error between the specified and the estimated phase offset was computed, which is referred to as the *RMS compensation error of phase offset* in the following. The errors of channel parameters such as delay spread, excess delay and coherence bandwidth were also used for the error statistics. Thereby, the error statistics between *noiseless channel* and the *reference channel*, which was perturbed by gaussian noise and phase noise apart from phase offset, were used for the lower bounds throughout the simulation study. The notation and definitions useful for better understanding are described as follows.

Notation. 2. *We use subscripts "OL", "EP", "ref" and "rel" of a symbol as the attributes for "overlap method", "extrapolation method", "reference" and "relative", respectively.*

Definition. 4. *We define the RMS compensation error of phase offset over N_{sub} sub-channels averaged over N_{run} simulation runs as follows:*

$$\zeta_{rms,x} \triangleq \frac{1}{N_{run}} \sum_{i=1}^{N_{run}} \left\{ \sqrt{\frac{1}{N_{sub}} \sum_{n=1}^{N_{sub}} \zeta_{i,n,x}^2} \right\}. \tag{3.37}$$

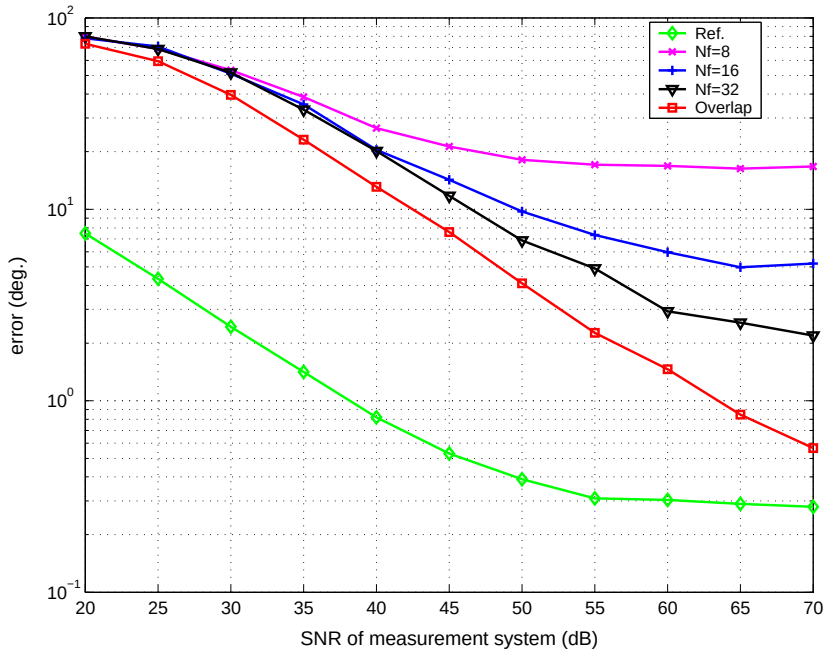

Figure 3.6: RMS compensation errors as functions of the SNR values of the measurement system: extrapolation method with N_f={8, 16, 32}, overlap method and reference as lower bound.

The letter "x" in subscript stands for the attributes for "OL", "EP" and "ref", respectively. The $\zeta_{i,n,OL}$ and $\zeta_{i,n,EP}$ are given in (3.18) and (3.35), respectively. The $\zeta_{rms,ref}$ is denoted as the average RMS phase error for the reference channel.

Definition. 5. *We define the relative error as follows:*

$$e_{ds,rel,x} \triangleq \frac{1}{N_{run}} \sum_{i=1}^{N_{run}} \sqrt{\frac{1}{N_{sub}} \sum_{n=1}^{N_{sub}} \left\{ \frac{\sigma_{\tau,i,n} - \sigma_{\tau,i,n,x}}{\sigma_{\tau,i,n}} \times 100 \right\}^2}, \tag{3.38}$$

where $e_{ds,rel,x}$ is denoted as the relative RMS delay spread error over N_{sub} sub-channels averaged over N_{run} simulation runs, computed relative to the reference value ($\sigma_{\tau,i,n}$) obtained from noiseless channel. In the exact same manner, $e_{ed,rel,x}$ and $e_{cbw,rel,x}$ are defined as the relative RMS errors of the mean excess delay and the coherence bandwidth, respectively. The letter "x" in subscript stands for the attributes for "OL", "EP" and "ref", respectively.

B. Results of the Simulative Error Analysis I

Simulation results are shown in Fig. 3.6, which shows the RMS compensation errors as functions of the SNR values of the measurement system for the reference channel ($\zeta_{rms,ref}$) and reconstructed channels using the extrapolation method ($\zeta_{rms,EP}$) and overlap method ($\zeta_{rms,OL}$). For the extrapolation method, results from using different values of N_f are also included.

The $\zeta_{rms,EP}$ is reduced strongly with increasing number of sub-carriers. For $N_f = 8$, the improvement with increased SNR is quite small, particulary above 40 dB indicating that error

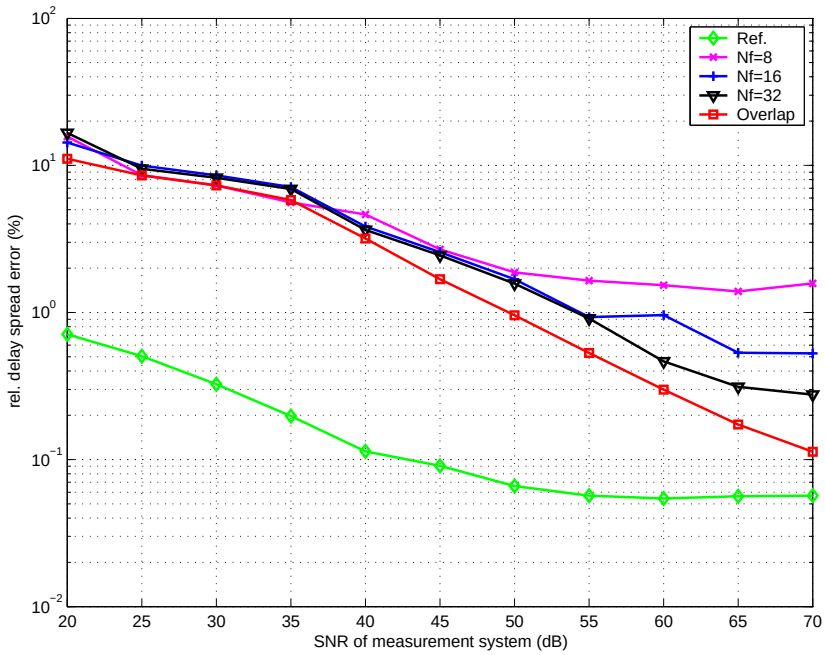

Figure 3.7: Relative RMS delay spread errors as functions of SNR values of measurement system.

introduced by the extrapolation is the dominant part and the result is thus virtually biased to a certain value. Performance is largely improved when N_f is doubled. For $N_f = 16$, errors less than 10° can be achieved above 50 dB. The improvement is more obvious for $N_f = 32$ providing an error less than 5° above 50 dB. The overlap method outperforms others overall and is showing a consistently decreasing characteristic with increasing SNR values. At SNR=70 dB, the $\zeta_{rms,OL}$ approaches to a value of 0.57°, where the lower bound ($\zeta_{rms,ref}$) is given by 0.28°.

A similar trend is reflected in Fig. 3.7, which shows the relative RMS delay spread errors as functions of the SNR values. The reference error ($e_{ds,rel,ref}$) is bounded to 0.05 %. A visibly large improvement is beginning from SNR=35 dB for all methods and above 50 dB, differences are noticeable between the different values of N_f. The overlap method outperforms the others with constantly decreasing characteristic.

The relative RMS mean excess delay errors ($e_{ed,rel,x}$) are shown in Fig. 3.8. The reference relative RMS mean excess delay error ($e_{ed,rel,ref}$) is bounded to 0.043 %. This trend is highly similar to the previously discussed error characteristics. An error less than 2 % can be achieved, if the SNR value is larger than 50 dB for all versions.

Fig. 3.9 illustrates the relative RMS coherence bandwidth errors ($e_{cbw,rel,x}$). The errors are decreasing consistently with increasing SNR values and an error less than 0.26 % can be reached above 45 dB for all versions, which are all close to reference values, $e_{cbw,rel,ref}$.

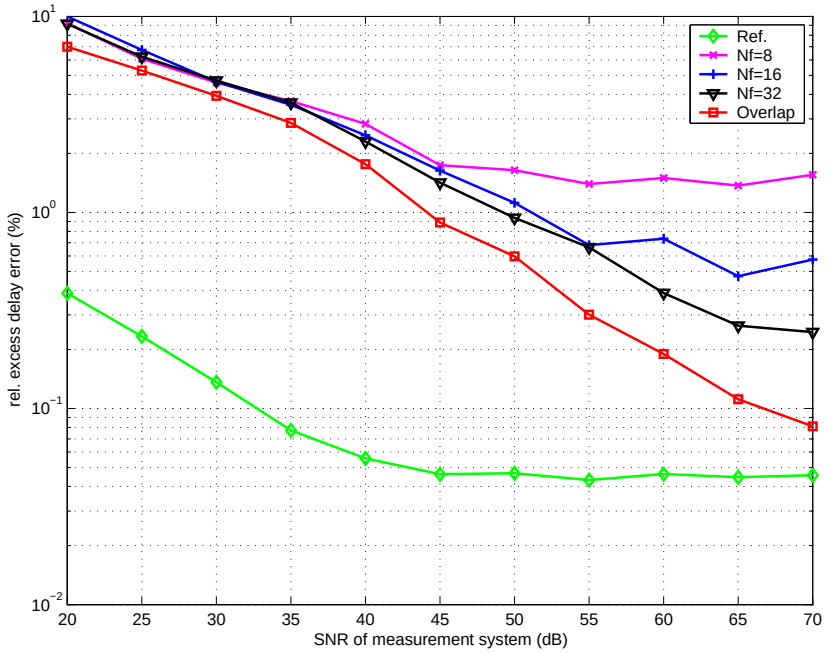

Figure 3.8: Relative RMS mean excess delay errors as functions of the SNR values of the measurement system.

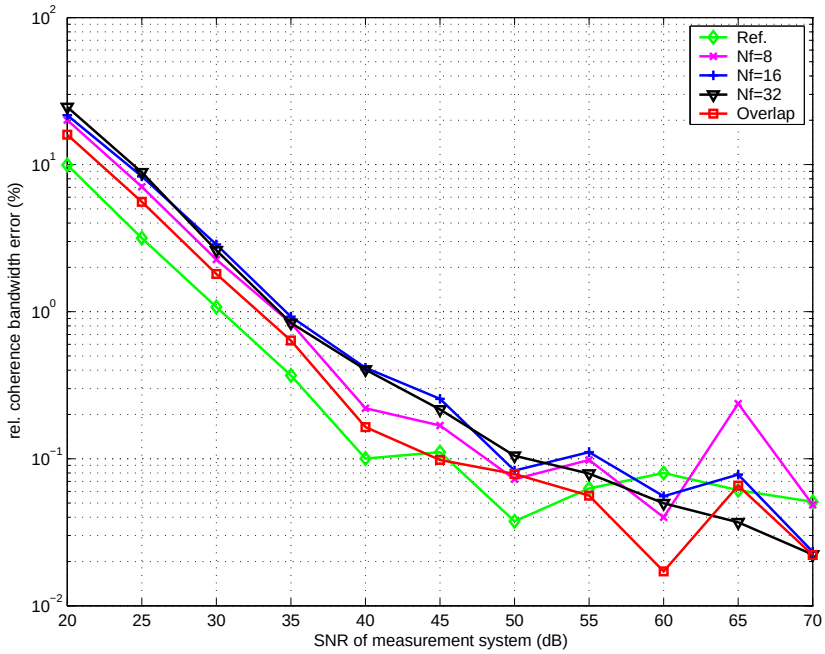

Figure 3.9: Relative RMS coherence bandwidth errors as functions of the SNR values of the measurement system: errors in number of frequency separation.

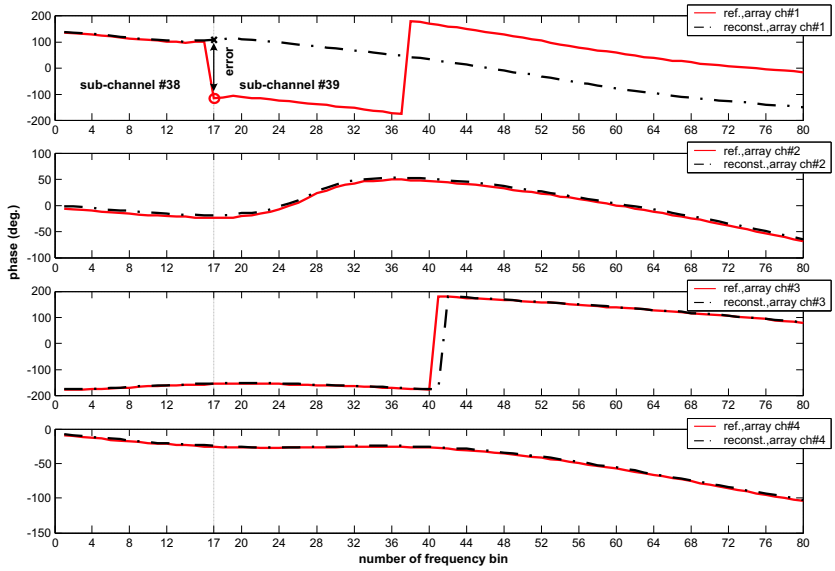

Figure 3.10: Illustration of using redundant information: phase response functions of the reference and reconstructed array channels at sub-channel # 38 and # 39. The phase response function of array channel # 1 exhibits a large error propagation beginning at sub-channel # 39.

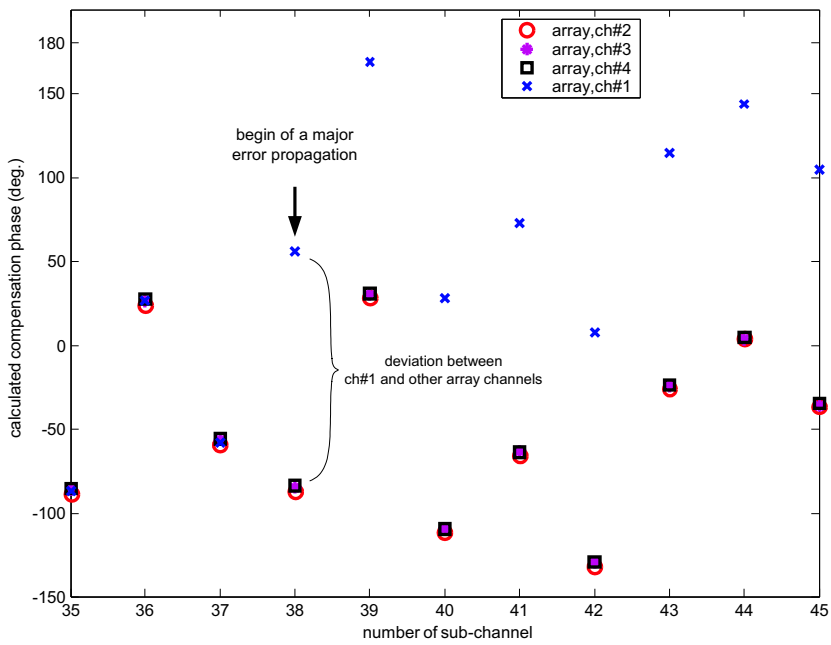

Figure 3.11: Illustration of compensation phases (calculated according to (3.33)) relating to Fig. 3.10: a large estimation error between sub-channel #38 and #39 for array channel # 1, the estimates of other array channels lie closely.

C. Enhancement # 1: Exploiting Redundant Information from the Antenna Array

The biggest concern when applying concatenation methods is appearing of large errors at an early state of the compensation procedure. Such errors may produce a consequential loss by propagating up to the last sub-channel and contribute majorly to the error statistics. However, motivated by the fact that due to the added spatial phases of antenna array channels the run of their phase curves should be different, this redundant information can be exploited for achieving an improvement. It was frequently observed that a large estimation error occurs at a single array channel at a certain sub-channel while the estimates of other array channels are reliable. An illustrative situation is shown in Fig. 3.10, where a large estimation error caused by a rapidly changing phase between the sub-channel # 38 and # 39 of the first array channel is observed. Fig. 3.11 shows the calculated compensation phases (according to (3.33)) relating to that. This example results in an average phase error of 111.5°, while the error is dramatically reduced to 4.9° by avoiding only this breakdown. The key idea for mitigating an error propagation is to identify and exclude such outliers. The situation displayed in Fig. 3.11 suggests utilizing combinatoric distance measures for detecting such outliers. Thus, an algorithm is formulated to identify such situations and to control outliers, which is summarized for ULA with M=4 below.

Summary of the algorithm

Algorithm for outlier detection and combination of compensation phases.

Let a matrix be $\mathbf{W} := (w_{m,k})_{1\leq m\leq M,\, 1\leq k\leq N_{sub}-1}$, whose column and row elements are the compensation phases for M antenna elements and N_{sub} sub-channels according to (3.33), respectively.
We define a vector $\mathbf{c} \in \mathbb{R}^{(N_{sub}-1)\times 1}$ to collect combined compensation phases.
1: initialize: $M \Longleftarrow 4$, $k \Longleftarrow 0$, $\mathbf{c}[1] = 0$
2: **repeat**
3: $k \Longleftarrow k + 1$
4: Calculate the combinatoric distances between $\mathbf{W}[1, M; k]$ (i.e. between row elements of k th column) by

$$\begin{aligned} d_{(1,2)} &\Longleftarrow |\mathbf{W}[1;k] - \mathbf{W}[2;k]|,\ d_{(1,3)} \Longleftarrow |\mathbf{W}[1;k] - \mathbf{W}[3;k]|, \\ d_{(1,4)} &\Longleftarrow |\mathbf{W}[1;k] - \mathbf{W}[4;k]|,\ d_{(2,3)} \Longleftarrow |\mathbf{W}[2;k] - \mathbf{W}[3;k]|, \\ d_{(2,4)} &\Longleftarrow |\mathbf{W}[2;k] - \mathbf{W}[4;k]|,\ d_{(3,4)} \Longleftarrow |\mathbf{W}(3,k) - \mathbf{W}[4;k]|, \\ \mathbf{d} &\Longleftarrow [d_{(1,2)}, ..., d_{(3,4)}]^T. \end{aligned}$$

5: Group the elements of $\mathbf{d}$ in vectors $\mathbf{g}_1, ..., \mathbf{g}_4 \in \mathbb{R}^{3\times 1}$, whose subscripts are associated with the number of antenna array, respectively, by:

$$\begin{aligned} \mathbf{g}_1 &\Longleftarrow [d_{(1,2)}, d_{(1,3)}, d_{(1,4)}]^T, \mathbf{g}_2 \Longleftarrow [d_{(1,2)}, d_{(2,3)}, d_{(2,4)}]^T, \\ \mathbf{g}_3 &\Longleftarrow [d_{(1,3)}, d_{(2,3)}, d_{(3,4)}]^T, \mathbf{g}_4 \Longleftarrow [d_{(1,4)}, d_{(2,4)}, d_{(3,4)}]^T \end{aligned}$$

6: Search of $\mathbf{d}$ for three largest elements and save the results in vector $\mathbf{s}$
7: Case differentiation for determining outlier and combination of compensation phases:

Case 1. **if** $(\sum_{i=1}^{3} \mathbf{g}_1[i] = \sum_{i=1}^{3} \mathbf{s}[i])$, **then**
outlier is most likely $\mathbf{W}$[1;k], $\mathbf{c}(k) \Longleftarrow \frac{1}{3}\sum_{i=2,i\neq 1}^{4} \mathbf{W}[i;k]$.
end if

Case 2. **if** $(\sum_{i=1}^{3} \mathbf{g}_2[i] = \sum_{i=1}^{3} \mathbf{s}[i])$, **then**
outlier is most likely $\mathbf{W}[2;k]$, $\mathbf{c}(k) \Longleftarrow \frac{1}{3}\sum_{i=1,i\neq 2}^{4} \mathbf{W}[i;k]$.
end if

Case 3. **if** $(\sum_{i=1}^{3} \mathbf{g}_3[i] = \sum_{i=1}^{3} \mathbf{s}[i])$, **then**
outlier is most likely $\mathbf{W}[3;k]$, $\mathbf{c}(k) \Longleftarrow \frac{1}{3}\sum_{i=1,i\neq 3}^{4} \mathbf{W}[i;k]$.
end if

Case 4. **if** $(\sum_{i=1}^{3} \mathbf{g}_4[i] = \sum_{i=1}^{3} \mathbf{s}[i])$, **then**

outlier is most likely $\mathbf{W}[4;k]$, $\mathbf{c}(k) \Longleftarrow \frac{1}{3}\sum_{i=1,i\neq 4}^{4} \mathbf{W}[i;k]$.

end if

Otherwise: Outlier is badly identifiable. Search $\mathbf{d}$ for smallest element and denote it as q.

Case 5.1. **if** $(d_{(1,2)} = q)$, **then**

$\mathbf{c}[k] \Longleftarrow \frac{1}{2}\sum_{i=1,i\neq 3,i\neq 4}^{4} \mathbf{W}[i;k]$.

end if

Case 5.2. **if** $(d_{(1,3)} = q)$, **then**

$\mathbf{c}[k] \Longleftarrow \frac{1}{2}\sum_{i=1,i\neq 2,i\neq 4}^{4} \mathbf{W}[i;k]$.

end if

Case 5.3. **if** $(d_{(1,4)} = q)$, **then**

$\mathbf{c}[k] \Longleftarrow \frac{1}{2}\sum_{i=1,i\neq 2,i\neq 3}^{4} \mathbf{W}[i;k]$.

end if

Case 5.4. **if** $(d_{(2,3)} = q)$, **then**

$\mathbf{c}[k] \Longleftarrow \frac{1}{2}\sum_{i=1,i\neq 1,i\neq 4}^{4} \mathbf{W}[i;k]$.

end if

Case 5.5. **if** $(d_{(2,4)} = q)$, **then**

$\mathbf{c}[k] \Longleftarrow \frac{1}{2}\sum_{i=1,i\neq 1,i\neq 3}^{4} \mathbf{W}[i;k]$.

end if

Case 5.6. **if** $(d_{(3,4)} = q)$, **then**

$\mathbf{c}[k] \Longleftarrow \frac{1}{2}\sum_{i=1,i\neq 1,i\neq 2}^{4} \mathbf{W}[i;k]$.

end if

Otherwise:

$\mathbf{c}[k] \Longleftarrow \frac{1}{4}\sum_{i=1}^{4} \mathbf{W}[i;k]$.

end if

8: **until** $k < N_{sub}$.

It should be noted that there is generally still a risk to come to a wrong decision, even if the case differentiation described in algorithm is fulfilled, when the majority of the phase offset estimates $\mathbf{W}[m;k]$ (see Sec. 3.3.2) at a certain sub-channel are outliers providing similar values, while a single channel provides a nearly true value. The probability of such a case, however, can be presumed to be rare. For the case that two of four phase offset estimates of $\mathbf{W}[m;k]$ are breakdowns, an additional case differentiation is necessary (see algorithm step# 7, case differentiation: otherwise). If the outliers provide distinguishable values from each other and the good-natured values have a similar range of values, then the probability of coming to a right

decision should be high. However, there are still cases in which it is still not possible to ensure a right decision.

D. Enhancement # 2: Forward-Backward Compensation

Previously, the first sub-channel was used as the reference for phase offset estimation and compensation. Multiple references may not be used, because the concatenated parts would not be interrelated any more. Thus, the optimal choice of reference sub-channel is taking the sub-channel number as $N_{sub}/2$ as shown in Fig. 3.12. Splitting the phase matrix $\widetilde{\Phi}_{H_{total}}$ in two parts relative to the middle reference sub-channel, the phase offset estimation as well as compensation, respectively, are performed in forward and backward directions

$$\tilde{\mathbf{\Phi}}_{H_{total}} = [\overbrace{\tilde{\mathbf{\Phi}}_{H_1}, ..., \tilde{\mathbf{\Phi}}_{H_{N_{ref}-1}}, \tilde{\mathbf{\Phi}}_{H_{N_{ref}}}}^{backward\ compensation}, \tilde{\mathbf{\Phi}}_{H_{N_{ref}+1}}, ..., \tilde{\mathbf{\Phi}}_{H_{N_{sub}}}] \tag{3.39}$$

$$= [\tilde{\mathbf{\Phi}}_{H_1}, ..., \tilde{\mathbf{\Phi}}_{H_{N_{ref}-1}}, \underbrace{\tilde{\mathbf{\Phi}}_{H_{N_{ref}}}, \tilde{\mathbf{\Phi}}_{H_{N_{ref}+1}}, ..., \tilde{\mathbf{\Phi}}_{H_{N_{sub}}}}_{forward\ compensation}], \tag{3.40}$$

where $N_{ref} := \frac{N_{sub}}{2}$. The error expression for each compensation direction is equivalent to (3.35). The compensation error of the extrapolation method for the n th compensation step can be given by

$$\zeta_{n,EP,fw} = \sum_{k=1}^{n} \{\mathbf{z}^{fw}_{N_{ref}+k-1}[m] - \mathbf{\Phi}_{\Gamma_{N_{ref}+k}}[m;1]\} + (\xi_{N_{ref}} - \xi_{N_{ref}+k}) \tag{3.41}$$

$$\zeta_{n,EP,bw} = \sum_{k=1}^{n} \{\mathbf{z}^{bw}_{N_{ref}+k-1}[m] - \mathbf{\Phi}_{\Gamma_{N_{ref}-k}}[m;N_f]\} + (\xi_{N_{ref}} - \xi_{N_{ref}-k}), \tag{3.42}$$

where $\mathbf{z}^{fw}_{N_{ref}+k-1}[m]$ and $\mathbf{z}^{bw}_{N_{ref}+k-1}[m]$ denote the error terms after applying extrapolation technique for forward and backward directions, respectively.

Due to the reduced number of compensations, error propagation is mitigated resulting in the improvement of error statistic. It can be expected that the compensation errors are distributed symmetrically with respect to the reference channel N_{ref}.

E. Results of Simulative Error Analysis II

The proposed enhancements (enhancement#1 and #2) were embedded in the extrapolation method and its reliability has been assessed by means of simulation study. The same simulation environment as described in Sec. 3.3.2 was used. Moreover, error statistics were obtained also using the same performance measures as for the previous error analysis in Sec. 3.3.2. First, only the enhancement described in Sec. 3.3.2.C was combined with the extrapolation method and the results are discussed in the following. A total of 500 simulation runs were conducted and the results are presented in Fig. 3.13 through Fig. B.2. In Fig. 3.13, the RMS compensation errors

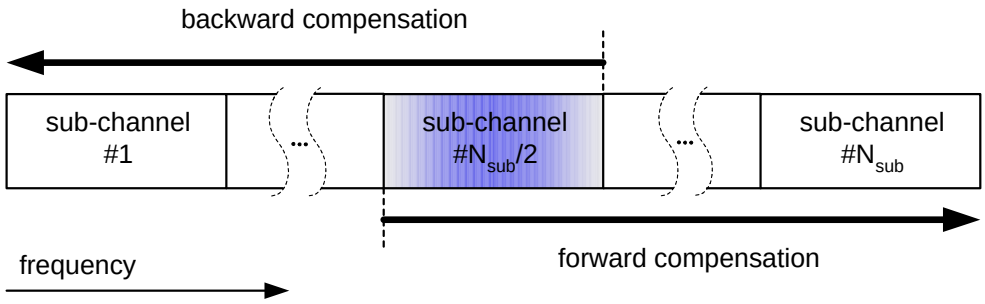

Figure 3.12: Enhancement # 2: forward and backward compensation by splitting the phase matrix $\widetilde{\Phi}_{H_{total}}$ in two parts relative to the middle reference sub-channel.

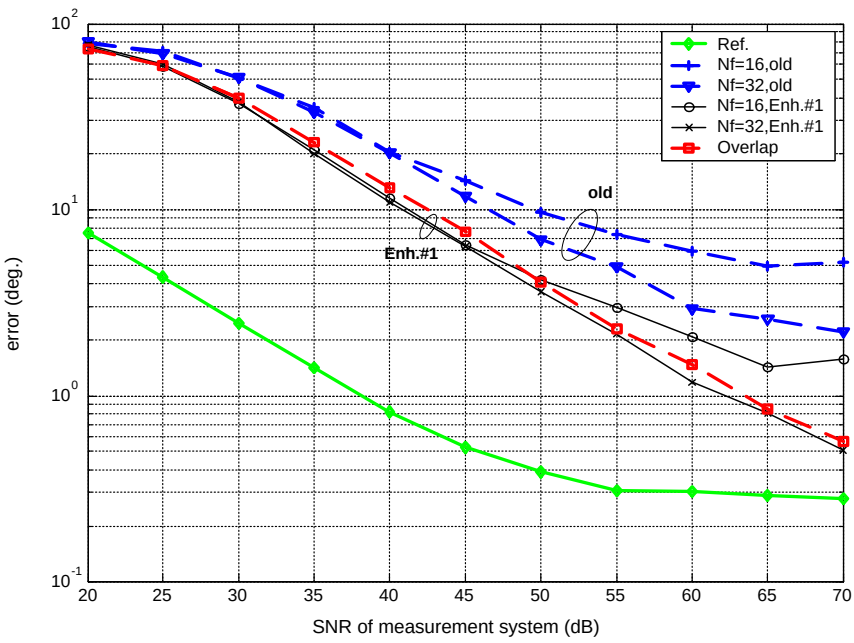

Figure 3.13: RMS compensation errors vs. SNR values: the previous extrapolation method (legend "old": see Sec. 3.3.2.B and Fig. 3.6) and improved extrapolation method (legend "Enh.#1": enhancement summarized in Sec. 3.3.2.C), overlap method and reference error statistics as lower bounds, $N_{sub} = 160$, $N_f = \{16, 32\}$.

as function of the SNR values are shown. In the graphic, different versions (different N_f with legend "old") of previous extrapolation method are compared with the improved versions (legend "Enh.#1"). The results of the overlap method and reference error statistics are also shown. An evidently large performance enhancement for the improved versions over all SNR range can be observed. The performance of the improved versions of the extrapolation method is very close to the error statistics of the overlap method and even slightly better when $N_f = 32$ used. Comparing the two versions (previous and improved extrapolation method) for $N_f = 16$ shows an improvement greater than 5° at SNR=50 dB. Inspecting the standard deviation (see. Table. B.1) the reliability of the improved versions is demonstrated even more obviously: the improved version ("$N_f = 16$, Enh.#1" in Fig. 3.13) has a standard deviation of 3.14° at SNR=50 dB, while the previous version ("$N_f = 16$, old" in Fig. 3.13) provides 15.66° for the same SNR value. Even the improved version with $N_f = 16$ outperforms the previous version with $N_f = 32$. Using $N_f = 32$, the improved version of the extrapolation method tends to result in approaching the lower bound value with increased SNR. Corresponding to the above, the error statistics for the $e_{ds,rel,x}$ and $e_{ed,rel,x}$ show a resembling characteristic (see. Fig. B.1 and Fig. B.2). The statistics for all improved versions are indistinguishable from those of the overlap method by SNR=50 dB showing decreasing characteristics with increased SNR, although small differences in performance appear between them over SNR=50 dB. A $e_{ds,rel,EP}$ and a $e_{ed,rel,EP}$ less than 1 % and 0.55 %, respectively, can be achieved with the improved version of the extrapolation method above SNR=50 dB. The reliability can be also observed by inspecting the standard deviation values given in Table. B.2 and Table. B.3. The statistics for coherence bandwidth are less conclusive for comparison of the methods, since they are very close to each other.
Here, the forward and backward compensation scheme was additionally embedded along with the previous enhancement. The results are depicted in Fig. 3.14 through Fig. 3.17. With both enhancements, the two versions of the extrapolation method (legend "Enh.#1+Enh.#2", N_f={16, 32}) clearly outperform the overlap method providing a RMS compensation error and a standard deviation of 2.81° and 1.96°, respectively, at 50 dB with $N_f = 16$, while the overlap method shows the corresponding statistics as 4.58° and 4.35°, respectively. However, the difference becomes less explicitly with increasing SNR. Also, noticeably large improvement can be observed compared to the enhancement discussed previously (see Fig. 3.13). Other results ($e_{ds,rel,x}$, $e_{ed,rel,x}$ and $e_{cbw,rel,x}$) follow the tendency discussed above widely as shown in Fig. 3.15 and Fig. 3.17. The standard deviations are summarized in Table. 3.1 through Table. 3.3.

F. Error Statistics depending on the Number of Concatenations

The simulative error analysis with respect to the number of concatenations was performed. The simulation environment used was mostly the same as described previously, but the number of concatenations, N_c, was changed using a value from the set $N_c \in \{5, 10, 20, 40, 80, 160\}$. The total number of generated sub-channels was, however, the same for all variations as $N_{sub} = 160$, but corresponding to the current N_c value, only N_c sub-channels were perturbed by phase

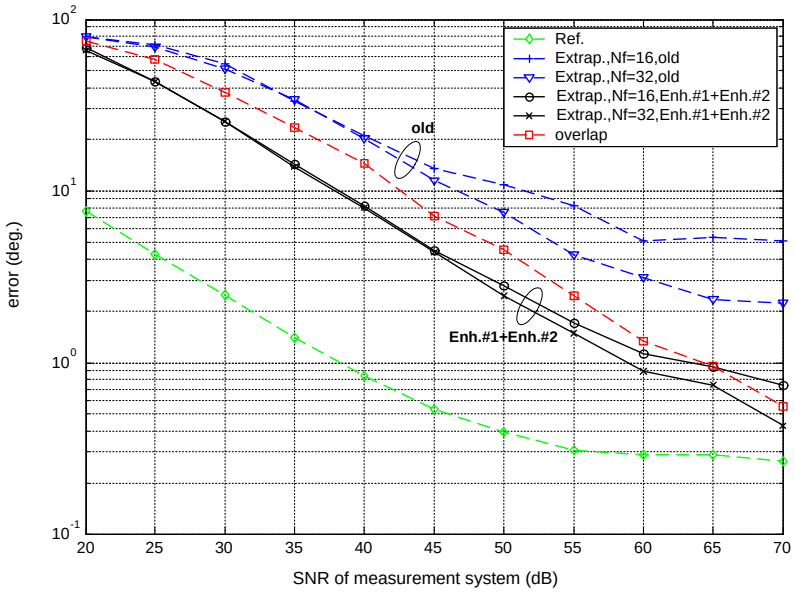

Figure 3.14: RMS compensation errors vs. SNR values: previous extrapolation method (legend "old": results from Sec. 3.3.2.B) and improved extrapolation method (legend "Enh.#1+Enh.#2": both enhancements described in Sec. 3.3.2.C and Sec. 3.3.2.D), overlap method and reference error statistics as lower bounds, $N_{sub} = 160$, $N_f = \{16, 32\}$

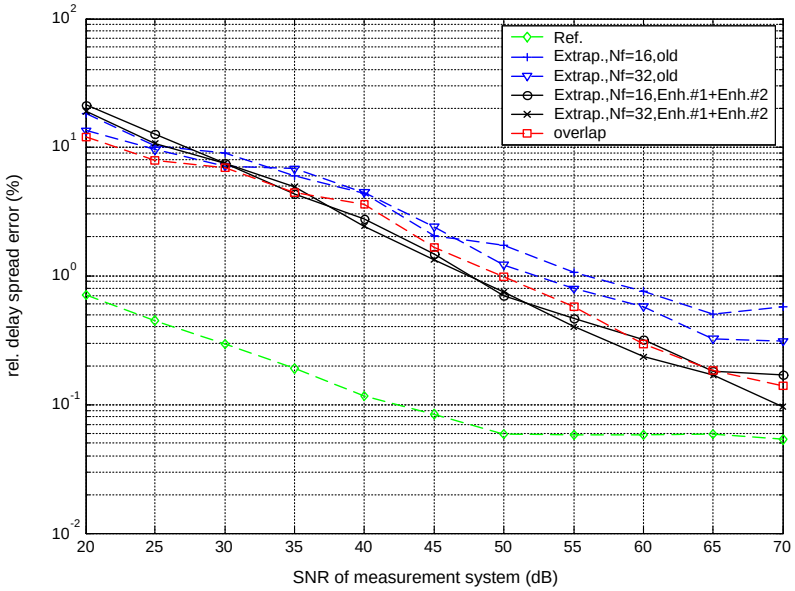

Figure 3.15: Relative RMS delay spread errors vs. SNR values: previous extrapolation method (legend "old": results from Sec. 3.3.2.B) and improved extrapolation method (legend "Enh.#1+Enh.#2": both enhancements described in Sec. 3.3.2.C and Sec. 3.3.2.D), overlap method and reference error statistics as lower bounds, $N_{sub} = 160$, $N_f = \{16, 32\}$.

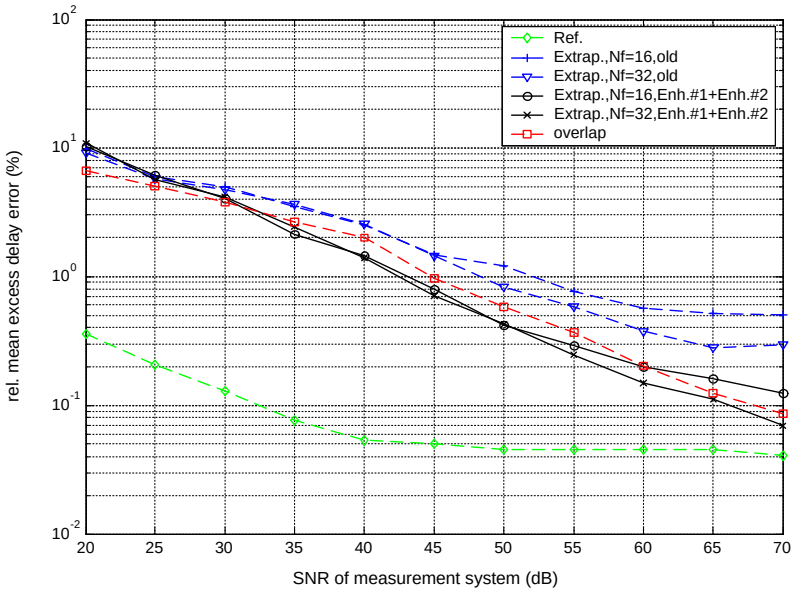

Figure 3.16: Relative RMS mean excess delay errors vs. SNR values: previous extrapolation method (legend "old": results from Sec. 3.3.2.B) and improved extrapolation method (legend "Enh.#1+Enh.#2": both enhancements described in Sec. 3.3.2.C and Sec. 3.3.2.D), overlap method and reference error statistics as lower bounds, $N_{sub} = 160$, $N_f = \{16, 32\}$.

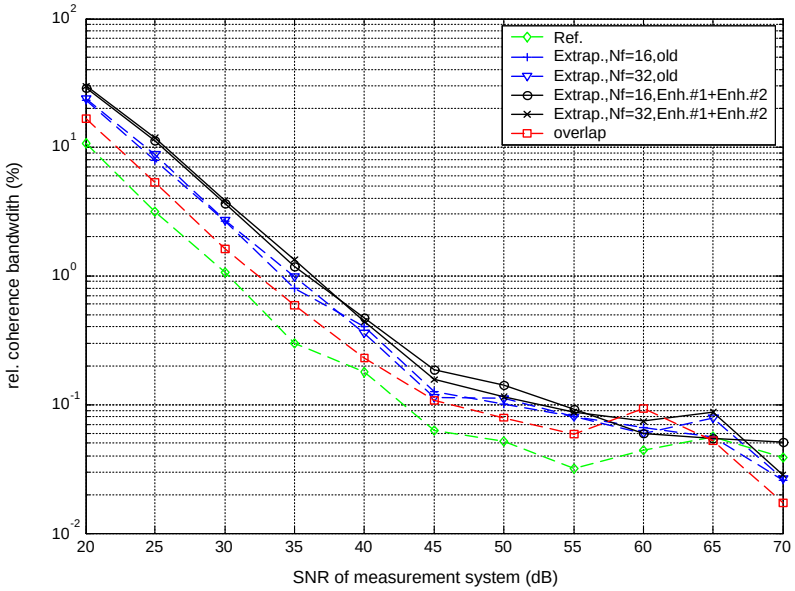

Figure 3.17: Relative RMS coherence bandwidth errors vs. SNR values: previous extrapolation method (legend "old": results from Sec. 3.3.2.B) and improved extrapolation method (legend "Enh.#1+Enh.#2": both enhancements described in Sec. 3.3.2.C and Sec. 3.3.2.D), overlap method and reference error statistics as lower bounds, $N_{sub} = 160$, $N_f = \{16, 32\}$.

SNR (dB)	$N_f = 16$, old	$N_f = 16$, Enh.#1+Enh.#2	$N_f = 32$, old	$N_f = 32$, Enh.#1+Enh.#2	Overlap	Reference
30	29.06	11.48	28.04	12.73	24.98	0.53
40	17.33	4.31	15.50	3.80	13.12	0.22
50	15.66	1.96	10.56	1.09	4.35	0.17
60	9.66	1.17	7.79	0.47	1.08	0.19
70	12.66	0.73	6.53	0.31	0.43	0.18

Table 3.1: Standard deviation of RMS compensation error (deg.): $N_{sub} = 160$

SNR (dB)	$N_f = 16$, old	$N_f = 16$, Enh.#1+Enh.#2	$N_f = 32$, old	$N_f = 32$, Enh.#1+Enh.#2	Overlap	Reference
30	16.88	15.23	9.20	13.35	13.62	0.41
40	10.34	6.03	11.01	4.76	6.78	0.19
50	4.02	1.14	2.39	1.55	2.32	0.06
60	1.48	0.49	1.89	0.40	0.65	0.05
70	1.24	0.23	1.33	0.13	0.28	0.05

Table 3.2: Standard deviation of relative RMS delay spread error (%): $N_{sub} = 160$

SNR (dB)	$N_f = 16$, old	$N_f = 16$, Enh.#1+Enh.#2	$N_f = 32$, old	$N_f = 32$, Enh.#1+Enh.#2	Overlap	Reference
30	5.30	5.01	4.99	4.74	4.29	0.11
40	3.14	1.90	3.78	1.90	2.85	0.05
50	2.09	0.51	1.35	0.63	1.09	0.04
60	1.16	0.26	0.78	0.17	0.33	0.05
70	1.16	0.19	1.05	0.09	0.14	0.05

Table 3.3: Standard deviation of relative RMS mean excess delay error (%): $N_{sub} = 160$

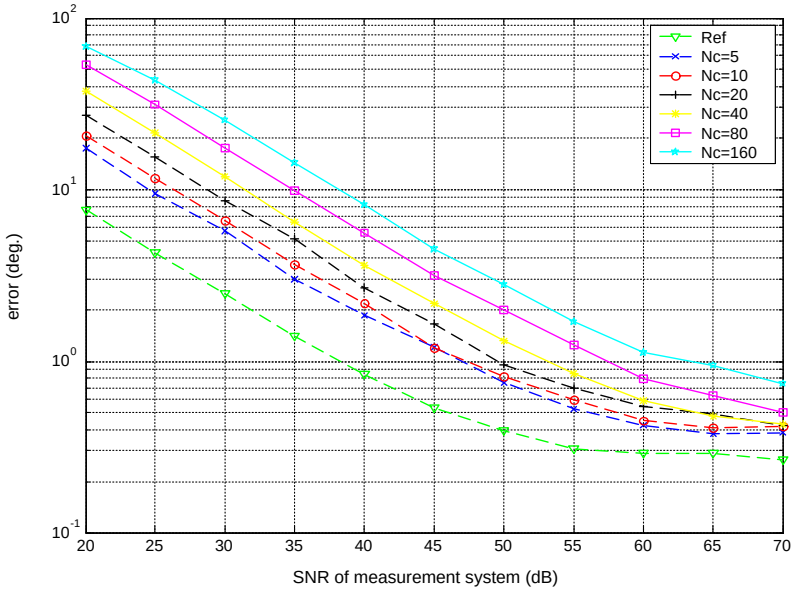

Figure 3.18: RMS compensation errors ($\zeta_{rms,EP}$) against the number of concatenations N_c and SNR of the measurement system.

offsets. The number of sub-carriers was $N_f = 16$ for all variations. The improved extrapolation method ("Enh.#1+Enh.#2") was used. Fig. 3.18 shows the RMS compensation errors vs. SNR values for varying number of concatenations. Corresponding to the expectation, performance degradation can be identified with increased number of concatenations. With increased SNR values, the lower bound of 0.27° is nearly approached for $N_c = \{5, 10, 20\}$. The standard deviation to Fig. 3.18 is summarized in Table. C.1. The error characteristics of other parameters are similar (see Fig. 3.19 and Fig. 3.20). Above 60 dB, an $e_{ds,rel,EP}$ as well as $e_{ed,rel,EP}$ lower than 0.1 % are attainable approaching towards lower bound, when $N_c = \{5, 10, 20\}$ are used.

G. Error Propagation

It was shown that through the consecutively performed compensation procedure, errors introduced by previous compensation can propagate with increased sub-channel number. Fig. 3.21 illustrates an example for an error distribution, which shows the number of appearances of the accumulated compensation errors over 500 simulation runs at SNR=50 dB at sub-channel # 90 and # 140, respectively (i.e. the relative distance to the middle reference sub-channel number of #80 is, respectively, 10 and 60), by means of histogram analysis. The errors at sub-channel # 90 are aggregated virtually around a single error while errors at sub-channel # 140 are widely distributed. The characteristics of the error propagation can be specified by observing the error statistics for each sub-channel. Using the data from 500 simulation runs, the average compensation errors and standard deviations to each sub-channel were calculated. The results are illustrated in Fig. 3.22. We notice quasi linear increasing compensation errors with different

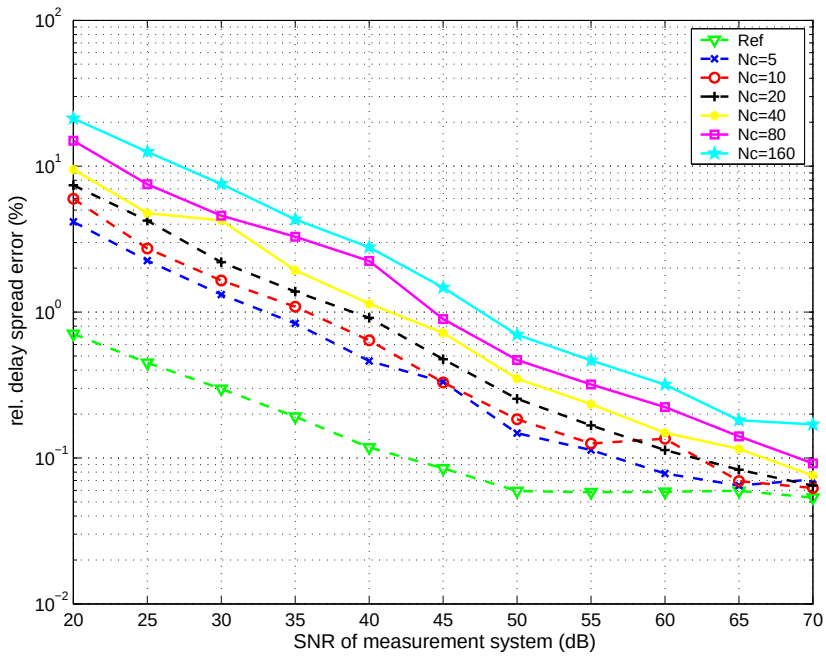

Figure 3.19: Relative RMS delay spread errors ($e_{ds,rel,EP}$) against the number of concatenations N_c and SNR of the measurement system.

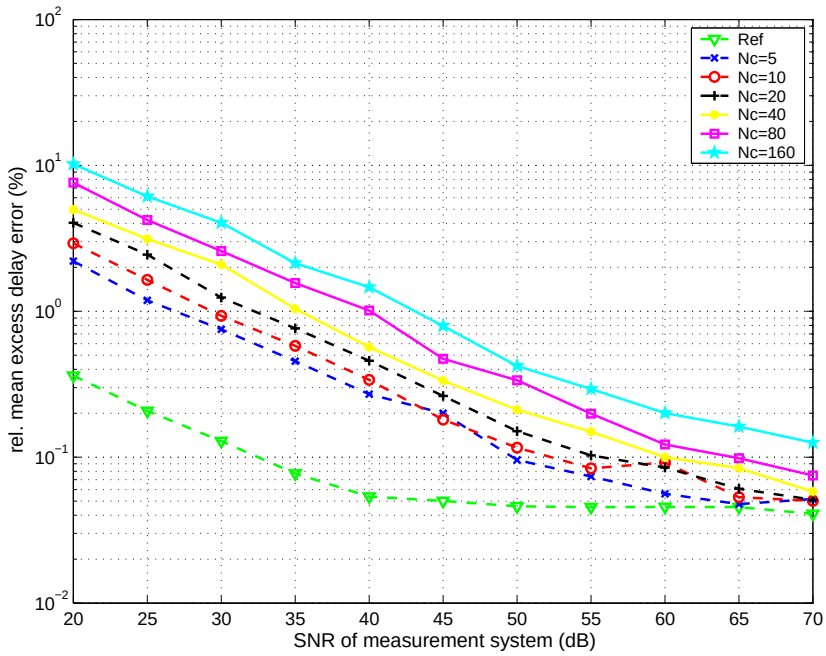

Figure 3.20: Relative RMS mean excess delay errors ($e_{ed,rel,EP}$) against the number of concatenations N_c and SNR of the measurement system.

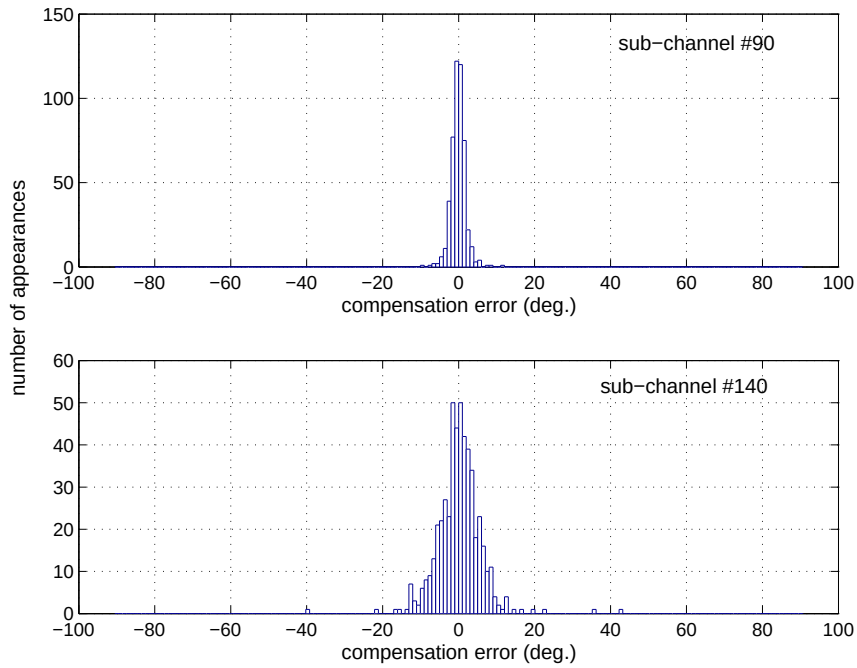

Figure 3.21: An exemplary histogram analysis of compensation errors at sub-channel $\#90$ and sub-channel $\#140$, respectively: errors collected over 500 simulation runs (SNR=50 dB).

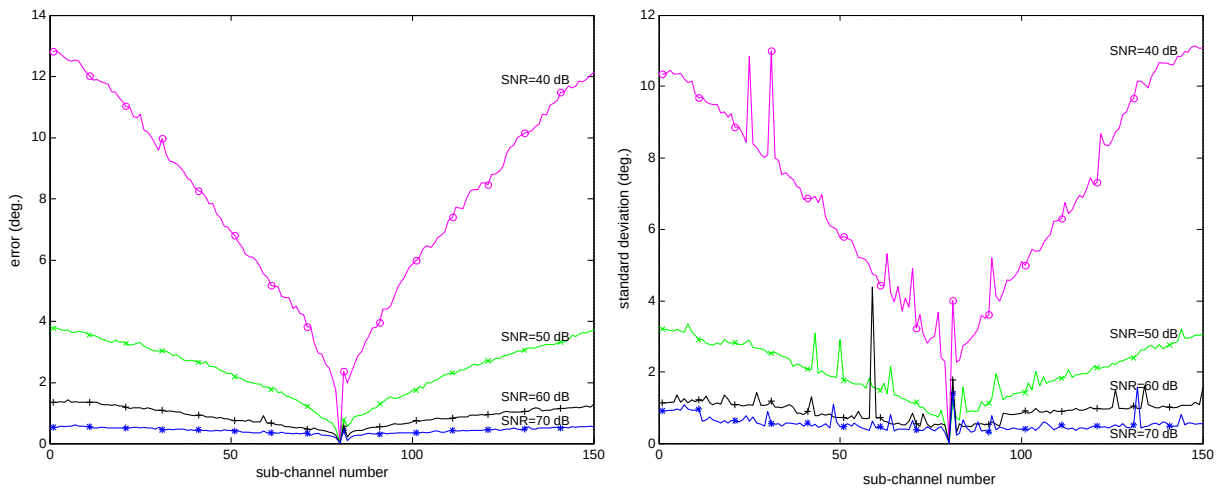

Figure 3.22: Average compensation error (left) and its standard deviation (right) vs. number of sub-channels using the extrapolation method with $N_f = 32$.

gradients depending on the SNR with rising number of sub-channels (i.e. concatenations). The error propagation is highly mitigated by increasing SNR by 10 dB (from 40 dB to 50 dB). A clear difference in the error characteristics is also observable between SNR=50 dB and even higher SNRs. The standard deviations follow widely the tendency above with few irregularities. The characteristic of the error propagation for the overlap method is much similar (see Fig. D.1).

3.4 Summary and Discussion

In this chapter, the problem of channel reconstruction is investigated when using a narrowband system and employing an antenna array for wideband channel measurement. More specifically, the channel concatenation methods were investigated to achieve wideband channel measurement, if the measured sub-channels are individually perturbed by random phase offsets due to lack of synchronization to common reference clock. In the preliminary consideration, the impact of phase offsets on the channel parameters was shown by means of a simulation study. The results showed that an average phase offset larger than 20° can degrade the channel parameters significantly. We dwelled on concatenation methods to reconstruct the channels by compensating phase offsets. A simple mathematical analysis was performed to express the compensation errors in context with error sources.

Extensive simulative error analysis has been conducted to specify the reliability of the methods. The performance of the extrapolation method could be largely improved by utilizing the proposed enhancements: the errors appearing at early state of the compensation procedure could be effectively prevented by exploiting redundant information from antenna array channels, where such breakdowns were detected and excluded (enhancement # 1). The optimal choice of reference sub-channel for the concatenation method allowed to reduce the number of compensations, which in turn led to the additional improvement in error statistics (enhancement # 2).

Hence, an average RMS compensation error less than 2.81° and a standard deviation of 1.96° could be achieved with the improved extrapolation method for SNR=50 dB (with $N_f = 16$ for concatenations of 160 sub-channels), while the overlap method provided corresponding error statistics as 4.58° and 4.35°, respectively. Moreover, relative errors smaller than 0.7 % and 0.6 % could be achieved using the same conditions as above for the channel parameters such as delay spread and mean excess delay, respectively. In rare cases, the errors appeared large, but due to the large number of trials, those errors would only have a minimal effect on the statistics. In performance assessment by variation of the number of concatenations, the performance lower bound could be well approached when a small number of concatenations ($Nc = \{5, 10, 20\}$) and a sufficiently high SNR were used. The error propagation is a systematic nature of the methods due to consecutively performed reconstruction taking reference by previously compensated sub-channels. The propagating errors provide a quasi linearly increasing characteristic as number of concatenations increased.

Chapter 4

Measurement System Setup

Characteristics of radio propagation channels can be obtained empirically by experimental investigations. Regarding the channel as a linear system, it can be characterized by the channel impulse response (CIR) in the time domain or channel frequency response (CFR) in the frequency domain. The parameters associated with CFR can be described by probability, which leads to the stochastic channel model. This chapter describes the measurement system setup, which is designed for the space-time channel measurement at 60 GHz. First of all, the digital array transceiver system is used that allows parallel baseband conversion of the received analog antenna array signals. Extension to the spatial domain is realized by using a 60 GHz 1×4 patch antenna array, which permits, combined with the digital array transceiver system, to obtain the space-time channel measurement simultaneously within a 6 MHz measurement bandwidth. The wideband channel measurement of 1 GHz RF-bandwidth is aimed applying the frequency sweep technique. The previously discussed channel concatenation method is employed as the post signal processing to compensate phase offsets of consecutively measured sub-channels.

In the following, the components and modules used for the measurement system setup are described in detail. The system calibration is depicted and the overall measurement setup is specified. Finally, the system is examined in terms of the reliability and it is demonstrated with measurement examples.

4.1 Measurement System Setup

4.1.1 Description of the modules

A. Digital Array Transceiver

The digital array transceiver consists of five electronic assembly groups developed by *Kortke*[1]. They are designed to down-convert eight IF signals at 200 MHz (only four of which are used for channel measurement in this work) parallel into baseband for reception mode (see Fig. 4.1 (a)). The receiver circuits of the digital array transceiver comprise of down-link mixers and IF-amplifiers which allow to set an amplification factor of about 80 dB for all array signals. Each A/D-converter generates digital signals with 10 bit resolution from in-phase/ quadrature (I/Q)

[1]The system was developed for research [59] as well as teaching at the Technical University of Berlin, Germany.

(a) (b)

Figure 4.1: (a) Digital array transceiver: eight IF inputs at 200 MHz, 10 bit resolution with the sampling frequency of 16 MHz, data transfer to PC over EPP interface, (b) Tx modulator with an external LO input and an IF output.

baseband signals. The sampling frequency is 16 MHz. The received baseband signals are stored in sampling memory, whose capacity is 256K samples corresponding to the time duration of 16.384 ms. Data transfer to PC is achieved over EPP interface, which allows a data transfer rate of about 500 kBytes/s. The baseband transmit signals are generated by the signal generator board located in the same housing as the digital array transceiver. For transmission mode, the sounding signals designed in a PC are transferred into the signal memory of the digital array transceiver over cable. The signal memory provides the storage capacity of 128K samples corresponding to the maximum transmit duration of 16.384 ms due to the transmit sampling rate of 8 M samples/s. The resolution of the D/A-converter is 10 bit.

B. RF-Frontend

The RF-Frontend consists of 60 GHz power amplifiers, mixers and a LO distribution network, which divides the supplied single 60 GHz carrier signal from the synthesizer (HP 8362B) into four carrier signals and distributes them to each input of 60 GHz mixers (see Fig. 4.2 (a)).

C. Transmit Antenna

For radio propagation channel measurement, an isotropic wideband antenna would be an ideal choice. However, such an antenna is hardly available, especially at 60 GHz. Instead, a 6 dB gain open-ended waveguide was used as the transmit antenna. The antenna pattern was obtained by measuring the received RF-power in an open area in the laboratory using a positioning system, moving the antenna between $[-60, 60]$ degrees in $5°$ steps in the azimuthal angles. The measured antenna pattern is shown in Fig. 4.3 (a).

D. Receiver Patch Antenna Array

The 60 GHz 1×4 patch antenna array (see. Fig. 4.2) developed by *Grosskopf et al.* [60] was used as the receiver antenna, which has been applied for experimental investigations on

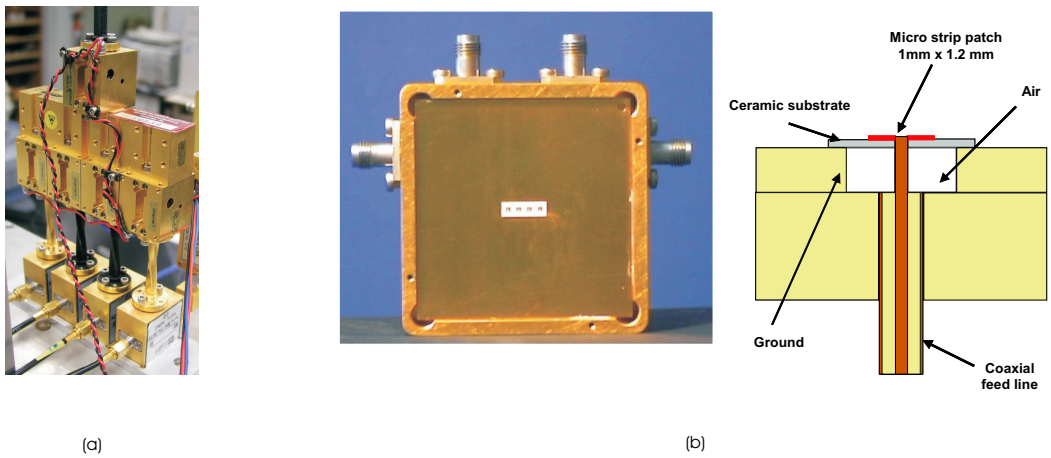

Figure 4.2: (a) RF-Frontend: power amplifiers, mixers and LO distribution network, (b) 1×4 patch array antenna with $0.5\ \lambda$ element spacing and its cross sectional view.

beamforming [61,62] and data transmission at 60 GHz [63,64]. The patch antennas are fabricated by applying classical photolithographic methods printed on a very thin (0.1 mm) aluminum oxide substrate. The λ /2 spaced antenna elements are fed from the rear side by semi-rigid coaxial lines. The patch size is $1 \times 1.2\ mm$. The measured radiation patterns of the antenna array elements are shown in Fig. 4.3 (b).

4.1.2 Channel Sounder Setup

The sampling timing offset is a severe problem, especially when the channel is measured successively, because the measured sub-channels would be suffered by different amount of linear phase shifting factors. Since these unknown factors are frequency dependent, the outermost frequency component is affected most. If a linear phase shift less than 5° is required for a measurement bandwidth of 6 MHz, the requiring sampling timing offset must be smaller than $2.3 \times 10^{-9}\ s$.

$$t_{off} < \frac{5^\circ}{360^\circ \cdot 6 \cdot 10^6\ Hz} \approx 2.3 \times 10^{-9}\ s \tag{4.1}$$

This still turns out to be a real challenge in the design. It is quite difficult to compensate this by applying an algorithm. Therefore, a modification on hardware side was performed: The Tx signal generator board was placed at receiver site and the sampling units of Tx and Rx were connected to a common sampling clock, so that the sampling timing offset is effectively reduced.

From this reason, the baseband sounding signals are generated at the Rx site and subsequently IF modulated. The IF modulated sounding signals are delivered to the Tx site over about 10 m cable, which presents no constraint to the channel measurement, because the maximum Tx-Rx separation in the measurement campaign would be less than this distance.

As sounding signals, single tone signals of 16 different frequencies were used. These sub-carriers provide a carrier spacing of 400 kHz within a 6 MHz frequency range (see Fig. 4.4). A sub-carrier comprise of 730 digital samples at the Tx site which were doubled at the Rx site due

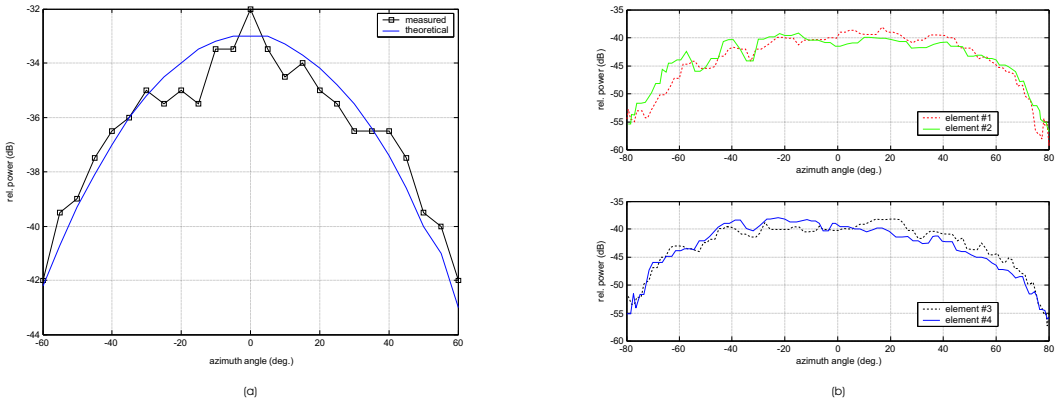

Figure 4.3: Radiation pattern of Tx and Rx antennas: (a) open-ended waveguide, (b) 60 GHz 1×4 patch array antenna.

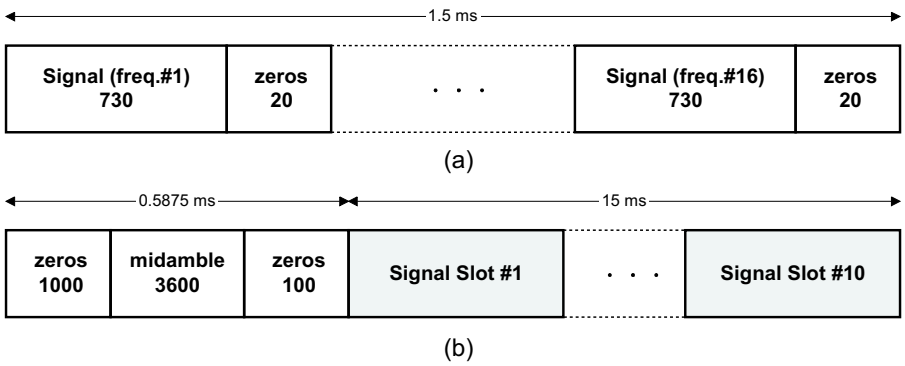

Figure 4.4: Transmit signal frame structure. (a) Signal slot: 16 single tone signals with a total transmit duration of 1.5 ms, sub-carrier spacing is 400 kHz. (b) Signal Frame: midamble signal for frame synchronization, a maximum of 9 redundant signal slots can be added.

to its double sampling frequency. A single signal slot contains the 16 sub-carrier signals and has a transmit time duration of 1.5 ms. A transmit signal frame can be composed of this one signal slot and additionally added nine redundant signal slots, which were used for averaging the measured signals coherently to increase the SNR. To assist finding the start of the sounding signals, a chosen midamble signal was prefixed. Frequency stability is also an important issue, since phase noise limits the dynamic range. The synthesizers used apart from the oscillator of the digital array transceiver were connected to a 10 MHz reference signal from SMIQ (see Fig. 4.5), which itself served as the carrier signal generator for the IF modulation of the baseband sounding signal.

The overall setup is depicted in Fig. 4.5. The transmitter part of the system consists of a sounding signal generator, an I/Q modulator, a 60 GHz mixer, a synthesizer, a bandpass filter and a power amplifier. The I/Q baseband signal from the Tx signal generator is IF modulated at 1.8 GHz with the synthesizer signal from SMIQ (*Rhode & Schwartz*). The IF modulated sounding signal is delivered to the 60 GHz mixer over 10 m cable. With the synthesizer signal

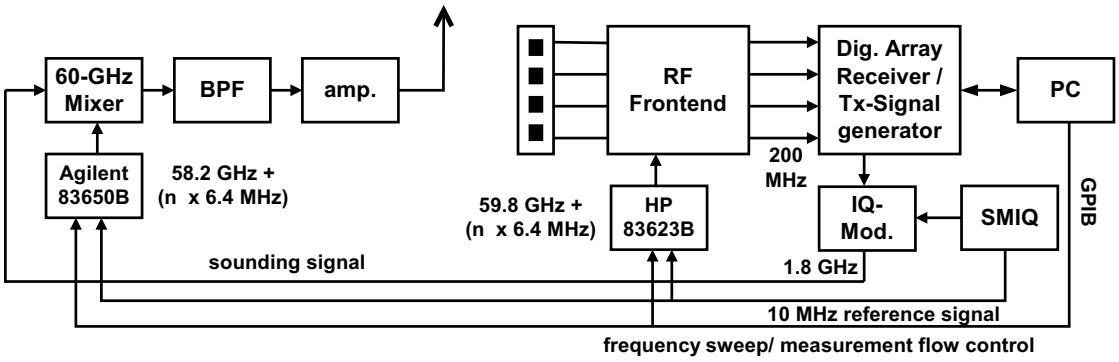

Figure 4.5: The channel sounder setup. Tx: 0.8-2.5 GHz IQ-modulator, IF-synthesizer SMIQ at 1.8 GHz, 60 GHz Tx synthesizer (Agilent 83650B), 60 GHz bandpass filter and 60 GHz amplifier, Rx: 1x4 digital array transceiver (IF at 200 MHz), LO distribution network, 1×4 patch array antenna, power amplifiers, mixers and 60 GHz Rx synthesizer (HP 83623B).

from the Agilent 83650B, the 60 GHz RF signal is produced. The RF signal is then bandpass filtered, amplified and fed into the transmit antenna of the open-ended waveguide radiating the power of about 10 dBm (10 mW). The receiver part is comprised of a 60 GHz 1×4 patch antenna array, a synthesizer, a LO distribution network, preamplifiers, mixers and the digital array transceiver system. At the receiver antenna, the RF signals from the antenna array outputs are initially amplified and then fed to the mixers, where the down-conversion to 200 MHz is performed. The digital array receiver converts these analog array signals into digital samples stored into the sampling memory. The digital samples are transferred to PC for further analysis. The CFRs are determined by correlating the received signals with a locally saved copy of the sounding signals. A PC controls the timely correct recording of channel data when swept over the measurement center frequencies (stepping of the measurement center frequencies), by using an implemented flow control realized through handshaking between PC and both Tx and Rx synthesizers over GPIB interface. Dependent on distance and RF power, SNRs of the measurement system between 45 dB and 50 dB could be achieved with averaging of redundant signal blocks. The wideband channel measurement was performed by consecutively measurement of $N_{sub} = 178$ sub-channels with stepping of the measurement RF center frequencies. In the post signal processing, the CFRs of sub-channels have been undertaken by a calibration, then the resulting CFRs were concatenated by applying the improved extrapolation method with middle reference as described in chapter 3.

4.1.3 System Calibration

The calibration measurement for the antenna array has been carried out in an empty room using the calibration chamber (see Fig. 4.7). Keeping the antenna array fixed, the measurement was performed using a 20 dB TE10 mode horn antenna moving the Tx in the H-plane of the field in a 15° equidistant grid between ± 90° along the broadside directions. The distance between Tx and

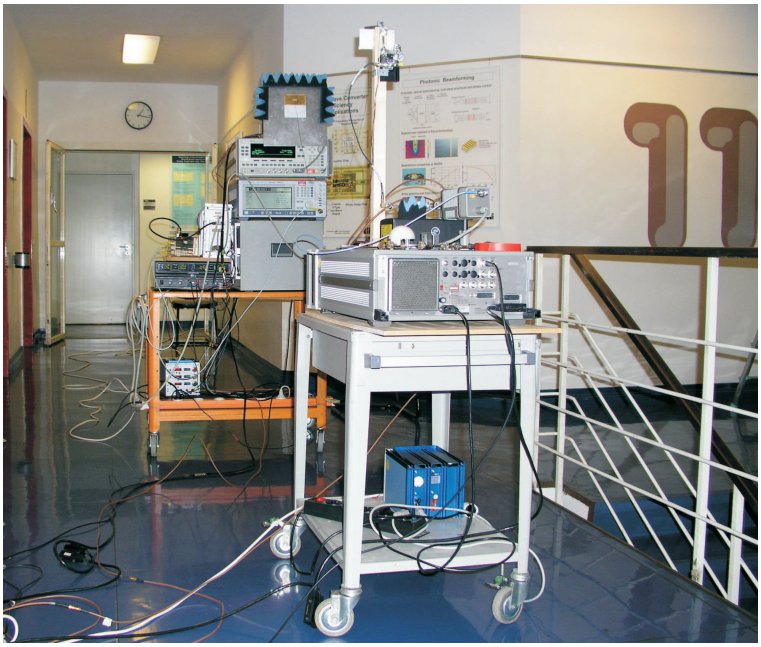

Figure 4.6: The designed 60 GHz space-time channel sounder.

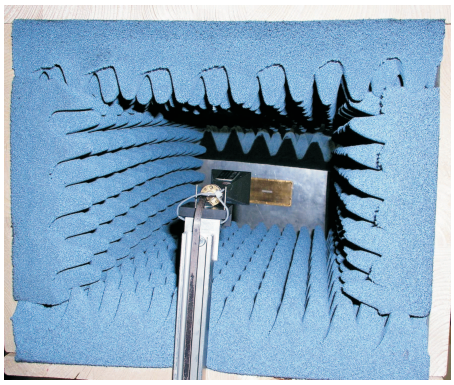

Figure 4.7: The chamber for the antenna array calibration.

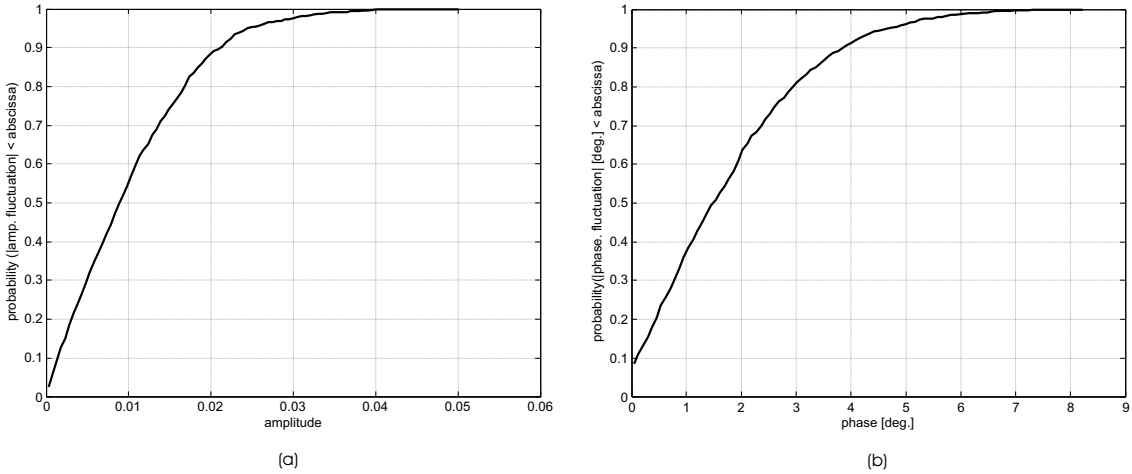

Figure 4.8: Results of the measurement system calibration: (a) CDF of the amplitude fluctuations, (b) CDF of the phase fluctuations.

Rx antennas was approximately 150 λ. Based on the set of the measurements the calibration matrix was calculated according to the method proposed in [65]. The calculated calibration matrix was applied to the recorded channel data for correction of amplitude as well as phase mismatching and mutual coupling effects.

The nonlinearity of the measurement system was eliminated by back-to-back measurement. Fig. 4.8 shows the CDF of the amplitude as well as the phase fluctuations of the calibrated system itself. The calibrated system provides a maximum amplitude fluctuation of $\pm$ 0.05 over the mean value and a maximum phase variation of about 8°. The small fluctuations of amplitude and phase can be attributed to the amplitude and phase noise of the system components.

4.2 Examination of the Measurement System

The measurement system has been examined by means of reference measurement, whereby the reliability of the employed concatenation method in the context of the multi-dimensional channel parameter estimation was assessed. In the defined scenario as depicted in Fig. 4.9, a reflector was mounted at a predetermined position. In this scenario, two incident waves are expected: a direct and a reflected wave. The measurements were conducted in an empty room and the environment was sufficiently isolated with absorber materials. The reflector used was a metal sheet (26 x 42 x 1.5 cm) and mounted at the same height as the Tx and Rx antennas. The reflection point is assumed to be located in the middle of the metal sheet. The measurements were repeated 4 times. The SAGE algorithm was applied for the 2-D channel parameter estimation. The quantization steps for propagation delay and AOA in SAGE were set to 1 ns and 0.05°, respectively. In all measurements, the expected direct and reflected waves could be clearly observed. The AOA estimates for the reflected wave exhibited a small deviation less than 1° against the reference value of 27°, providing an attenuated power of 13 dB compared to the

direct wave and representing the expected relative propagation delay of 1 ns. The observed additional reflected waves at around 0° probably were a result of the rectangular shape of the room as shown in [66].

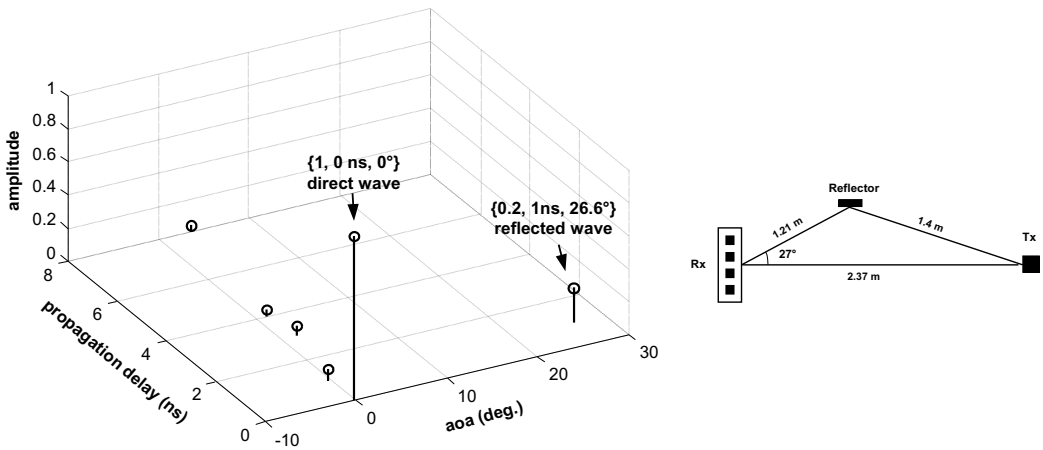

Figure 4.9: Reference measurements: expected incident waves (a direct and a reflected wave) at 0° and 27°, respectively, estimated parameters $\theta_\ell = \{\alpha_\ell, \tau_\ell, \phi_\ell\}$: $\theta_1 = \{1, 0\ ns, 0°\}$, $\theta_2 = \{0.2, 1\ ns, 26.6°\}$

Below, we carry on our discussion with some other examples. Fig. 4.10 shows an example of the CFR (solid line) obtained from measurement conducted in a narrow gangway (width 1.3 m, Tx-Rx separation: 3.5 m). Another curve (dashed line) in Fig. 4.10 represents the CFR reconstructed based on SAGE estimates. Furthermore, the power azimuth profiles were calculated to both CFRs by applying a conventional beamforming technique and the results are depicted in Fig. 4.11. By comparing the results, the reliability of SAGE algorithm could be examined indirectly. Except some small errors, we can identify an overall good match between the two CFRs. The power azimuth profiles (PAP) in Fig. 4.11 also exhibit good agreement and coincide between −30° and 60°. It should also generally be noted that some possible discrepancy might remain hidden due to limited azimuth resolution. Another example of a measurement performed in the laboratory room is shown in Fig. 4.12. The Tx in this example was partly shadowed by the instrument tower. The reconstructed CFR follows the measured CFR well. The associated measured PAP shown in Fig. 4.13 accords well with the reconstructed PAP. Moreover, this example indicates a tendency of the multipath components to exhibit a partitioning phenomenon, where two partitions are identifiable. The presented examples correlate plausibly with the measurement environment.

4.3 Summary and Discussion

The measurement setup of the 60 GHz space-time channel sounder has been presented. The measurement system was designed using a digital array transceiver and a 60 GHz 1 × 4 patch antenna array [67]. The digital array transceiver allowed parallel baseband conversions. Hence,

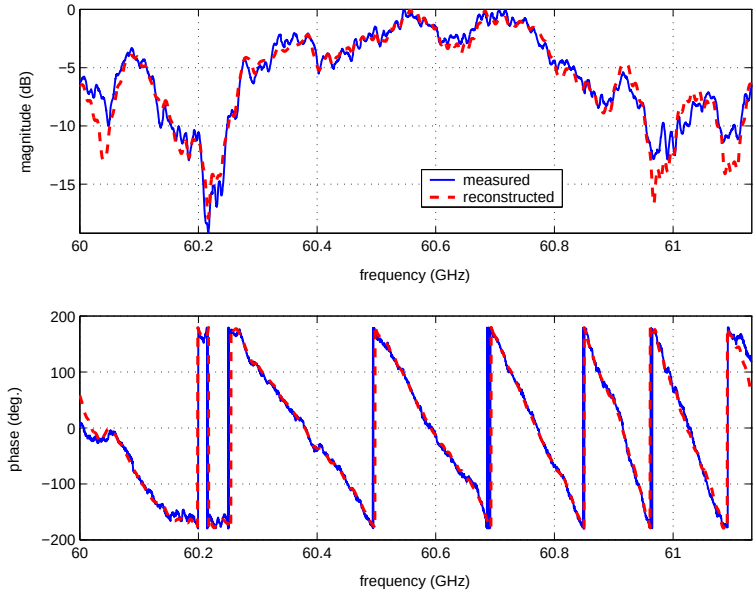

Figure 4.10: A measurement example for a gangway (corridor I, Tx-Rx separation: 3.5 m): measured (solid line) and reconstructed (dashed line) CFRs (reconstructed CFR based on SAGE estimates).

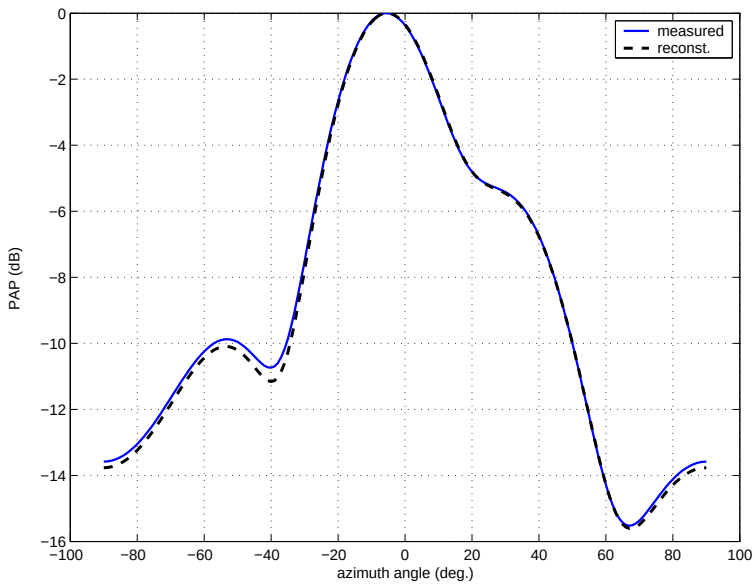

Figure 4.11: Measured (solid line) and reconstructed (dashed line) PAPs associated with Fig. 4.10

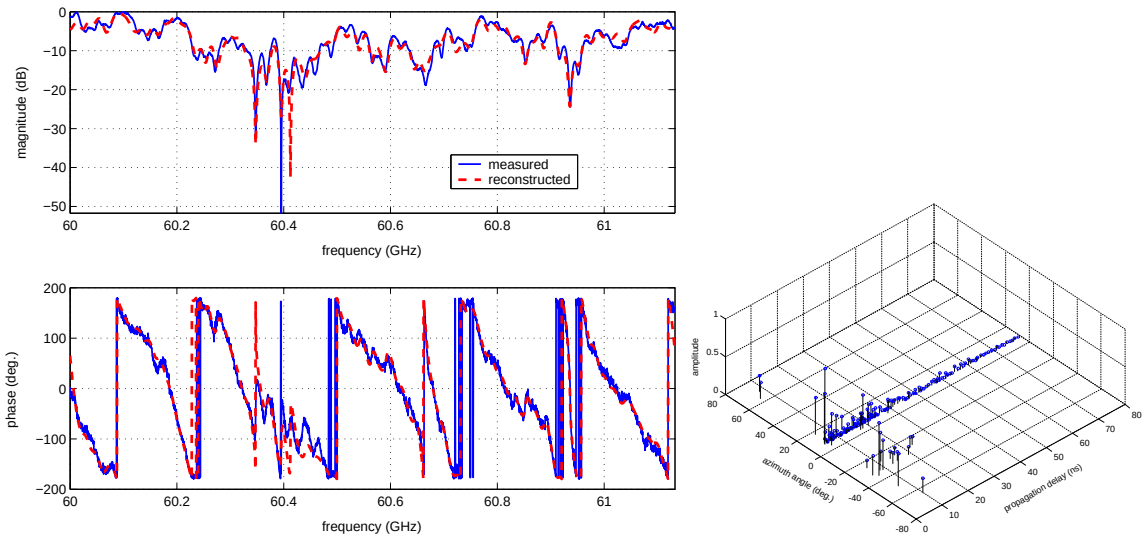

Figure 4.12: A measurement example for a room (Tx-Rx separation: 3.3 m): measured (left, solid line) and reconstructed (left, dashed line) CFRs (reconstructed CFR based on SAGE estimates)

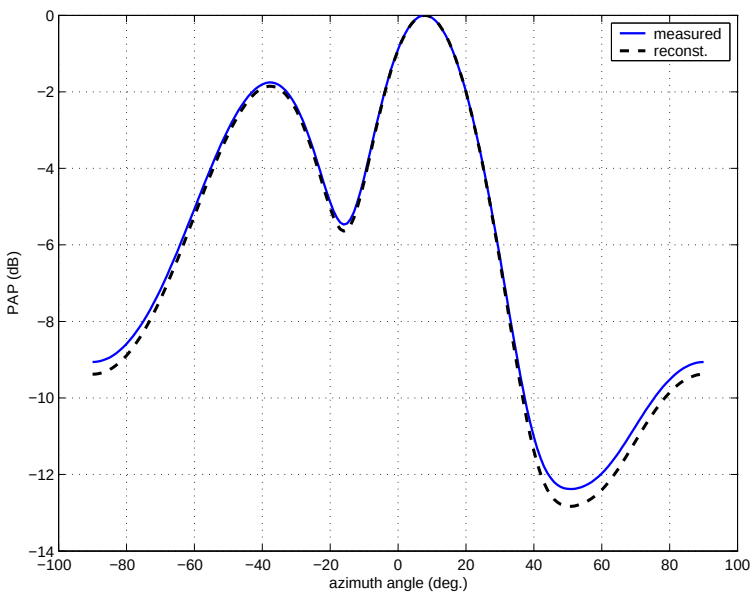

Figure 4.13: Measured (solid line) and reconstructed (dashed line) PAPs relating to Fig. 4.12

the digital array transceiver in conjunction with the 60 GHz antenna array facilitated the design of the space-time channel measurement system. In the measurement setup, the Tx and Rx sampling modules were connected to 16 MHz common clock to minimize the sampling timing offset. The 60 GHz synthesizers used were connected to a 10 MHz reference signal to increase frequency stability. The local oscillator used for the digital array transceiver could not be synchronized, though. As sounding signals, single tone signals of 16 different frequencies were used. The sub-carriers of a transmit sounding signal slot were arranged equally distanced in the frequency domain with 400 kHz carrier spacing within 6 MHz measurement bandwidth. Due to the narrow bandwidth of the data acquisition components used, the aimed wideband measurement was achieved by applying the frequency sweep technique. To represent the correct CFR function, the consecutively measured sub-channels have been reconstructed by applying the considered extrapolation method described in the previous chapter. The reliability of the designed channel sounding system was examined by means of reference measurements. An example of the reference measurement was given, by which the resolution capability of the measurement system was demonstrated. Furthermore, the reliability of the designed system in the context of SAGE estimation was verified and the results were discussed with some examples. It was identified that the measured CFRs and PAPs correlated well with those reconstructed based on SAGE estimates. It should be noted that the system is suitable only for strictly stationary channel measurement due to limited measurement speed.

Chapter 5

Statistical Characteristics of Indoor Radio Channel at 60 GHz

This chapter presents the results of the statistical analysis of the indoor propagation channel obtained by conducted measurement campaign in the corridors of an office building at 60 GHz. The measurement campaign has been carried out using the described space-time channel sounder in the previous chapter. Hence, multipath components were resolved in the temporal domain with a time resolution of about 1 ns and in the spatial domain using an 1×4 antenna array. The space-time channel parameters were extracted from the collected measurement data by applying SAGE algorithm. The estimated parameter sets were statistically analyzed for the stochastic space-time channel modeling. The chapter is organized as follows. In the first section, the measurement environment and the measurement campaign are described. In the following section, the results from the statistical analysis with respect to TOA parameters are presented followed by AOA statistics in the next section. Then, the power spectra of TOA and AOA are discussed and the statistical channel models for the TOA and AOA are proposed. Finally, the results are summarized and conclusions are drawn.

5.1 Site Description and Measurement Campaign

The measurement campaign has been conducted at a carrier frequency of 60 GHz in three differently sized corridors in an office building whose construction plan is shown in Fig. 5.1. The height of the ceiling was about 2.57 m above the floor. Unlike corridors I and III, corridor II (see Fig. E.1- E.3) has windows along the entire right side. Corridor I has a narrow gangway (width 1.3 m), while the corridor III is wider and has a "T" shaped open area in the middle. All corridors have concrete walls, doors and large poster frames. The height of both Tx and Rx antennas was set to 1.65 m. Throughout the measurements, the Rx was fixed while the Tx was moved over a regularly spaced grid between 2 m and 8 m. Since the Tx and Rx antennas were aligned during the measurement campaign, the LOS path was always present. During the measurements, the environment was empty apart from the experimental apparatus, which was conducted at night. A Total of 54 channel profiles was collected.

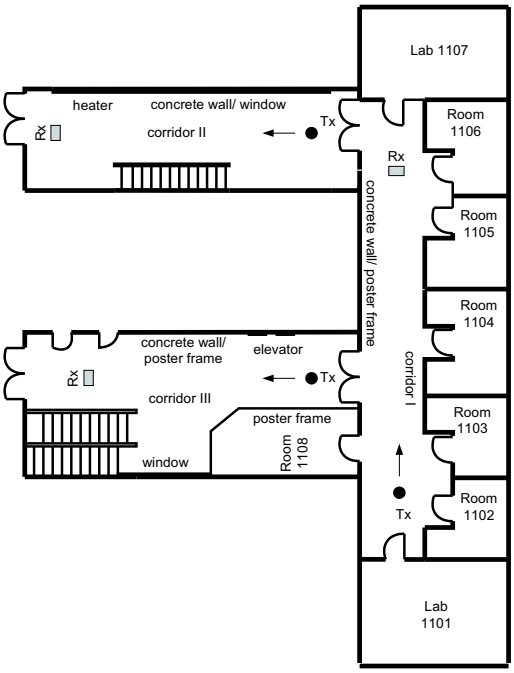

Figure 5.1: Site Description: corridor I: $1.3 \times 13.07 \times 2.57\ m$, corridor II: $3.07 \times 12.25 \times 2.57\ m$, corridor III: $5.5 \times 12.25 \times 2.57\ m$.

5.2 General Observation

When using a linear antenna array system, multipath components can be separated either by their AOA or TOA. A power delay profile (PDP) describes the temporal power distribution with respect to multipath TOA, while the power distribution in space domain is characterized by a power azimuth profile (PAP). In order to gain more insight into the multipath structure, we discuss its common characteristics based on some measurement examples. A brief environment description, where the measurement has been conducted, is illustrated in Fig. 5.2. In the laboratory room, three locations are shown exemplary, where the LOS path was present and its azimuth angle was determined manually. Moreover, the measurements were conducted for the same conditions using both an open-ended waveguide and a 20 dB TE10 horn antenna as the Tx antenna, so that the results could be compared directly. From the measured CFRs, 2-D parameter estimation was performed using the SAGE algorithm. Based on the estimates, the CFRs were reconstructed for comparison with the measured CFRs, whereby the estimation reliability could be assessed. Also, the PAPs for the reconstructed CFRs were calculated by using a classical beamforming technique with enhanced beamwidth (using a steering vector $\mathbf{a}(\phi_i) \in \mathbb{C}^{32\times 1}$, i.e. multipath powers arrived within the azimuth interval $\Delta\phi_{BW}$ were integrated, where $\Delta\phi_{BW} \approx 3.2°$).

At location 1 (Fig 5.3), the LOS path can be observed clearly for both antenna types used. For the open-ended waveguide, the contribution by the reflected waves can be seen at azimuthal

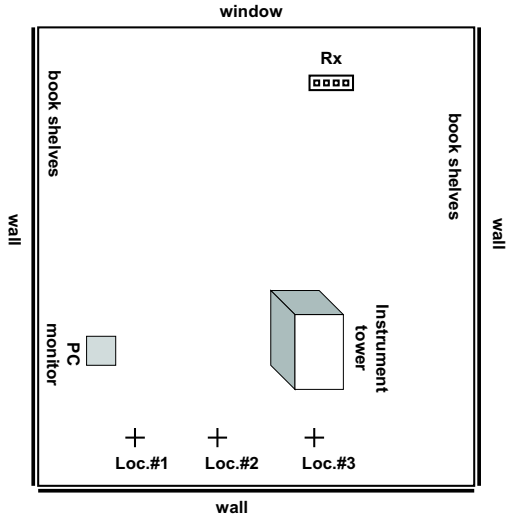

Figure 5.2: Layout of the laboratory.

angles between 20° and 40° attenuated by 8.8 dB relative to the LOS path, which originated from the instrument tower.

At location 2 (Fig 5.4), the LOS path is more dominant, since the LOS path and the reflected wave are assumed to be almost coherent in the azimuthal angles.

At location 3 (Fig 5.5), where the Tx antenna was partly shadowed by the instrument tower, but the LOS path was still present, strong multipath power mainly from $-40°$ and 25° for the open-ended waveguide can be observed. For the 20 dB horn antenna, beside the LOS path, multipath components around 0° can be observed, where the diffusive characteristic of multipath components could be assumed.

In Fig.F.4 and Fig F.6 (appendix F), the reconstructed PAPs measured in corridor III are presented. For Fig. F.4, the Tx antenna was located at 5.5 m from the Rx antenna and the left side was an open area (location at "T" shaped area in corridor III). A significantly reflected wave from the poster frame could be identified. With increased Tx-Rx separation (Fig. F.6, Tx-Rx separation: 7.5 m), the multipath powers impinging from both sidewalls can be observed. From the above observations, the following conclusions can be made:

- When the LOS path exists, the main multipath component is always arriving from the LOS direction.
- The LOS and multipath components of first through second azimuth directions contribute the majority of total azimuth power.
- The first order reflected waves arrive with relatively high power attenuation.
- The correlation with the propagation environments could be well observed. Consequently, the use of an image based method such as ray tracing technique appears to be a suitable tool for channel modeling for 60 GHz environment.

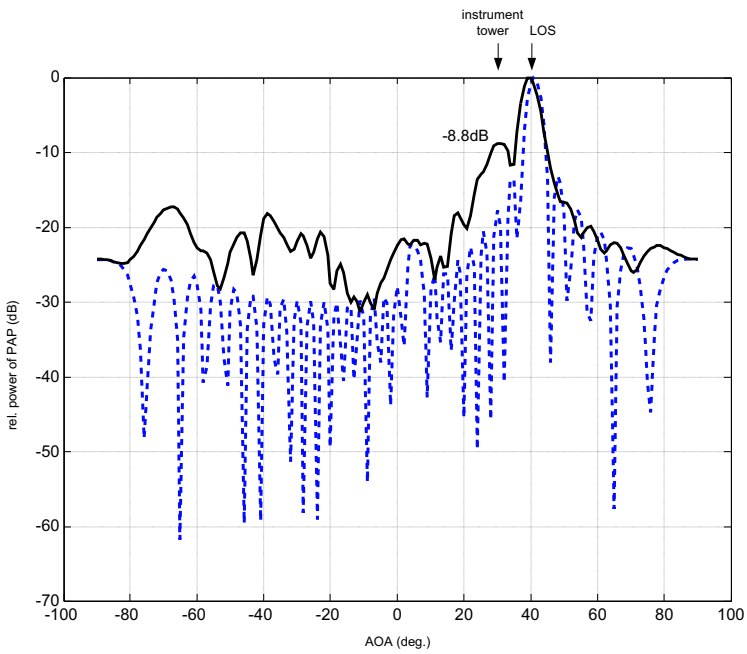

Figure 5.3: Location 1 in laboratory: PAP obtained using an open-ended wave guide (solid line) and a 20 dB TE10 horn antenna (dashed line).

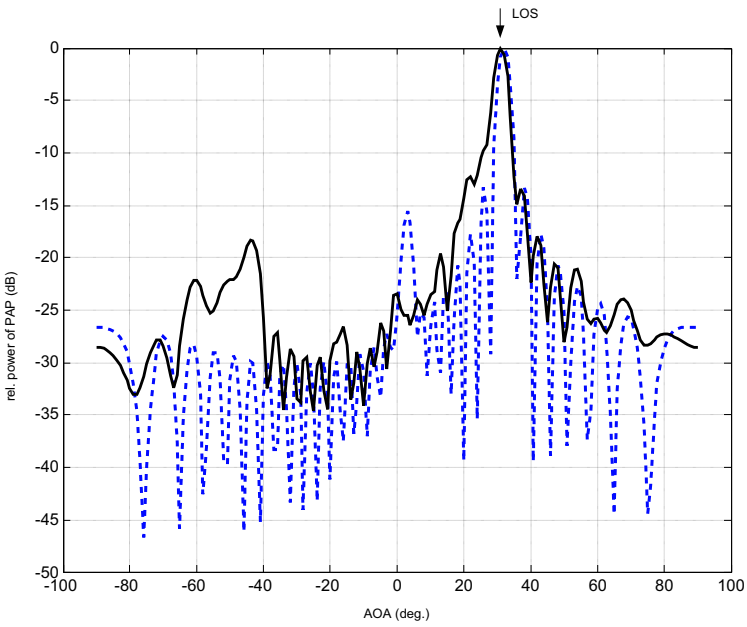

Figure 5.4: Location 2 in laboratory: PAP obtained using an open-ended wave guide (solid line) and a 20 dB TE10 horn antenna (dashed line).

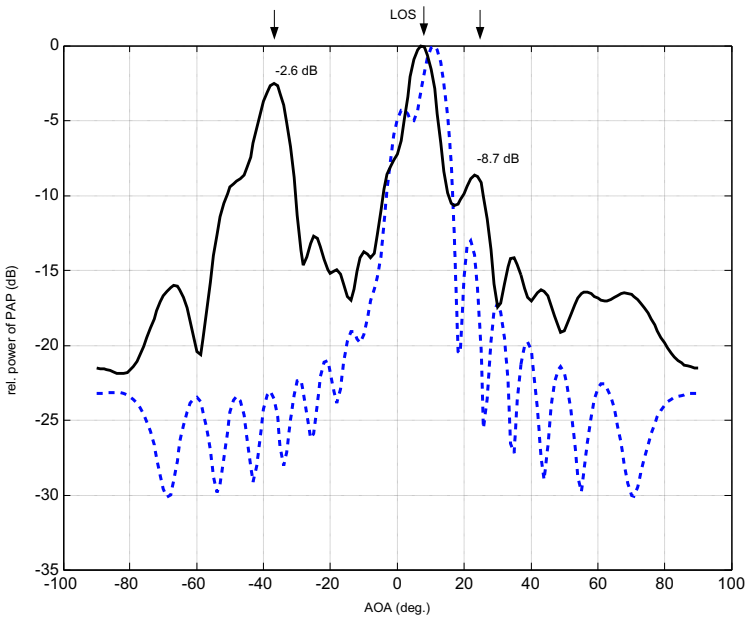

Figure 5.5: Location 3 in laboratory: PAP obtained using an open-ended wave guide (solid line) and a 20 dB TE10 horn antenna (dashed line).

5.3 Statistics of Channel Parameters

5.3.1 Time of Arrival Statistics

In this section, the statistics of the TOA parameters are presented. As the TOA parameters, the RMS delay spread, the mean excess delay, the coherence bandwidth and the Ricean K-factor were extracted from the measured channel profiles. These parameters give valuable information about the time dispersion of a multipath channel. For instance, the RMS delay spread is useful for determining the maximum transmission data rate of a system without equalization, while the mean excess delay can be used to determine the search interval of rake receivers. The coherence bandwidth is also an important measure, since it indicates the frequency selectivity of a multipath channel in terms of transmit bandwidth.

The empirical cumulative distribution function (CDF) of the RMS delay spread is depicted in Fig. 5.6. The RMS delay spread is in the range from 0.2 ns to 13.06 ns. The average RMS delay spread is 2.93 ns with the standard deviation of 2.81 ns. The RMS delay spread value at 60 GHz was reported in literature up to 60 ns for long corridors (up to 40 m) and for a large room (90 m^2) [34]. Our measurement results are well in accordance with the results in [20]. However, it is generally difficult to compare the results directly, because the setup of measurement system and measurement environment are generally dissimilar from each other.

Fig. 5.7 shows the empirical CDF of the mean excess delay. The values of $\bar{\tau}$ are between 1.04 ns and 19.16 ns. The average $\bar{\tau}$ is 5.76 ns and the standard deviation is 5.73 ns.

Fig. 5.8 shows the empirical CDFs of the coherence bandwidth for the threshold definitions

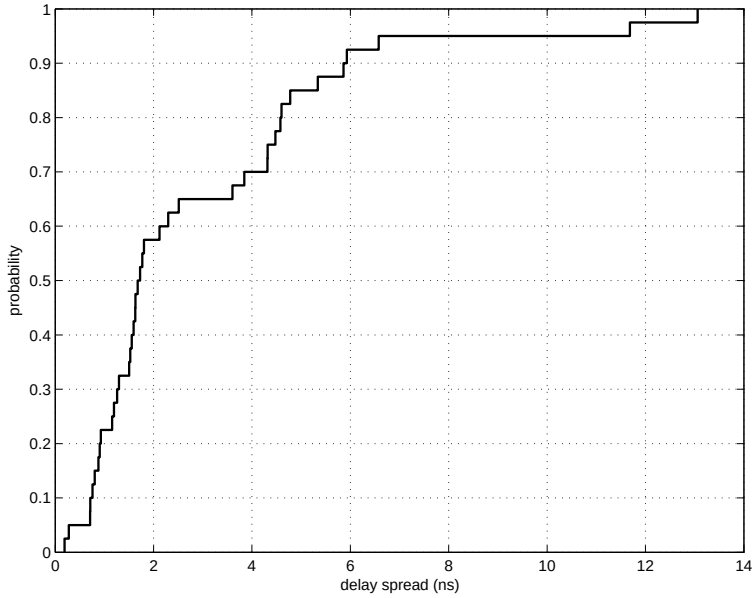

Figure 5.6: The CDF of the RMS delay spread (σ_τ).

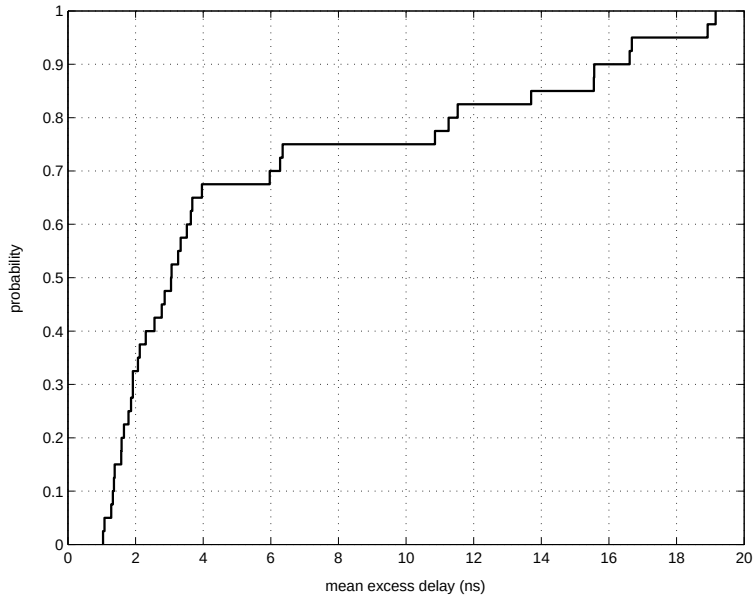

Figure 5.7: The CDF of the RMS mean excess delay ($\bar{\tau}$).

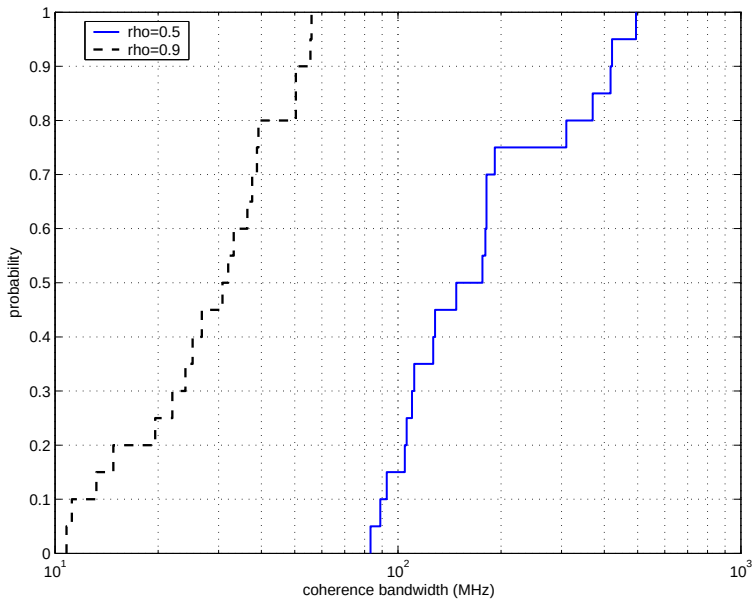

Figure 5.8: The CDFs of the coherence bandwidth (B_ρ): $B_{0.5}$ (solid line), $B_{0.9}$ (dashed line).

$\rho = 0.5$ and $\rho = 0.9$, respectively. A large deviation between the results from the two threshold definitions was observed. When using $\rho = 0.5$, the average coherence bandwidth is 201.2 MHz, while the average coherence bandwidth is 31.4 MHz for $\rho = 0.9$. The maximum and minimum values of $B_{0.9}$ are 10.8 MHz and 56 MHz, respectively. The standard deviation value is 14.28 MHz. The B_ρ is inversely proportional to the σ_τ. The product between $B_{0.9}$ and σ_τ is relatively constant and yields $\sigma_\tau \cdot B_{0.9} \approx 0.053$. In [34], an average coherence bandwidth value of 14.1 MHz was reported from measurements in corridors at 60 GHz ($41 \times 1.91 \times 2.68\ m,\ B_{0.9}$).

The Ricean K-factor was estimated using the method described in [68]. The method exploits the relationship given by

$$\frac{E[A]}{\sqrt{E[A^2]}} = \sqrt{\frac{\pi}{4(K+1)}} \exp(-0.5K)[(K+1)I_0(0.5K) + KI_1(0.5K)], \tag{5.1}$$

where $E[A]$ is the average amplitude, $E[A^2]$ is the average power of the CFR and I_x denotes the modified Bessel function of the first kind and x th order. Thus, the K-factor can be extracted from the theoretical curve. The advantage of this method is that it gives an estimate using only the power measurements. The empirical CDF of the Ricean K-factor is shown in Fig. 5.9. The K-factors are in the range between -3.98 dB and 12.06 dB with an average value of 5.93 dB. The standard deviation is 5.8 dB. In rare cases, the K-factor is smaller than 0 dB, where the windows appear to be strong reflectors (corridor II, Tx-Rx separation: 8 m).

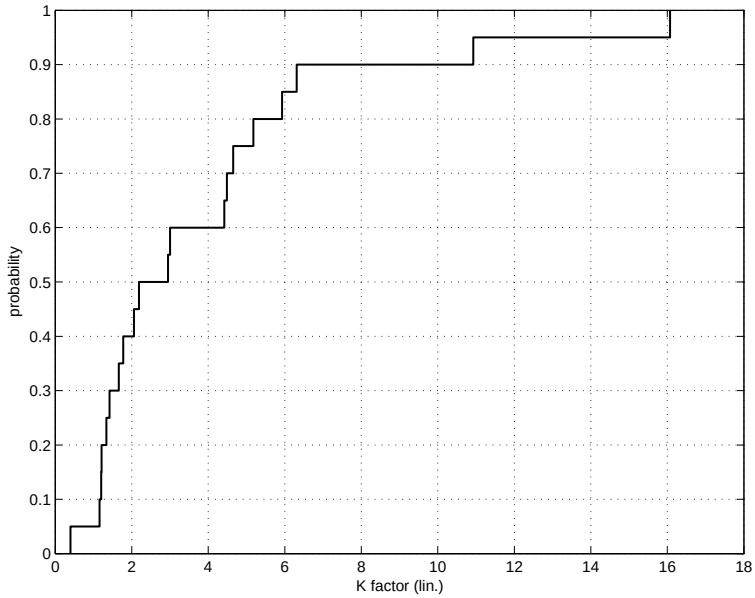

Figure 5.9: The CDF of the Ricean K factor.

	σ_τ (ns)	$\overline{\tau}$ (ns)	K-factor (dB)	$B_{0.9}$ (MHz)	σ_ϕ (deg.)
min	0.19	1.04	-3.98	10.8	5.36
max	13.06	19.16	12.06	56.0	40.7
mean	2.93	5.76	5.93	31.4	18.25
std.	2.81	5.73	5.80	14.28	9.59

Table 5.1: Summary of the TOA and AOA statistics.

5.3.2 Angle of Arrival Statistics

The RMS azimuth spread (σ_ϕ) is a measure of the angular dispersiveness of channel [1]. It was reported that the azimuth spread is dependent on the antenna height [1,69]. Moreover, the azimuth spread increases with lowered antenna height and the nature of scattering environments also has an impact on the azimuth spread [1].

The empirical CDF of the computed azimuth spread is shown in Fig. 5.10. The minimum and maximum σ_ϕ are 5.36° and 40.7°, respectively. The average σ_ϕ is 18.25° and the standard deviation is 9.59°. The 90 % of σ_ϕ remains lower than 27.75°. These values are large compared to measurement results from the outdoor environment, where the typical values were found to be between 5° and 15°, [69]. However, it was found that they are comparably similar to the results from indoor measurements in [6] and [7]. The statistics for TOA and AOA are summarized in Table. 5.1.

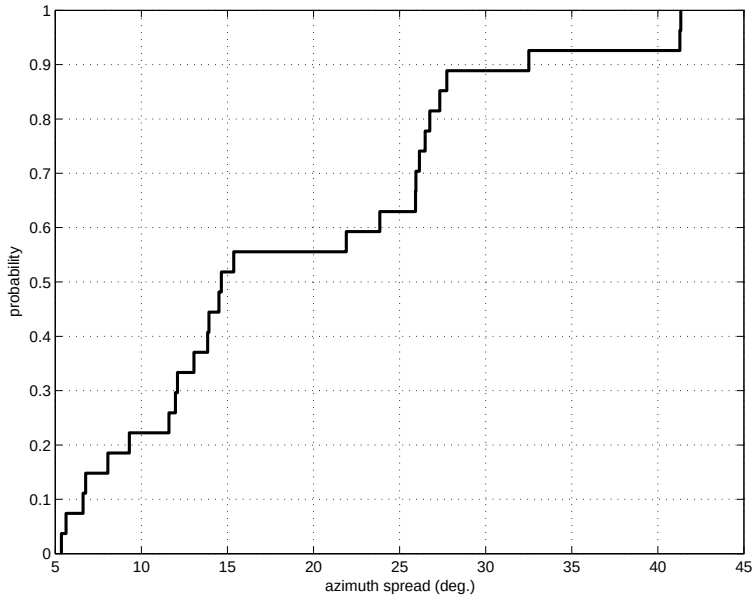

Figure 5.10: The CDF of the azimuth spread (σ_ϕ).

5.4 Statistical Space-Time Channel Models

The future 60 GHz systems may rely consolidated on the antenna diversity techniques due to the limited available power as well as the high attenuation. In few publications, the space-time channel models for the indoor environment were addressed both by experimental [6–8] and analytically. In [70] and [71], an analytical approach was taken using a circular and elliptical scattering model. However, the proposed models are primarily suitable for indoor environments at lower frequencies and the model assumptions are not validated. Research activities at 60 GHz including the receiver antenna pattern with AOA can be found in earlier literature [31] and [26]. In [26], the polarization effect was investigated addressing that multipath components can be effectively suppressed by employing circular polarization instead of linear polarization. More recently, the AOA parameters were statistically analyzed by measurement and the multipath structure was discussed [22]. Though these results help to gain more insight into the propagation mechanism, the models for the space-time channel at 60 GHz have not been addressed. In this section, the statistically analyzed empirical space-time channel models are presented and discussed.

5.4.1 Power Azimuth-Delay Spectrum

From the space-time channel impulse response $h(\phi, \tau)$ [5] given by

$$h(\phi, \tau) = \sum_{l=1}^{L} \alpha_l \delta(\phi - \phi_l, \tau - \tau_l), \tag{5.2}$$

the instantaneous power azimuth-delay spectrum can be defined to be

$$P_i(\phi, \tau) = \sum_{l=1}^{L} |\alpha_l|^2 \delta(\phi - \phi_l, \tau - \tau_l). \tag{5.3}$$

According to (5.3), the power azimuth-delay spectrum is defined as

$$P_{ad}(\phi, \tau) = E\{P_i(\phi, \tau)\}. \tag{5.4}$$

Assuming that the mechanisms associated with the delay dispersion and the azimuth dispersion are independent, the power delay-azimuth spectrum in (5.4) can be decomposed [5], [6] by

$$P_{ad}(\tau, \phi) \propto P_a(\phi) P_d(\tau), \tag{5.5}$$

where $P_a(\phi)$ and $P_d(\tau)$ denote the power azimuth spectrum (PAS) and the power delay spectrum (PDS), respectively, which can be determined by measurements. This assumption can be boosted by inspecting the correlation coefficient between σ_τ and σ_ϕ , since these are the second central moments of PDS and PAS. The correlation coefficient ρ is computed according to

$$\rho = \frac{\sum_{n=1}^{N} (\sigma_\phi(n) - \overline{\sigma}_\phi)(\sigma_\tau(n) - \overline{\sigma}_\tau)}{\sqrt{\sum_{n=1}^{N} (\sigma_\phi(n) - \overline{\sigma}_\phi)^2 \sum_{n=1}^{N} (\sigma_\tau(n) - \overline{\sigma}_\tau)^2}} \tag{5.6}$$

where $\overline{\sigma}_\phi$ and $\overline{\sigma}_\tau$ are the sample means of σ_ϕ and σ_τ, respectively. The calculated ρ yields 0.085, which indicates that the two domains are likely uncorrelated. This result is opposite to the result from the outdoor measurement [5], where a somewhat large correlation coefficient was reported. The assertion of the uncorrelatedness can be supported by the results from [22], where clearly increased azimuth spreads were reported from a hallway to rooms, even though the delay spreads in the rooms were smaller than in hallway. It should be yet noted that the uncorrelatedness does not generally imply the independence. However, the validity of (5.5) for the modeling is assumed as it was used by other authors [6], [7].

5.4.2 Power Delay Spectrum

The PDS is derived from (5.4) according to

$$P_d(\tau) = \int P_{ad}(\phi, \tau) d\phi. \tag{5.7}$$

First, the estimated parameter sets $\{\alpha_l, \tau_l, \phi_l\}$ were accumulated for the statistical analysis, then the empirical PDS was computed according to (5.7). Curve fitting was performed to the empirical PDS and the fit parameters were obtained by the maximum likelihood estimation for the exponential distribution. Though the empirical PDS does not fit perfectly with an exponential decaying function, the double exponential decaying functions match better as shown

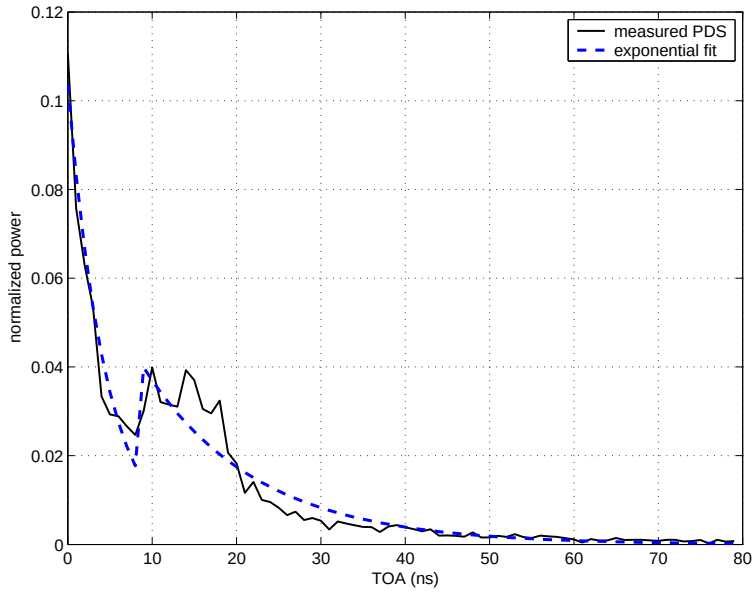

Figure 5.11: Power delay spectrum: $P(\tau) \propto \exp(-\tau/\sigma_{\tau,i})$, $\sigma_{\tau,1} = 4.53\ ns$, $\sigma_{\tau,2} = 13.35\ ns$.

in Fig. 5.11.

$$P_d(\tau) \propto \begin{cases} c_1 \exp(\frac{-\tau}{\sigma_{\tau_1}}) & 0 \leq \tau \leq 9\ ns \\ c_2 \exp(\frac{-\tau}{\sigma_{\tau_2}}) & \tau \geq 10\ ns. \end{cases} \tag{5.8}$$

5.4.3 Power Azimuth Spectrum

The PAS was also obtained from (5.4) according to

$$P_a(\phi) = \int P_{ad}(\phi, \tau) d\tau \tag{5.9}$$

In literature, different models for PAS (at lower frequencies) have been suggested. In [70], the PAS was derived using an elliptical scattering model resulting in a truncated Laplacian distribution. In [27] and [7], a Laplacian PAS was proposed for the outdoor and indoor measurements, respectively, while even an uniform PAS was proposed [8]. It was found that a typically observed PAS exhibits concentration virtually in a single azimuth direction. Curve fitting was performed for the measured PAS using the two candidate model functions and the results are shown in Fig. 5.12.

$$P(\phi) \propto \begin{cases} \exp(-\frac{\phi^2}{2\sigma_\phi^2}) & \text{Gaussian} \\ \exp(-\frac{\sqrt{2}|\phi|}{\sigma_\phi}) & \text{Laplacian} \end{cases} \tag{5.10}$$

The Gaussian function does not fit well at the center of azimuthal angles as well as at both tails, while the Laplacian function matches better with the measured PAS. The goodness of fit was performed by applying the *Kolmogorov-Smirnov* test. The hypothesis of being Gaussian

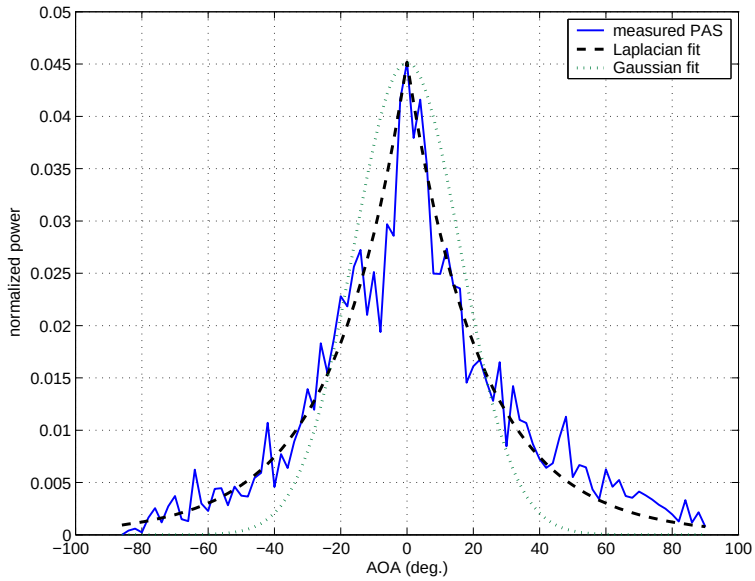

Figure 5.12: Power azimuth spectrum: measured PAS (solid line), Laplacian fit (dashed line) and Gaussian fit (doted line).

distributed was rejected at significance level 0.05, while the alternative hypothesis of being Laplacian distributed was accepted providing a p-value of 0.73.

5.4.4 Probability Density Function of TOA

The models for the relative delays and incidence azimuth angles were investigated. Since these parameters are time-variant in actual channels, they can be described by the probability density function (PDF) assuming that the relative delay and the incident azimuth angle are independent. Then the following relationship is assumed to be valid

$$f(\tau, \phi) \approx f(\tau) f(\phi), \tag{5.11}$$

where $f(\tau)$ and $f(\phi)$ are the PDFs for relative delays and azimuth angles respectively. A histogram analysis has been performed for the estimated relative delays. The histogram was generated using a width of 2 ns and the result is depicted in Fig. 5.13. An exponential decaying function turns out to be a good match to the histogram.

$$f(\tau) \propto \exp(-\frac{\tau}{\sigma_\tau}). \tag{5.12}$$

The *Kolmogorov-Smirnov* test was performed as the goodness of fit. The hypothesis of being exponentially distributed was accepted with a p-value of 0.72 for a 0.95 confidence level. Dissimilar models have been also suggested in literature. A non-homogeneous Poisson process was proposed by *Turin*, while *Suzuki* suggested a modified Poisson process. In [7] and [66], according to their measurement results at 5.2 GHz (indoor, 8 elements ULA and time resolution 8.3 ns)

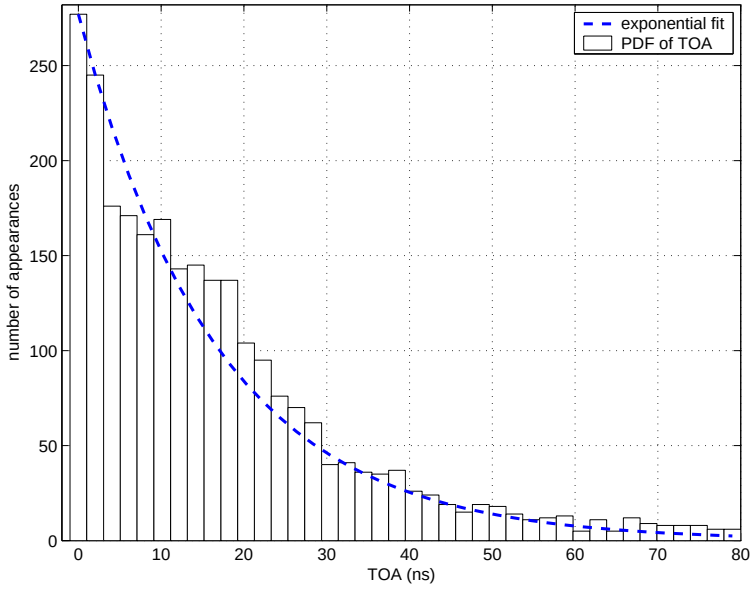

Figure 5.13: Probability density function of TOA.

and 24 GHz (indoor, 3-D virtual cross array, time resolution 2 ns), an exponential PDF for TOA was proposed.

5.4.5 Probability Density Function of AOA

In [6], the PDF for AOA was proposed to use a Laplacian PDF from the indoor measurements at 6.75 GHz, where clustering phenomenon was observed. Similar results were reported in [7], where the correlation between the spatial and temporal domains was investigated. In our experiment, the incisive clustering phenomenon could not be observed. This is most notably due to the fact that the sounding system provides limited RF power and the Tx antenna used does not exhibit an omnidirectional radiation pattern. Moreover, the high attenuation of reflected waves at 60 GHz might be another reason. A histogram analysis was performed for the estimated AOA obtained by SAGE. In Fig. 5.14, the two candidate PDF functions are compared with the measured PDF of AOA. Each bar of the histogram represents an AOA interval of 4.5°. The histogram can be well approximated by Laplacian PDF rather than Gaussian PDF.

$$f(\phi) \propto \exp(-\frac{\sqrt{2}|\phi|}{\sigma_\phi}). \tag{5.13}$$

The Gaussian PDF fails to reproduce the peaks at the top showing a relatively large deviation at both tails from the histogram. The fit parameters for the Laplacian PDF were determined by applying a maximum likelihood fitting. As the goodness of fit, the *Kolmogorov-Smirnov* test was performed. The hypothesis of being Laplacian distributed was accepted with a p-value of 0.86 for a 0.95 confidence level, while the hypothesis of Gaussian PDF was rejected. The proposed empirical space-time channel models are summarized in Table. 5.2.

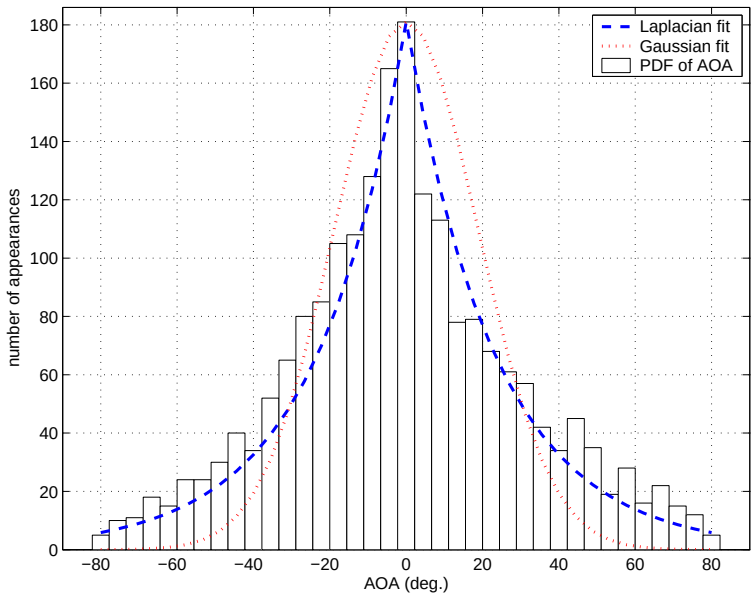

Figure 5.14: Probability density function of AOA

	Model
Power Delay Spectrum	Exponential: $P(\tau) \propto c_i \exp(-\frac{\tau}{\sigma_{\tau_i}}),\ i = \{1, 2\}$
Power Azimuth Spectrum	Laplacian: $P(\tau) \propto \exp(-\sqrt{2}\frac{\lvert\phi\rvert}{\sigma_\phi})$
PDF for the relative delays	Exponential: $f(\tau) \propto \exp(-\frac{\tau}{\sigma_\tau})$
PDF for the azimuth angles	Laplacian: $f(\phi) \propto \exp(-\frac{\sqrt{2}\lvert\phi\rvert}{\sigma_\phi})$

Table 5.2: Summary of the empirical space-time channel models.

5.5 Summary and Conclusion

In this chapter, the results from the space-time channel measurements at 60 GHz in the corridors of an office building were presented [19]. Multipath components were resolved in time domain with a time resolution of about 1 ns and in spatial domain using an 1×4 array antenna. The LOS path was always present during the measurement campaign. From the collected channel data, the empirical channel parameters with respect to TOA ($\sigma_\tau, \overline{\tau}, B_\rho$, K-factor) as well as to AOA (σ_ϕ) were analyzed. The maximum delay spread (σ_τ) was found to be 13.06 ns and the average σ_τ was 2.93 ns. The average mean excess delay ($\bar{\tau}$) was determined as 5.76 ns. An average K-factor of 5.93 dB was estimated. The maximum attainable coherence bandwidth appeared to be $B_{0.9} = 56\ MHz$ and the average azimuth spread (σ_ϕ) was found to be 18.25°. In context with environment-specific information, it was found that multipath components are largely constrained along the LOS path. Furthermore, good correlation between the multipath structure and the propagation environment was observed. This observation is also well reflected in the empirical space-time channel models, where a typical PAS was found to be concentrated virtually in a single azimuth direction showing a good match with the Laplacian distribution. The PDS can be described by two exponential decaying functions. Performing the histogram analysis for the relative delays, an exponential PDF was found to be most suitable with fit parameter σ_τ. The empirical PDF for the azimuth angles was modeled by the Laplacian PDF. The Gaussian PDF failed to fit at top and both tails of the measured azimuth angles. These results will help not only to gain more insight into the multipath structure, but also can be well used for the design and performance evaluation of 60 GHz systems.

Chapter 6

Conclusions and Future Work

6.1 Summary of the Main Results

This dissertation deals with the indoor measurement of the radio propagation channel at 60 GHz in the corridors of an office building and investigates the channel characteristics with regard to temporal and spatial multipath structure. It is focused mainly on two parts: In the first part, the problem of wideband channel measurement using a narrowband system is addressed. The second part covers the measurement system setup and the statistical analysis of the measurement data with respect to channel parameters as well as empirical space-time channel models.

In chapter 2, relevant terms relating to the radio propagation channel and the associated parameters were discussed. Moreover, measurement techniques for time and spatial domains as well as known channel models for smart antenna systems and multi-dimensional parameter estimation techniques were reviewed.

In Chapter 3, the problem of channel reconstruction was investigated when using a narrowband system and employing an antenna array for wideband channel measurement, if the measurement system lacks the required synchronization to a common reference clock. To achieve wideband channel measurement using a narrowband system, the consecutively measured sub-channels have to be compensated with respect to phase offsets to represent the correct CIR. Two concatenation methods were investigated: the overlap method and the extrapolation method. Improvements were achieved by exploiting redundant information from the antenna array channels and optimal choice of the compensation reference. The extrapolation method with utilizing the proposed enhancements and the overlap method were examined by simulative error analysis.

It was shown that the extrapolation method with both enhancements (Sec. 3.3.2.C and Sec. 3.3.2.D) outperformed the overlap method clearly. With sufficiently high SNRs ($\geq$ 50 dB) and using a relatively small number of concatenations ($N_c = \{5, 10, 20\}$), the performance lower bound could be nearly approached by applying the improved extrapolation method. Using a large concatenation number of $N_f = 160$, an average compensation error of phase offset less than 2.81° and relative errors for channel parameters such as RMS delay spread and RMS mean excess delay smaller than 0.7 % and 0.6 %, respectively, could be still achieved for SNR=50 dB. Furthermore, error propagation was significantly mitigated by the improvements to the concatenation method.

The measurement system setup was presented in chapter 4. The measurement system primarily consisted of a 60 GHz 1×4 patch antenna array and a digital array transceiver system, that allowed parallel baseband conversion of the antenna array signals. Hence, the digital array transceiver in conjunction with the 60 GHz patch antenna array facilitated the design of the space-time channel measurement system. The sampling timing offset could be minimized by connecting the Tx and Rx sampling modules to a common 16 MHz sampling clock. Frequency stability was achieved by synchronizing all synthesizers to a 10 MHz reference signal apart from the local oscillator in the digital array transceiver. The consecutively measured 178 sub-channels were reconstructed and concatenated using the compensation method described in chapter 3 to achieve the desired RF-bandwidth of 1 GHz. Thus, multipath components could be resolved in time domain with a time resolution of about 1 ns and in space domain with the antenna array. The SAGE algorithm was applied for extracting the parameters of multipath components from the measured channel data. The reliability of the channel sounder used was successfully examined with reference measurements and demonstrated by means of some measurement examples.

The results from the statistical analysis of the data obtained by measurements at 60 GHz in the corridors of an office building were presented in chapter 5. The channel parameters with respect to the TOA as well as to the AOA were analyzed: the maximum and average RMS delay spread values were found to be 13.06 ns and 2.93 ns, respectively. The average K-factor of 5.93 dB was determined. The coherence bandwidth values remained below $B_{0.9} = 56$ MHz. The average azimuth spread was 18.25°. Empirical space-time channel models were presented. Typical PAS was found to be concentrated virtually in a single azimuth direction showing a good match with the Laplacian distribution. The empirical PDS can be described by two exponential decaying functions. It was found that the empirical PDF for azimuth angles can be modeled by the Laplacian PDF, while the exponential PDF turned out to be most suitable for modeling of the relative delays. These results will help to gain more insight into the multipath structure and can be well used for the design as well as the performance evaluation for 60 GHz systems.

6.2 Future Work

The research can be extended or stretched into several directions through future work. Some possible extensions of research can be outlined as follows:

- It would be meaningful to extend the investigation into channel parameter domains such as elevation angle and doppler shift. By adding additional parameter domains, the multipath structure can be revealed more insightfully. The quality of joint parameter estimation would be enhanced largely resulting in more reliable channel modeling. Measurements presented in this work were conducted only in corridors. Expanding the measurement campaign to environments of different types such as dissimilar-sized rooms can be interesting, so that channel characteristics can be classified according to them.

- Polarization dependence of channel parameters has been reported in several publications. Space-Time channel models in conjunction with polarization will provide very useful information for future system design in terms of exploiting the polarization diversity.

- A comparative study between the measurement and prediction by ray-tracing would be highly interesting. The ray-tracing technique was reported frequently in several publications to be suitable for application for mm-wave frequency environment. Adaptation of measurement results into the ray-tracing technique and following comparison would be meaningful.

List of Tables

3.1 Standard deviation of RMS compensation error (deg.): $N_{sub} = 160$ 53
3.2 Standard deviation of relative RMS delay spread error (%): $N_{sub} = 160$ 53
3.3 Standard deviation of relative RMS mean excess delay error (%): $N_{sub} = 160$ . . 53

5.1 Summary of the TOA and AOA statistics. 76
5.2 Summary of the empirical space-time channel models. 82

B.1 Standard deviation of RMS compensation error (deg.): $N_{sub} = 160,\ N_f = \{16, 32\}$ 96
B.2 Standard deviation of relative RMS delay spread error (%): $N_{sub} = 160,\ N_f = \{16, 32\}$ 97
B.3 Standard deviation of relative RMS mean excess delay error (%): $N_{sub} = 160,\ N_f = \{16, 32\}$ 97

C.1 Std. of RMS compensation error of phase offset (deg.) dependent on the number N_c of concatenations. 98
C.2 Std. of relative RMS delay spread error (%) dependent on the number N_c of concatenations. 98
C.3 Std. of relative RMS mean excess delay error (%) dependent on the number N_c of concatenations. 98

List of Figures

2.1 Multipath Propagation in mobile radio communication. 9
2.2 Spatial measurement using an antenna array: (a) real time parallel measurement [27], (b) measurement by multiplexing of array outputs [28]. 13
2.3 Other spatial measurement examples: (a) virtual cross array using a single $\lambda/4$ monopole antenna and positioning by a stepping motor [29], (b) measurement using a highly directional antenna rotated in the azimuthal directions [22]. 14
2.4 Lee's Model. 15
2.5 Circular scatterer density geometry. 16
2.6 Elliptical scatterer density geometry. 17
2.7 GWSSUS geometry with three clusters and the mean DOA ϕ_{0k}. 17
2.8 Geometry of the uniform sectored distribution. 20
2.9 Observation window for $\mathbf{Y}(t)$. 22

3.1 Measurement procedure by sweep of RF center frequency: total measurement RF-bandwidth B_{total} is divided into N_{sub} bandwidths. A sub-channel provides the bandwidth of B_{sub} consisting of N_f sub-carriers. 31
3.2 Measurement procedure for the overlap method. 32
3.3 Relative delay spread error in (%) as a function of the averaged phase offset over 160 sub-channels. 38
3.4 Relative mean excess delay error in (%) as a function of the averaged phase offset over 160 sub-channels. 39
3.5 Spurious peaks cased by rapidly changing phase offsets. 39
3.6 RMS compensation errors as functions of the SNR values of the measurement system: extrapolation method with N_f={8, 16, 32}, overlap method and reference as lower bound. 41
3.7 Relative RMS delay spread errors as functions of SNR values of measurement system. 42
3.8 Relative RMS mean excess delay errors as functions of the SNR values of the measurement system. 43
3.9 Relative RMS coherence bandwidth errors as functions of the SNR values of the measurement system: errors in number of frequency separation. 43

3.10 Illustration of using redundant information: phase response functions of the reference and reconstructed array channels at sub-channel # 38 and # 39. The phase response function of array channel # 1 exhibits a large error propagation beginning at sub-channel # 39. 44
3.11 Illustration of compensation phases (calculated according to (3.33)) relating to Fig. 3.10: a large estimation error between sub-channel #38 and #39 for array channel # 1, the estimates of other array channels lie closely. 44
3.12 Enhancement # 2: forward and backward compensation by splitting the phase matrix $\widetilde{\Phi}_{H_{total}}$ in two parts relative to the middle reference sub-channel. 49
3.13 RMS compensation errors vs. SNR values: the previous extrapolation method (legend "old": see Sec. 3.3.2.B and Fig. 3.6) and improved extrapolation method (legend "Enh.#1": enhancement summarized in Sec. 3.3.2.C), overlap method and reference error statistics as lower bounds, $N_{sub} = 160$, $N_f = \{16, 32\}$. 49
3.14 RMS compensation errors vs. SNR values: previous extrapolation method (legend "old": results from Sec. 3.3.2.B) and improved extrapolation method (legend "Enh.#1+Enh.#2": both enhancements described in Sec. 3.3.2.C and Sec. 3.3.2.D), overlap method and reference error statistics as lower bounds, $N_{sub} = 160$, $N_f = \{16, 32\}$ 51
3.15 Relative RMS delay spread errors vs. SNR values: previous extrapolation method (legend "old": results from Sec. 3.3.2.B) and improved extrapolation method (legend "Enh.#1+Enh.#2": both enhancements described in Sec. 3.3.2.C and Sec. 3.3.2.D), overlap method and reference error statistics as lower bounds, $N_{sub} = 160$, $N_f = \{16, 32\}$. 51
3.16 Relative RMS mean excess delay errors vs. SNR values: previous extrapolation method (legend "old": results from Sec. 3.3.2.B) and improved extrapolation method (legend "Enh.#1+Enh.#2": both enhancements described in Sec. 3.3.2.C and Sec. 3.3.2.D), overlap method and reference error statistics as lower bounds, $N_{sub} = 160$, $N_f = \{16, 32\}$. 52
3.17 Relative RMS coherence bandwidth errors vs. SNR values: previous extrapolation method (legend "old": results from Sec. 3.3.2.B) and improved extrapolation method (legend "Enh.#1+Enh.#2": both enhancements described in Sec. 3.3.2.C and Sec. 3.3.2.D), overlap method and reference error statistics as lower bounds, $N_{sub} = 160$, $N_f = \{16, 32\}$. 52
3.18 RMS compensation errors ($\zeta_{rms,EP}$) against the number of concatenations N_c and SNR of the measurement system. 54
3.19 Relative RMS delay spread errors ($e_{ds,rel,EP}$) against the number of concatenations N_c and SNR of the measurement system. 55
3.20 Relative RMS mean excess delay errors ($e_{ed,rel,EP}$) against the number of concatenations N_c and SNR of the measurement system. 55

3.21 An exemplary histogram analysis of compensation errors at sub-channel #90 and sub-channel #140, respectively: errors collected over 500 simulation runs (SNR=50 dB). 56
3.22 Average compensation error (left) and its standard deviation (right) vs. number of sub-channels using the extrapolation method with $N_f = 32$. 56

4.1 (a) Digital array transceiver: eight IF inputs at 200 MHz, 10 bit resolution with the sampling frequency of 16 MHz, data transfer to PC over EPP interface, (b) Tx modulator with an external LO input and an IF output. 59
4.2 (a) RF-Frontend: power amplifiers, mixers and LO distribution network, (b) 1×4 patch array antenna with 0.5 λ element spacing and its cross sectional view. . . . 60
4.3 Radiation pattern of Tx and Rx antennas: (a) open-ended waveguide, (b) 60 GHz 1×4 patch array antenna. 61
4.4 Transmit signal frame structure. (a) Signal slot: 16 single tone signals with a total transmit duration of 1.5 ms, sub-carrier spacing is 400 kHz. (b) Signal Frame: midamble signal for frame synchronization, a maximum of 9 redundant signal slots can be added. 61
4.5 The channel sounder setup. Tx: 0.8-2.5 GHz IQ-modulator, IF-synthesizer SMIQ at 1.8 GHz, 60 GHz Tx synthesizer (Agilent 83650B), 60 GHz bandpass filter and 60 GHz amplifier, Rx: 1x4 digital array transceiver (IF at 200 MHz), LO distribution network, 1×4 patch array antenna, power amplifiers, mixers and 60 GHz Rx synthesizer (HP 83623B). 62
4.6 The designed 60 GHz space-time channel sounder. 63
4.7 The chamber for the antenna array calibration. 63
4.8 Results of the measurement system calibration: (a) CDF of the amplitude fluctuations, (b) CDF of the phase fluctuations. 64
4.9 Reference measurements: expected incident waves (a direct and a reflected wave) at 0° and 27°, respectively, estimated parameters $\theta_\ell = \{\alpha_\ell, \tau_\ell, \phi_\ell\}$: $\theta_1 = \{1, 0\, ns, 0°\}$, $\theta_2 = \{0.2, 1\, ns, 26.6°\}$ 65
4.10 A measurement example for a gangway (corridor I, Tx-Rx separation: 3.5 m): measured (solid line) and reconstructed (dashed line) CFRs (reconstructed CFR based on SAGE estimates). 66
4.11 Measured (solid line) and reconstructed (dashed line) PAPs associated with Fig. 4.10 66
4.12 A measurement example for a room (Tx-Rx separation: 3.3 m): measured (left, solid line) and reconstructed (left, dashed line) CFRs (reconstructed CFR based on SAGE estimates) 67
4.13 Measured (solid line) and reconstructed (dashed line) PAPs relating to Fig. 4.12 67

5.1 Site Description: corridor I: $1.3 \times 13.07 \times 2.57\ m$, corridor II: $3.07 \times 12.25 \times 2.57\ m$, corridor III: $5.5 \times 12.25 \times 2.57\ m$. 70

5.2 Layout of the laboratory. 71
5.3 Location 1 in laboratory: PAP obtained using an open-ended wave guide (solid line) and a 20 dB TE10 horn antenna (dashed line). 72
5.4 Location 2 in laboratory: PAP obtained using an open-ended wave guide (solid line) and a 20 dB TE10 horn antenna (dashed line). 72
5.5 Location 3 in laboratory: PAP obtained using an open-ended wave guide (solid line) and a 20 dB TE10 horn antenna (dashed line). 73
5.6 The CDF of the RMS delay spread (σ_τ). 74
5.7 The CDF of the RMS mean excess delay ($\bar{\tau}$). 74
5.8 The CDFs of the coherence bandwidth (B_ρ): $B_{0.5}$ (solid line), $B_{0.9}$ (dashed line). 75
5.9 The CDF of the Ricean K factor. 76
5.10 The CDF of the azimuth spread (σ_ϕ). 77
5.11 Power delay spectrum: $P(\tau) \propto \exp(-\tau/\sigma_{\tau,i})$, $\sigma_{\tau,1} = 4.53\ ns$, $\sigma_{\tau,2} = 13.35\ ns$. . . 79
5.12 Power azimuth spectrum: measured PAS (solid line), Laplacian fit (dashed line) and Gaussian fit (doted line). 80
5.13 Probability density function of TOA. 81
5.14 Probability density function of AOA 82

B.1 Relative RMS delay spread errors vs. SNR values: the previous extrapolation method (legend "old": see Sec. 3.3.2.B and Fig. 3.6) and improved extrapolation method (legend "Enh.#1": enhancement summarized in Sec. 3.3.2.C), overlap method and reference error statistics as lower bounds, $N_{sub} = 160$, $N_f = \{16, 32\}$. 96
B.2 Relative RMS mean excess delay errors vs. SNR values: the previous extrapolation method (legend "old": see Sec. 3.3.2.B and Fig. 3.6) and improved extrapolation method (legend "Enh.#1": enhancement summarized in Sec. 3.3.2.C), overlap method and reference error statistics as lower bounds, $N_{sub} = 160$, $N_f = \{16, 32\}$. 97

D.1 Average compensation error (left) and its standard deviation (right) vs. number of sub-channels using the overlap method. 99

E.1 Corridor type I: $1.3 \times 13.07 \times 2.57\ m$. 100
E.2 Corridor type II: $3.07 \times 12.25 \times 2.57\ m$ 101
E.3 Corridor type III: $5.5 \times 12.25 \times 2.57\ m$ 101

F.1 Measured and reconstructed (based on SAGE estimates) CFRs at location 1 in laboratory. 102
F.2 Measured and reconstructed (based on SAGE estimates) CFRs at location 2 in laboratory. 103
F.3 Measured and reconstructed (based on SAGE estimates) CFRs at location 3 in laboratory. 103

F.4 PAP obtained using the open-ended wave guide in corridor III, Tx-Rx separation: 5.5 m. 104
F.5 Measured and reconstructed (based on SAGE estimates) CFRs in corridor III ($5.5 \times 12.25 \times 2.57\ m$), Tx-Rx separation: 5.5 m. 104
F.6 PAP obtained using the open-ended wave guide in corridor III, Tx-Rx separation: 7.5 m. 105
F.7 Measured and reconstructed (based on SAGE estimates) CFRs in corridor III ($5.5 \times 12.25 \times 2.57\ m$), Tx-Rx separation: 7.5 m. 105

Appendices

Appendix A

Acronyms

AOA angle of arrival

BS base station

CDF cumulative distribution function

CDMA code division multiple access

CFR channel frequency response

CIR channel impulse response

DMB digital multimedia broadcasting

DOA direction of arrival

DVB-T/S digital video broadcasting-terrestrial/satellite

EM expectation maximization

ESPRIT estimation of signal parameters via rotational invariance technique

FDSAGE frequency domain SAGE

GBSBSCM geometrically based single bounce statistical channel models

GBSB geometrically based single bounce

GSM global system for mobile communication

GWSSUS gaussian wide sense stationary uncorrelated scattering

I/Q in-phase/ quadrature

JADE joint angle and delay estimation

LOS line of sight

MIMO multiple input multiple output

MMSE minimum mean square error

MS mobile station

MUSIC multiple signal classification

OFDM orthogonal frequency-division multiplex

PAP power azimuth profile

PAS power azimuth spectrum

PDF probability density function

PDP power delay profile

PDS power delay spectrum

PIC parallel interference cancellation

RMS root mean square

Rx receiver

SAGE space-alternating generalized expectation

SIC successive interference cancellation

SVD singular value decomposition

TOA time of arrival

Tx transmitter

ULA uniform linear array

UMTS universal mobile telecommunications system

URA uniform rectangular array

US uncorrelated scattering

VNA vector network analyzer

WLAN wireless local area network

WSSUS wide sense stationary uncorrelated scattering

WSS wide sense stationary

Appendix B

Error Statistics to Sec. 3.3.2. E, "Enh.#1".

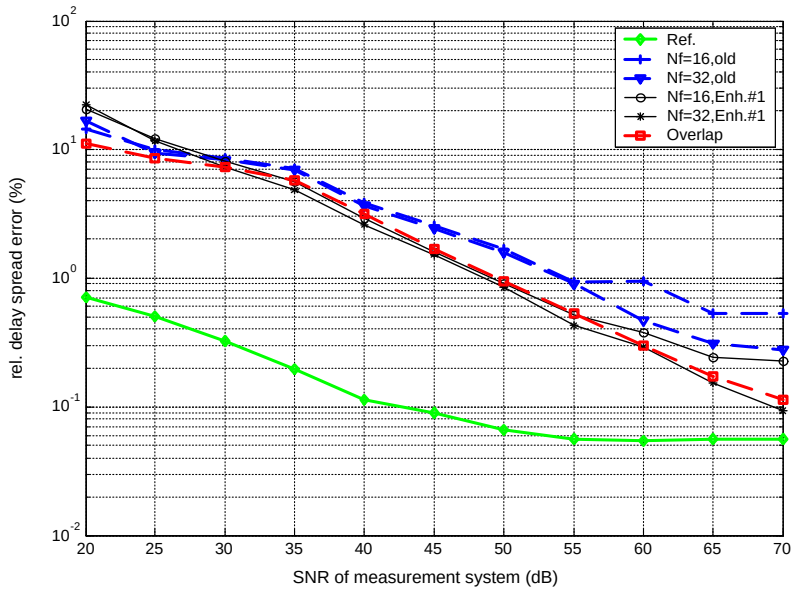

Figure B.1: Relative RMS delay spread errors vs. SNR values: the previous extrapolation method (legend "old": see Sec. 3.3.2.B and Fig. 3.6) and improved extrapolation method (legend "Enh.#1": enhancement summarized in Sec. 3.3.2.C), overlap method and reference error statistics as lower bounds, $N_{sub} = 160$, $N_f = \{16, 32\}$.

SNR (dB)	$N_f = 16$, old	$N_f = 16$, Enh.#1	$N_f = 32$, old	$N_f = 32$, Enh.#1	Overlap	Reference
30	28.04	22.05	28.06	21.86	26.27	0.59
40	18.76	7.90	16.46	6.42	12.17	0.21
50	13.87	3.14	7.69	2.33	3.96	0.16
60	10.81	3.57	5.32	0.85	2.06	0.19
70	12.25	4.90	7.50	0.35	0.56	0.19

Table B.1: Standard deviation of RMS compensation error (deg.): $N_{sub} = 160$, $N_f = \{16, 32\}$

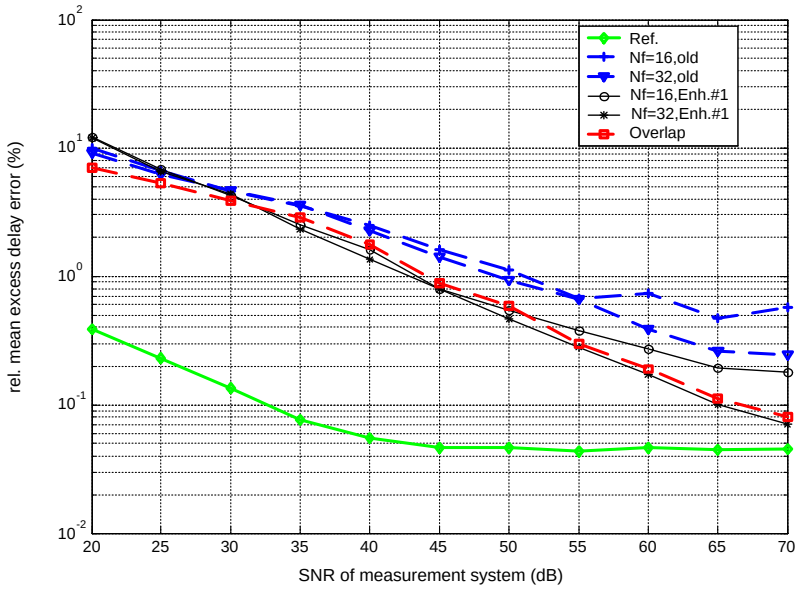

Figure B.2: Relative RMS mean excess delay errors vs. SNR values: the previous extrapolation method (legend "old": see Sec. 3.3.2.B and Fig. 3.6) and improved extrapolation method (legend "Enh.#1": enhancement summarized in Sec. 3.3.2.C), overlap method and reference error statistics as lower bounds, $N_{sub} = 160$, $N_f = \{16, 32\}$.

SNR (dB)	$N_f = 16$, old	$N_f = 16$, Enh.#1	$N_f = 32$, old	$N_f = 32$, Enh.#1	Overlap	Reference
30	14.82	16.97	13.32	9.97	12.87	0.49
40	6.88	5.87	6.57	4.87	6.36	0.18
50	5.04	1.95	4.50	1.65	2.30	0.08
60	2.51	0.70	0.98	0.64	0.53	0.05
70	1.40	0.65	0.97	0.17	0.16	0.06

Table B.2: Standard deviation of relative RMS delay spread error (%): $N_{sub} = 160$, $N_f = \{16, 32\}$

SNR (dB)	$N_f = 16$, old	$N_f = 16$, Enh.#1	$N_f = 32$, old	$N_f = 32$, Enh.#1	Overlap	Reference
30	4.87	4.74	5.04	4.72	4.49	0.12
40	3.43	2.22	3.12	1.79	2.79	0.05
50	1.99	0.69	1.38	0.63	0.97	0.05
60	1.58	0.43	1.04	0.26	0.26	0.05
70	1.57	0.42	0.96	0.11	0.09	0.05

Table B.3: Standard deviation of relative RMS mean excess delay error (%): $N_{sub} = 160$, $N_f = \{16, 32\}$

Appendix C

Error Statistics to Sec. 3.3.2. F.

SNR (dB)	$N_c = 5$	10	20	40	80	160	Reference
30	4.33	4.06	4.40	5.70	7.86	11.48	0.53
40	1.54	1.49	1.23	1.78	4.89	4.31	0.22
50	0.74	0.85	0.49	1.18	2.82	1.96	0.17
60	0.40	0.62	0.75	0.42	0.46	1.17	0.19
70	0.58	0.48	0.59	0.49	0.47	0.73	0.18

Table C.1: Std. of RMS compensation error of phase offset (deg.) dependent on the number N_c of concatenations.

SNR (dB)	$N_c = 5$	10	20	40	80	160	Reference
30	2.49	2.48	3.13	8.26	7.16	15.23	0.41
40	0.95	1.27	1.97	2.39	4.56	6.03	0.19
50	0.30	0.40	0.55	0.58	0.73	1.14	0.06
60	0.10	0.81	0.16	0.22	0.51	0.49	0.05
70	0.15	0.06	0.07	0.08	0.11	0.23	0.05

Table C.2: Std. of relative RMS delay spread error (%) dependent on the number N_c of concatenations.

SNR (dB)	$N_c = 5$	10	20	40	80	160	Reference
30	1.22	1.15	1.51	2.77	2.96	5.01	0.11
40	0.57	0.48	0.62	0.70	1.24	1.90	0.05
50	0.15	0.14	0.19	0.23	0.43	0.51	0.04
60	0.06	0.74	0.13	0.16	0.16	0.26	0.05
70	0.08	0.05	0.05	0.08	0.10	0.19	0.05

Table C.3: Std. of relative RMS mean excess delay error (%) dependent on the number N_c of concatenations.

Appendix D

Figure to Sec. 3.3.2. G.

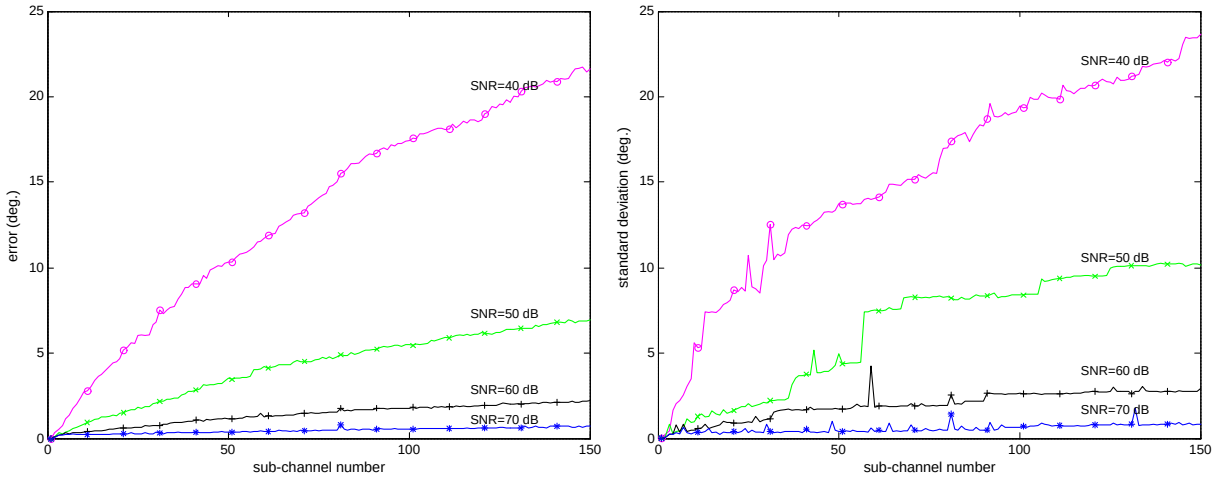

Figure D.1: Average compensation error (left) and its standard deviation (right) vs. number of sub-channels using the overlap method.

Appendix E

Site Photos.

Figure E.1: Corridor type I: $1.3 \times 13.07 \times 2.57\ m$.

Figure E.2: Corridor type II: $3.07 \times 12.25 \times 2.57\ m$

Figure E.3: Corridor type III: $5.5 \times 12.25 \times 2.57\ m$

Appendix F

Measured and Reconstructed PAPs.

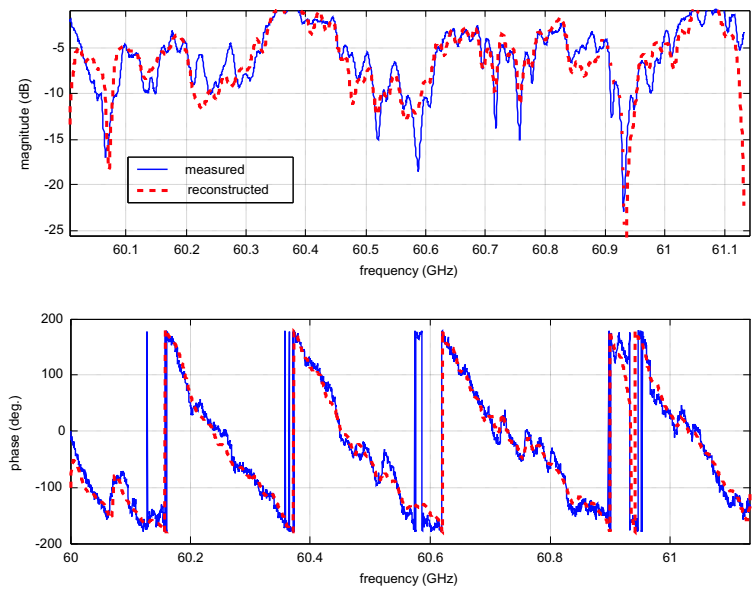

Figure F.1: Measured and reconstructed (based on SAGE estimates) CFRs at location 1 in laboratory.

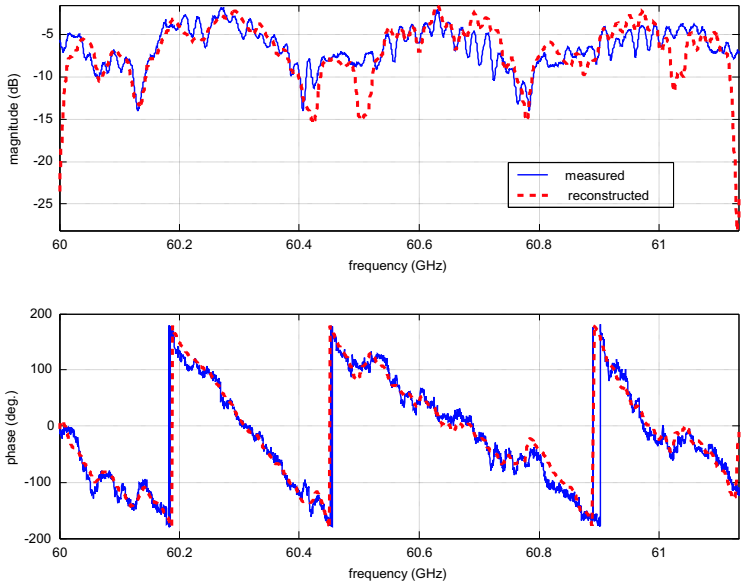

Figure F.2: Measured and reconstructed (based on SAGE estimates) CFRs at location 2 in laboratory.

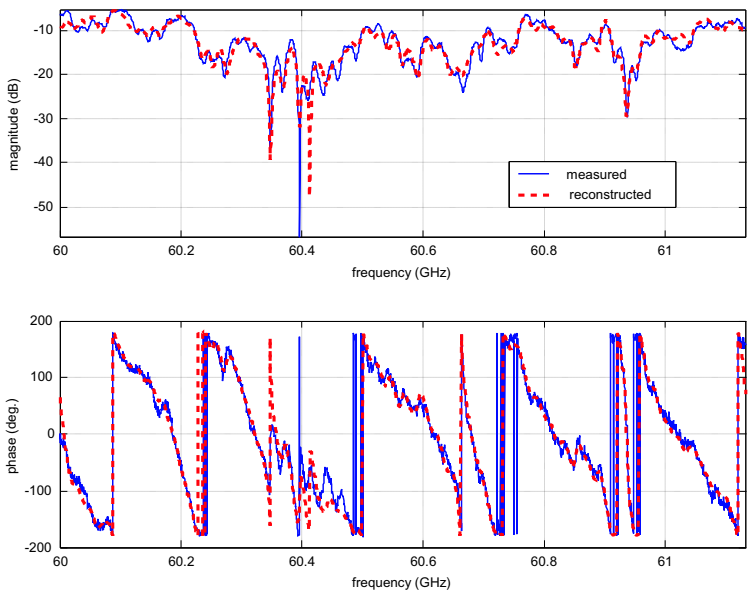

Figure F.3: Measured and reconstructed (based on SAGE estimates) CFRs at location 3 in laboratory.

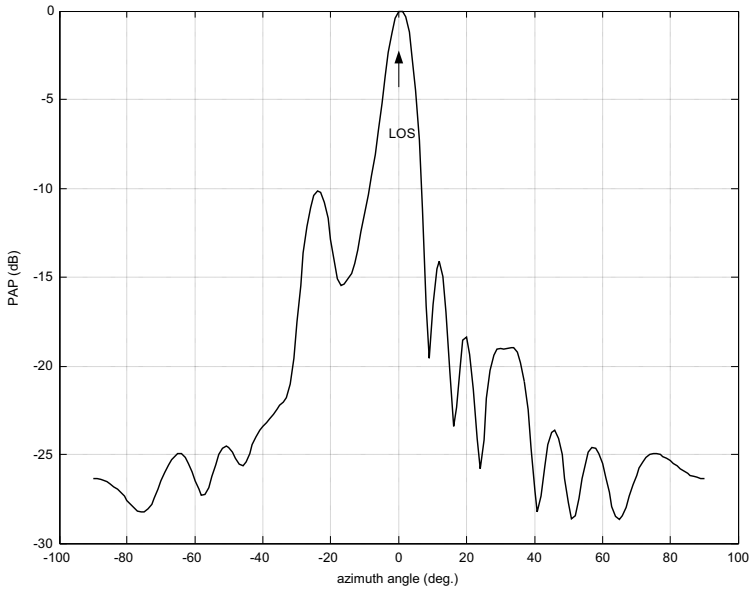

Figure F.4: PAP obtained using the open-ended wave guide in corridor III, Tx-Rx separation: 5.5 m.

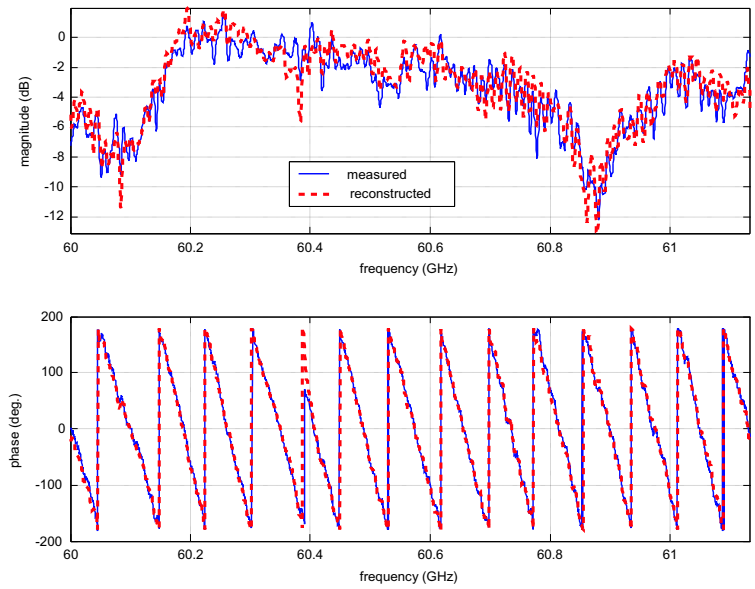

Figure F.5: Measured and reconstructed (based on SAGE estimates) CFRs in corridor III ($5.5 \times 12.25 \times 2.57\ m$), Tx-Rx separation: 5.5 m.

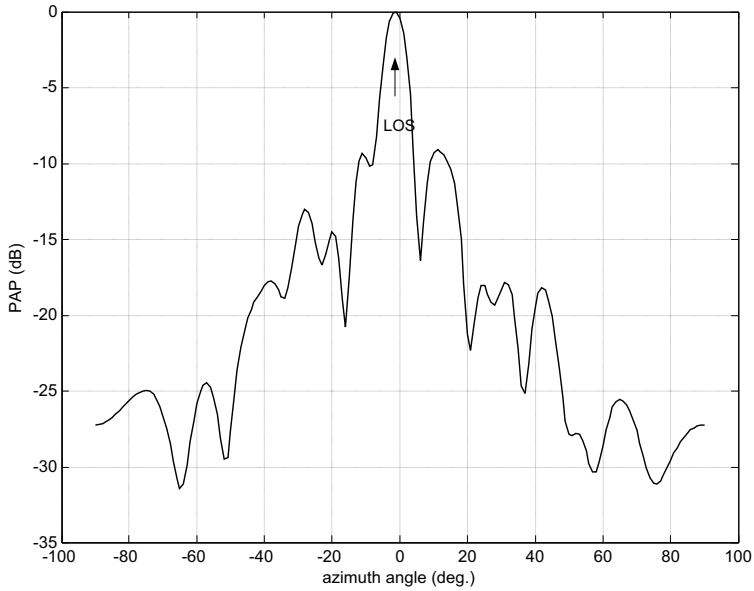

Figure F.6: PAP obtained using the open-ended wave guide in corridor III, Tx-Rx separation: 7.5 m.

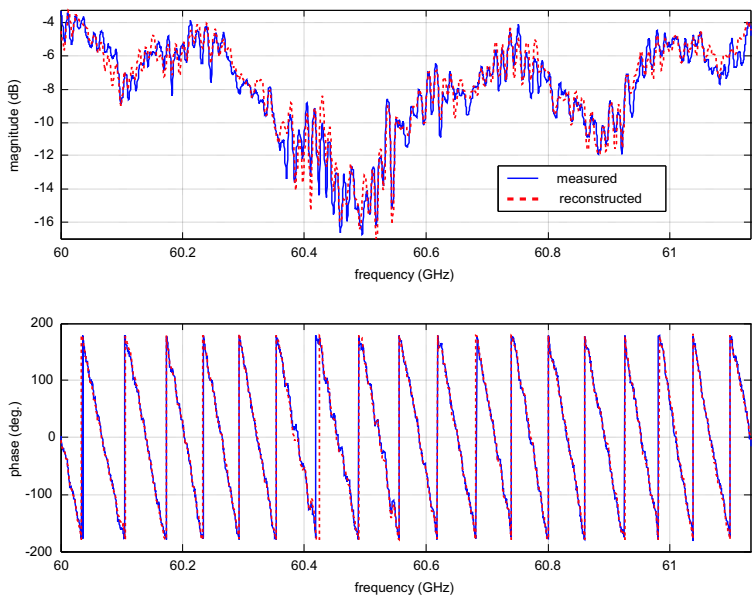

Figure F.7: Measured and reconstructed (based on SAGE estimates) CFRs in corridor III ($5.5 \times 12.25 \times 2.57\ m$), Tx-Rx separation: 7.5 m.

Bibliography

[1] J. C. Liberty Jr. and T. S. Rappaport, *Smart Antennas for Wireless Communications: IS-95 and Third Generation CDMA Applications.* Upper Saddle River, NJ 07458, Prentice Hall, 1999.

[2] L. C. Godara, "Part I: Applications of antenna arrays to mobile communications," *Proc. IEEE*, vol. 85, pp. 1031–1060, July 1997.

[3] M. Luise, F. Giannetti, and R. Reggiannini, "Mobile and personal communications in the 60 GHz band: a survey," *WIRELESS PERSONAL COMMUNICATIONS*, vol. 10, no. 2, pp. 207–243, 1999.

[4] P. Smulders, "Exploiting the 60 GHz band for local wireless multimedia access: Prospects and future directions," *IEEE Commun. Mag*, vol. 40, pp. 140–147, January 2002.

[5] K. Pedersen, P. Mogensen, and B. Fleury, "A stochastic model of the temporal and azimuthal dispersion seen at the base station in outdoor propagation environments," *IEEE Transactions on Vehicular Technology*, vol. 49, pp. 437–447, March 2000.

[6] Q. H. Spencer, B. D. Jeffs, M. A. Jensen, and A. L. Swindlehurst, "Modeling the statistical time and angle of arrival characteristics of an indoor multipath channel," *IEEE Journal on Selected Areas in Communications*, vol. 18, No. 3, pp. 347–360, March 2000.

[7] C.-C. Chong, D. I. Laurenson, and S. McLaughlin, "Statistical characterization of the 5.2 GHz wideband directional indoor propagation channels with clustering and correlation properties," *Vehicular Technology Conference, Proceedings. VTC 2002-Fall*, vol. 1, pp. 629–633, Sept 2002.

[8] R. Heddergott and P. Truffer, "Statistical characteristics of indoor radio propagation in NLOS scenarios," *COST 259 TD (00) 024*, Jan. 2000.

[9] P. Bello, "Characterization of randomly time-variant linear channels," *IEEE Transactions on Communications*, vol. 11, pp. 360–393, Dec. 1963.

[10] J. McKown and J. Hamilton, "Ray tracing as a design tool for radio networks," *IEEE Network Magazine*, vol. 5, pp. 27–30, Nov. 1991.

[11] S. Seidel and T. Rappaport, "A ray tracing technique to predict path loss and delay spread inside buildings," *IEEE Global Telecommunications Conference*, vol. 2, pp. 649–653, Dec. 1992.

[12] F. Adana, O. Blanco, I. Diego, J. Arriaga, and M. Catedra, "Propagation model based on ray tracing for the design of personal communication systems in indoor environments," *IEEE Transactions on Vehicular Technology*, vol. 49, pp. 2105–2112, Nov. 2000.

[13] K. A. Remley, H. R. Anderson, and A. Weisshar, "Improving the accuracy of ray-tracing techniques for indoor propagation modeling," *IEEE Transactions on Vehicular Technology*, vol. 49, pp. 2350–2358, Nov 2000.

[14] H. Hashemi, "The indoor radio propagation channel," *Proceedings of IEEE*, vol. 81, pp. 943–968, July 1993.

[15] E. Zollinger, *Eigenschaften von Funkübertragungsstrecken in Gebäude*. PhD thesis, 1993.

[16] L. Clavier, M. Rachdi, M. Fryziel, Y. Delignon, V. L. Thuc, C. Garnier, and P. Rolland, "Wide band 60 GHz indoor channel: characterization and statistical modeling," *Vehicular Technology Conference, VTC 2001 Fall*, vol. 4, pp. 2098–2102, October 2001.

[17] J. Purwaha, A. Mank, D. Matic, K. Witrisal, and R. Prasad, "Wide-band channel measurements at 60 GHz in indoor environments," *Proceedings Sixth Symposium on Vehicular Technology and Communications*.

[18] R. Davies, M. Bensebti, M. Beach, and J. McGeehan, "Wireless propagation measurements in indoor multipath environments at 1.7 GHz and 60 GHz for small cell systems," *IEEE Vehicular Technology Conference*, pp. 589–593, May 1991.

[19] M. S. Choi, G. Grosskopf, and D. Rohde, "Statistical characteristics of 60 GHz wideband indoor propagation channel," *IEEE 16th International Symposium on Personal, Indoor and Mobile Radio Communications*, vol. 1, pp. 599–603, September 2005.

[20] T. Zwick, T.J.Beukema, and H. Nam, "Wideband channel sounder with measurements and model for the 60 GHz indoor radio channel," *IEEE Transactions on Vehicular Technology*, vol. 54, pp. 1266–1277, July 2005.

[21] P. Smulders and L. Correia, "Characterisation of propagation in 60 GHz radio channels," *Electronics and Communication Engineering Journal*, vol. 9, pp. 73–80, April 1997.

[22] Hao.Xu, V. Kukshya, and T. S. Rappaport, "Spatial and temporal characteristics of 60 GHz indoor channels," *IEEE Journal on Selected Areas in Communications*, vol. 20, pp. 620–630, April 2002.

[23] A. Siamarou and M. Al-Nuaimi, "Wideband propagation measurements for indoor rician fading radio channels at 62.4 GHz," *IEEE Vehicular Technology Conference*, vol. 1, pp. 449–453, May 2001.

[24] J. D. Gibson, "Mobile communications," *IEEE Presse*, 1996.

[25] M. Al-Nuaimi and A. Siamarou, "Effects of human shadowing, traffic and antenna movements on 62.4 GHz indoor RLAN's channels," *IEEE Vehicular Technology Conference*, vol. 1, pp. 444–448, May 2001.

[26] T. Manabe, Y. Miura, and T. Ihara, "Effects of antenna directivity and polarization on indoor multipath propagation characteristics at 60 GHz," *IEEE Journal on Selected Areas in Communications*, vol. 14, pp. 441–448, April 1996.

[27] P. E. Mogensen, K. I. Pedersen, B. Fleury, F. Frederiksen, P. Leth-Espensen, Kim-Olesen, and S. L. Larsen, "2 D- channel characteristics," *ACTS 020Technical Report*, Dec 1997.

[28] R. S. Thomä, D. Hampicke, A. Richter, G. Sommerkorn, and A. Schneider, "Identification of time-variant directional mobile radio channels," *IEEE Transac. on Instrumentation and Measurement*, vol. 49, pp. 357–364, April 2000.

[29] P. Truffer and P. Leuthold, "Wide-band channel sounding at 24 GHz based on a novel fiber-optic synchronization concept," *IEEE Transactions on Microwave Theory and Techniques*, vol. 49, pp. 692–700, April 2001.

[30] B. H. Fleury, "First- and second-order characterization of direction dispersion and space selectivity in the radio channel," *IEEE Transactions on Information Theory*, vol. 46, pp. 2027 – 2044, September 2000.

[31] H. Droste and G. Kadel, "Measurement and analysis of wide band indoor propagation characteristics at 17 GHz and 60 GHz," *International Conference on Antennas and Propagation*, vol. 2, pp. 288–291, April 1995.

[32] T. Manabe, K. Taira, K. Sato, and T. Ihara, "Multipath measurement at 60 GHz for indoor wireless communication systems," *IEEE Vehicular Technology Conference*, pp. 905–909, March 1994.

[33] S.W.Wales, D.C.Rickard, M.A.Beach, and R. Davies, "Measurement and modelling of short range broadband millimetric mobile communication channels," *IEE Colloquium on Radiocommunications in the Range 30-60 GHz*, pp. 12/1–12/6, January 1991.

[34] M. Al-Nuaimi and A. Siamarou, "Coherence bandwidth characterisation and estimation for indoor rician multipath wireless channels using measurements at 62.4 GHz," *IEE Proceedings on Microwaves, Antennas and Propagation*, vol. 149, pp. 181–187, June 2002.

[35] D. Aszetly, "On antenna arrays in mobile communication systems: Fast fading and GSM base station receiver algorithms," *Ph.D. Dissertaion, Royal Institute of Technology, Stockholm, Sweden*, Mar 1996.

[36] W. C. Y. Lee, "Mobile communications engineering," *McGraw Hill*, vol. NY, 1989.

[37] S. P. Stapleton, X. Carbo, and T. McKeen, "Spatial channel simulator for phased arrays," *IEEE Vehicular Technology Conf.*, vol. 3, pp. 1789–1792, 8-10 June 1994.

[38] S. P. Stapleton, X. Carbo, and T. McKeen, "Tracking and diversity for a mobile communications base station array antenna," *IEEE Vehicular Technology Conf.*, vol. 3, pp. 1695–1699, April 1996.

[39] W. C. Jakes, "Microwave mobile communications," *IEEE Press, Piscataway, NJ*, 1974.

[40] G. G. Raleigh and A. Paulraj, "Time varying vector channel estimation for adaptive spatial equalization," *Proc. IEEE Globecom*, vol. 1, pp. 218–224, 13-17 Nov 1995.

[41] A. Saleh and R. Valenzuela, "A statistical model for indoor multipath propagation," *IEEE Journal on Selected Areas in Communications*, vol. 5, no. 2, pp. 128–137, 1987.

[42] Q. Spencer, M. Rice, B. Jeffs, and M. Jensen, "A statistical model for angle of arrival in indoor multipath propagation," *IEEE Vehicular Technology Conference*, vol. 3, pp. 1415–1419, May 1997.

[43] A. Klein, W. Mohr, R. Thomas, P. Weber, and B. Wirth, "Direction-of-arrival of partial waves in wideband mobile radio channels for intelligent antenna concepts," *IEEE Vehicular Technology Conference*, vol. 2, pp. 849–853, April 1996.

[44] M. Lu, T. Lo, and J. Litva, "A physical spatio-temporal model of multipath propagation channels," *IEEE Vehicular Technology Conference*, vol. 2, pp. 810–814, May 1997.

[45] J. J. Blanz, A. Klein, and W. Mohr, "Measurement-based parameter adaptation of wideband spatial mobile radio channel models," *IEEE 4th International Symposium on Spread Spectrum Techniques and Applications Proceedings*, vol. 1, pp. 91–97, Sept 1996.

[46] E. S. Sousa, V. M. Jovanovic, and C. Daigneault, "Delay spread measurements for the digital cellular channel in Toronto," *IEEE Transactions on Vehicular Technology*, vol. 43, pp. 837–847, Nov 1994.

[47] A. P. Dempster, N. M. Laird, and D. B. Rubin, "Maximum likelihood from incomplete data via the EM algorithm," *J. Royal Statist. Society*, vol. 39, no. 1, pp. 1–38, 1977.

[48] J. A. Fessler and A. O. Hero, "Space-alternating generalized expectation-maximization algorithm," *IEEE Transactions on Signal Processing*, vol. 42, pp. 2664 – 2677, October 1994.

[49] B. H. Fleury, M. Tschudin, R. Heddergott, D. Dahlhaus, and K. I. Pedersen, "Channel parameter estimation in mobile radio environments using the SAGE algorithm," *IEEE Journal on Selected Areas in Communications*, vol. 17, pp. 434–450, March 1999.

[50] M. Feder and E. Weinstein, "Parameter estimation of superimposed signals using the EM algorithm," *IEEE Transactions on Acoustics, Speech, and Signal Processing*, vol. 36, pp. 477 – 489, April 1988.

[51] M. D. Zoltowski, M. Haardt, and C. P. Mathews, "Closed-form 2-D angle estimation with rectangular arrays in element space or beamspace via unitary ESPRIT," *IEEE Transactions on Signal Processing*, vol. 44, pp. 316–328, February 1996.

[52] M. Haardt and J. Nossek, "3-D unitary ESPRIT for joint 2-D angle and carrier estimation," *IEEE Acoustics, Speech and Signal Processing Mag.*, vol. 1, pp. 255–258, 21-24 April 1997.

[53] D. Spielman, A. Paulraj, and T. Kailath, "A high resolution algorithm for combined time-of-arrival and direction-of-arrival estimation," *In Proc. 19th Asilomar Conf. on Circuits, Systems and Computer*, pp. 90–93, November 1985.

[54] A.-J. van der Veen., M. C. Vanderveen, and A. Paulraj, "Joint angle and delay estimation using shift-invariance techniques," *IEEE Transactions on Signal Processing*, vol. 46, pp. 405–418, February 1998.

[55] M. Toeltsch, J. Laurila, K. Kalliola, A. F. Molisch, P. Vainikainen, and E. Bonek, "Statistical characterization of urban spatial radio channels," *IEEE Journal on selected areas in commnunications*, vol. 20, April 2002.

[56] M. Tschudin, C. Brunner, T. Kurpjuhn, M. Haardt, and J. A. Nossek, "Comparison between unitary ESPRIT and SAGE for 3-D channel sounding," *IEEE Vehicular Technology Conference*, vol. 2, pp. 1324 – 1329, May 1999.

[57] P. Jung and G. Wunder, "On time-variant distortions in multicarrier transmission with application to frequency offsets and phase noise," *IEEE Transactions on Communications*, vol. 53, pp. 1561 – 1570, September 2005.

[58] L. Yi-Ching and C. Kwang-Cheng, "Estimation of wiener phase noise by the autocorrelation of the ICI weighting function in OFDM systems," *IEEE International Symposium on Personal, Indoor and Mobile Radio Communications*, vol. 2, pp. 725 – 729, September 2005.

[59] A. Kortke, *Analyse und Kalibration von linearen Microstrip-Patch-Antennenarrays.* PhD thesis, Technical University Berlin, March 2006.

[60] D. Rohde, A. Kortke, R. Ziegler, R. Eggemann, G. Grosskopf, and M. S. Choi, "Optically steered 1x4 patch array antenna for 60 GHz," *Microwaves and Optronics, the German Wireless Week (MIOP'2001)*, pp. 128–132, May 2001.

[61] M. S. Choi, G. Grosskopf, D. Rohde, B. Kuhlow, G. Przyrembel, and H. Ehlers, "Experiments on DOA-estimation and beamforming for 60 GHz smart antennas," *IEEE Semiannual Vehicular Technology Conference*, vol. 2, pp. 1041–1045, April 2003.

[62] P. Sanchis, V. Polo, J. Herrera, J. L. Corral, M. S. Choi, and J. Marti, "Experimental demonstration of a direction of arrival estimation algorithm for mm-wave broadband communication systems," *IEEE MTT-S International Microwave Symposium*, vol. 3, pp. 1533 – 1536, June 2003.

[63] G. Grosskopf, R. Eggemann, D. D. Rohde, and M. S. Choi, "155 Mbit/s data transmission at 60 GHz using a 1 x 4 patch array antenna with variable optical delay lines," *IEEE MTT-S International Microwave Symposium*, vol. 3, pp. 1821–1824, May 2001.

[64] G. Grosskopf, D. Rohde, A. Kortke, R. Eggemann, R. Ziegler, and M. S. Choi, "155 Mbit/s Datenübertragung im 60 GHz-Bereich mit einer optisch gesteuerten Array Antenne," *ITG Diskussionssitzung "Systeme mit intelligenten Antennen"*, p. Poster presentation, March 2001.

[65] K. Pensel and J. A. Nossek, "Uplink and downlink calibration of smart antennas," *International Conference on Telecommunications*, 1998.

[66] R. Heddergott and P. Truffer, "Results of indoor wideband delay-azimuth-elevation measurements for stochastic radio channel modeling," *European Cooperation in the field of scientific and technical research (COST 259 TD (99) 083)*, September 1999.

[67] M. S. Choi, G. Grosskopf, and D. Rohde, "A novel wideband space-time channel measurement method at 60 GHz," *IEEE 16th International Symposium on Personal, Indoor and Mobile Radio Communications*, vol. 1, pp. 584–588, September 2005.

[68] F. van der Wijk, A. Kegel, and R. Prasad, "Assessment of a pico-cellular system using propagation measurement at 1.9 GHz for indoor wireless communication," *IEEE Trans. on Veh. Tech*, vol. 44, pp. 155–162, February 1995.

[69] K. Pedersen, P. Mogensen, and B. Fleury, "Spatial channel characteristics in outdoor environments and their impact on BS antenna system performance," *IEEE Vehicular Technology Conference*, vol. 2, pp. 719–723, May 1998.

[70] T. Ao and G. Ke, "Study on power azimuth spectrum of wireless channel in microcell environments," *Personal, Indoor and Mobile Radio Communications, PIMRC 2003*, vol. 1, pp. 685–687, Sept 2003.

[71] R. Ertel and J. Reed, "Angle and time of arrival statistics for circular and elliptical scattering models," *IEEE Journal on Selected Areas in Communications*, vol. 17, no. 11, pp. 1829–1840, 1999.